General Relativity:
Alternatives, Tests and Applications

Dissertation
zur
Erlangung der naturwissenschaftlichen Doktorwürde
(Dr. sc. nat.)
vorgelegt der
Mathematisch-naturwissenschaftlichen Fakultät
der
Universität Zürich
von

Andreas Schärer

von
Stein am Rhein SH

Promotionskommission

Prof. Dr. Philippe Jetzer (Leitung der Dissertation)
Prof. Dr. Prasenjit Saha
Prof. Dr. Salvatore Capozziello

Zürich, 2017

Summary

This thesis covers different topics related to general relativity.

Even though general relativity is a very successful theory, it can be expected that it breaks down and unifies with quantum mechanics at very tiny scales of the order of the Planck energy. Other symptoms of its break-down include the observations of dark energy and dark matter, which cannot be explained with existent physics. It is therefore reasonable to study alternative theories of gravitation and compute the violations produced. We focus on single and multi scalar-tensor theories. We study them in the PPN framework and discuss ways of testing these theories experimentally.

According to general relativity, the ticking rate of a clock depends on its location in a gravitational field and its velocity. Thus, comparing an atomic clock onboard an orbiting satellite to local clocks on the Earth's surface allows testing gravity. We study the measurability of relativistic effects, such as frame-dragging effects, with such satellites and apply our method to possible terrestrial satellites and existing planetary missions.

Atomic clocks can also be used to measure changes in the gravitational field on Earth. We study the possibility of monitoring volcanoes with ground based clock networks, and find that this should be possible once high precision optical clocks are available for field measurements.

Publications

Chapter 2 is based on work published in Phys. Rev. D **90**, 123005 (2014) [1] and work still in preparation and not yet published [2].

Chapter 3 is based on work published in Phys. Rev. D. **89**, 064067 (2014) [3] and work submitted to Frontiers in Astronomy and Space Sciences [4].

Chapter 4 is based on work published in Geophys. J. Int. **202**, 1770 (2015) [5].

Table of Contents

Chapter 1

Introduction

General relativity (GR) explains gravitation as a geometrical feature emerging from a curved four-dimensional spacetime. It was founded by Albert Einstein more than 100 years ago.

Since then, general relativity managed to withstand many experimental probes like the perihelion precession of Mercury, the deflection of light and the gravitational redshift. While for a very long time technology was not or barely ready to probe the tiny effects predicted by general relativity in local experiments, this is no longer the case. Just recently, one century after they were predicted by Einstein, the *LIGO* collaboration directly detected gravitational waves for the first time. Gravitational wave astronomy opens a whole new possibility of observing the Universe and will yield many exciting and revolutionary scientific results. In the future, it will also be possible to observe gravitational waves using space-borne detectors. Also, different aspects of the Einstein equivalence principle, the foundation of general relativity consisting of three sub-principles, can now be tested rigorously. For example, the satellite mission *Microscope* tests the weak equivalence principle, stating that all test masses fall with the same acceleration in a gravitational field independent of their compositions, by using macroscopic masses. Atom interferometers can do a quantum test of the very same principle.

Atomic clocks today are sensitive enough to measure height differences at the centimeter level. This motivates building clock-carrying satellites that broadcast their onboard time to ground stations where it is compared to local time. Such a mission allows testing another part of the Einstein equivalence principle, the principle of local invariance. From this principle it follows that a clock's ticking rate depends on the gravitational potential it is exposed to. In addition, there are different relativistic effects, such as frame-dragging effect, that can be probed.

This technical readiness and the many experiments that are currently being performed, proposed or planned are also very exciting for theoreticians. These experiments will at least give better bounds on general relativity and constraints on alternative theories, or even find indications for physics beyond general relativity. Furthermore, one can think about applications outside fundamental physics that could benefit from the technology used in these experiments. For example, atomic clocks are a very interesting tool for geodesy, geophysics and planetary physics.

During my PhD, I worked on different projects that cover different aspects of general relativity. This thesis is divided into three parts, each discussing one such aspect. The first part discusses some classes of alternative theories of gravitation, the second the possibility of testing relativistic effects using satellite experiments and the third one geophysical applications of atomic clocks. Below, each part is briefly introduced.

First, in chapter 2, we discuss **scalar and multi scalar-tensor theories**, which are alternative theories of gravitation. These theories contain one or multiple scalar fields in addition to the metric tensor of general relativity. Note that there are many other alternative theories. In order to understand how such theories can be constructed, it makes sense to start with the Einstein field equations of standard general relativity

$$R_{\mu\nu} - \frac{1}{2} g_{\mu\nu} R = 8\pi G T_{\mu\nu} \,. \tag{1.1}$$

They relate the geometry of a four-dimensional spacetime on the left hand side to the mass and energy content of the Universe on the right hand side. Alternative theories are usually extensions, based on common general relativity. Typically, there are two philosophies of how to extend general relativity. One is to modify the LHS of the field equations, i.e., the geometry part, as done in $f(R)$ theories. There, the Einstein Hilbert action is modified like $\int R \to \int f(R)$. The other is to modify the energy part on the RHS, e.g., by introducing new matter fields such as scalar or vector fields. Here, we follow this second approach and study the role of additional scalar degrees of freedom.

Alternative theories predict deviations from general relativity. With a plethora of experiments in gravitational physics underway right now or being planned for the near future, different gravitational theories are being constrained or even excluded. This motivates the study of theories beyond general relativity.

But considering general relativity's success, why should we expect deviations and care for alternatives at all? There are many big questions that are still open and that will, in order to be understood, require new physics. Since gravitation is one of the fundamental forces of nature and has a major impact on the evolution and the dynamics of the Universe, it seems natural that modifications or extensions are necessary. For example, there is no quantum theory of gravitation yet. We know four fundamental forces: The electromagnetic force, the weak and the strong interaction and gravitation. While the first three can be described as quantum theories in the framework of quantum field theory, no quantum theory of gravitation has been found yet. However, with increasing accuracy in gravity experiments, at some level quantum effects could occur. But also at a classical level deviations from general relativity could arise. For example, effective scalar fields can arise from underlying, not-yet understood fundamental physics such as compactified extra dimensions or string theory. Furthermore, there are still many open questions in cosmology. For example, in the very early Universe there was a phase of enormous expansion that is necessary in order to explain the Universe as it is today. It is not possible to explain inflation with 'ordinary' physics only, additional physics is required. Typically, inflation is explained by a slowly rolling scalar field. Therefore, having scalar fields contributing to the evolution of the Universe in later stages seems to be natural. Another big question is the energy and matter content of the Universe. Typically, cosmologists 'tune' the matter and energy content of their theory in order to satisfy observations. But it is also possible that one has to modify the laws of physics, in particular of gravitational physics, instead — or in addition. The most popular model of our Universe is the ΛCDM model — a model with a surprisingly small number of parameters that works very well to describe observations. According to this model, only about 5% of the energy content of the Universe is made of matter as we know it. Some more than 25% is made of dark matter, a different type of matter that interacts gravitationally with ordinary matter. Even more mysterious is dark energy, which contributes the rest, i.e., around 70% to the Universe's energy budget. This dark energy causes the observed accelerated expansion of our Universe. While being explained by a cosmological constant in ΛCDM, dark energy could also be a cosmological scalar field called quintessence.

Scalar-tensor theories can be expressed in different equivalent frames, the ones usually used are the Jordan and the Einstein frame. In the Jordan frame, the scalar fields are non-minimally coupled to curvature and the matter fields couple to the frame metric directly. In the Einstein frame, in contrast, the fields are minimally coupled, letting the field equations appear similar to the ones of general relativity. This usually simplifies equations significantly compared to the corresponding ones in the Jordan frame.

Section 2.1 discusses (single) scalar-tensor theories. It contains the calculation of the PPN parameter β for a theory formulated in the Einstein frame. We introduce a simple formalism to discuss and constrain general scalar-tensor theories in Solar System experiments. It turns out that the leading order contribution to the scalar field falls off like a Yukawa potential $\sim e^{-mr}/r$ outside a central mass such as the Sun. This term gets multiplied by a coefficient that depends both on parameters of the theory and of the central mass. We calculate this parameter explicitly for a massive Brans-Dicke scalar field outside a homogeneous sphere. Further, we discuss the possibility of probing alternative theories with terrestrial satellites. The idea is that a satellite carrying an atomic clock on a preferably highly eccentric orbit sends timing signals to ground stations where the time is compared to that of local clocks. Thereby, one can search for violations of general relativity by comparing the observed time modulation to the one predicted by general relativity. This idea of using satellites with clocks is discussed in more detail in the subsequent chapter about relativistic effects.
Then, in section 2.2, multi scalar-tensor theories are discussed. The first goal of this project is to develop a framework to describe these theories geometrically. The second goal is to calculate the β parameter for these theories. This project is still work in progress and a draft is presented in this version of the thesis.

The second scientific topic, discussed in chapter 3, is the measurability of **relativistic effects** with satellite missions. One important consequence of general relativity is that the ticking rate of a clock depends on the clock's location in a gravitational field and its motion if it is compared to a reference clock. This can be tested by comparing the time of a clock onboard a satellite to the time measured by ground clocks. The time transfer can for example be done by using microwave links. With such a setup, a redshift $z = \Delta t_{\mathrm{e}}/\Delta t_{\mathrm{a}} - 1$ can be calculated. Δt_{e} is the time interval between two photons emitted at the satellite as measured by the onboard clock. Then, Δt_{a} is the time gap between the arrival times of the two photons at a ground station. In Newtonian physics, there is no time delay and photons travel on Minkowski straight lines, thus these two time intervals are the same, yielding $z = 0$. Comparing the measured redshift curve to the one predicted by a theory of gravity allows testing the theory. The idea of having satellites with very precise clocks is not new. E.g., the Global Positioning System (GPS) is a network of satellites each carrying an atomic clock.

The setup described above allows measuring different relativistic effects and we develop a code to calculate these. The orbit of the satellite and the trajectories of the signal photons are calculated by integrating Hamilton's equations for the Hamiltonian $H = 1/2 g^{\mu\nu} p_\mu p_\nu$, where p_μ is the relativistic four-momentum. The solutions yield the trajectories of freely falling particles, called geodesics. They generalize the notion of straight lines to curved spacetime. Orbits and photons follow time-like and null geodesics, respectively. In the Solar System, gravitational fields are very weak and massive objects like the planets move very slowly compared to the speed of light. Therefore, the dynamics within the Solar System is dominated by Newtonian physics, and general relativity provides very small corrections only. As a consequence, the general relativistic Hamiltonian can be expanded in velocity orders. While the leading order terms correspond to Newtonian motion, the terms appearing at higher orders correspond to different relativistic effects. Effects on the orbit and the photons have to be discussed individually. The first relativistic effect on the orbit is a time dilation effect. This is the effect that has to be taken into account for GPS. It actually already appears at the order that leads to Newtonian motion, i.e., Keplerian ellipses. The next higher order effect is what we call 'Schwarzschild space curvature', the effect that leads to the precession of perihelion of Mercury. We focus on the next higher effect, first-order spin. This is a frame-dragging effect, due to the rotation of the planet. At next higher order, a spin-squared and a further Schwarzschild effect arise. These effects are extremely small and have not been measured yet. To leading order, photons travel on straight lines. The first relativistic effect is the Shapiro time delay that slightly bends the signal's path. At next higher order, both spin and spin-squared effects arise. These effects have been previously undetected.

Section 3.1 gives the theoretical background necessary to develop the code and section 3.2 is an article discussing the measurability of relativistic effects in terrestrial and planetary satellite missions.

Applications of general relativity in geophysics are discussed in chapter 4. As briefly mentioned in section 3.2, atomic clocks and signal transponders onboard a satellite orbiting a planet can be used to investigate properties of the planet. Here, we discuss the possibility of doing relativistic geophysics using local atomic clocks or even a network of clocks on the Earth's surface. The ticking rate of a clock, when compared to a reference clock far away, depends on the gravitational potential it is sitting in. Thus, if a clock in a laboratory is lifted up, it is farther away from the Earth's center of mass and therefore experiences a weaker gravitational field. As a consequence, time will run faster compared to its original position. The best laboratory clocks today are sensitive to such changes at the centimeter level. Since the gravitational potential depends on the mass distribution, clocks are therefore sensitive to mass movements and density changes. Consequently, clocks can be used to monitor what is happening below the surface. We study the use of clocks to monitor volcanoes and the use of a global network of clocks to measure the solid Earth tides.

Finally, chapter 5 **concludes** this thesis. The most important results are summarized and also some remarks are added.

Chapter 2

Scalar and multi-scalar tensor theories

In this chapter, we discuss single and multi scalar-tensor theories, classes of alternative theories of gravitation. Sec. 2.1 is a publication about the single scalar field case while Sec. 2.2 extends the discussion to the more general case of multiple scalar fields. This project is still work in progress. In appendix A, some calculations used for Sec. 2.2 are demonstrated in detail.

2.1 Testing scalar-tensor theories and parametrized post-Newtonian parameters in Earth orbit

Andreas Schärer, Raymond Angélil, Ruxandra Bondarescu, Philippe Jetzer and Andrew Lundgren

Published in Phys. Rev. D **90**, 123005 (2014) [1].

Abstract

We compute the parametrized post-Newtonian (PPN) parameters γ and β for general scalar-tensor theories in the Einstein frame, which we compare to the existing PPN formulation in the Jordan frame for alternative theories of gravity. This computation is important for scalar-tensor theories that are expressed in the Einstein frame, such as chameleon and symmetron theories, which can incorporate hiding mechanisms that predict environment-dependent PPN parameters. We introduce a general formalism for scalar-tensor theories and constrain it using the limit on γ given by the Cassini experiment. In particular, we discuss massive Brans-Dicke scalar fields for extended sources. Next, using a recently proposed Earth satellite experiment, in which atomic clocks are used for spacecraft tracking, we compute the observable perturbations in the redshift induced by PPN parameters deviating from their general relativistic values. Our estimates suggest that $|\gamma - 1| \sim |\beta - 1| \sim 10^{-6}$ may be detectable by a satellite that carries a clock with fractional frequency uncertainty $\Delta f/f \sim 10^{-16}$ in an eccentric orbit around the Earth. Such space experiments are within reach of existing atomic clock technology. We discuss further the requirements necessary for such a mission to detect deviations from Einstein relativity.

2.1.1 Introduction

General relativity (GR) is the widely accepted theory to explain gravitation. Nonetheless, there are other theories of gravity which also satisfy the experimental constraints and remain candidates for the correct theory of gravity. These theories are being constrained by various high precision experiments. In particular, the recent development of ultra-precise frequency standards and atom interferometers provide new opportunities for testing different aspects of gravity. In this paper, we focus on scalar-tensor theories, which are a class of alternative theories of gravity that in addition to the metric tensor include a scalar field. We are interested both in developing the theoretical framework for testing these theories and in estimating potential constraints from upcoming satellite missions that carry clocks in space.

Scalar-tensor theories are widely used in particle physics, string theory and cosmology to model poorly understood phenomena for which we may have some observations such as in the case of dark matter and dark energy, but the new physics remains tantalizingly just out of reach. Effective scalar fields can arise from underlying, not-yet understood fundamental physics such as compactified extra dimensions [6] or string theory, which includes the dilaton scalar field [7]. Since the detection of the Higgs particle [8] we know that scalar (spin-0) particles exist in nature. The phase of inflation [9], a short period of rapid expansion in the very early Universe, could have been caused by a scalar field. Quintessence models make use of scalar fields causing the late-time acceleration of the Universe and therefore they could replace the cosmological constant and explain dark energy [10]. These scalar fields may couple to matter in ways that slightly violate general relativity and could be detected as our instrumentation becomes more precise.

The most accessible test bed for theories of gravity is the external environment of compact bodies such as binary pulsars or Solar System objects. Here, the gravitational field is weak, allowing the use of the parametrized post-Newtonian formalism (PPN). While there are infinitely many possible frames, typically, the Lagrangians of these theories are expressed either in the Jordan or the Einstein frame. In the Jordan frame, the scalar field multiplies the Ricci scalar and any present matter fields couple directly to the frame metric, while in the Einstein frame the Ricci scalar appears alone (as in traditional Einstein gravity) and the matter fields couple to a conformally related metric. We focus on the γ and β parameters predicted by scalar-tensor theories for which we have existent experimental constraints.

The simplest scalar-tensor theory is the original Brans-Dicke theory, where the massless scalar field and its constant coupling function (in the Jordan frame) lead to $\gamma = (\omega_0 + 1)/(\omega_0 + 2)$ and $\beta = 1$ [11]. For the case of a massive Brans-Dicke field, which contains a potential $U \sim m^2\varphi^2$ in addition to the constant coupling, these parameters were determined in [12]. The introduction of the mass term induces the γ parameter to become distance dependent. The parameters for chameleon theories were derived in [13]. In special cases, PPN parameters have been calculated for more general theories such as scalar-tensor-vector theories where, as its name implies, an additional vector field enters the stage of gravitation [14]. For general scalar-tensor theories formulated in the Jordan frame, they were determined by Hohmann *et al.* [15, 16].

We calculate the PPN parameters for a general scalar-tensor theory expressed in the Einstein frame. We show how this formalism can be useful for finding the PPN parameters for specific choices of scalar-tensor theories. Next, turning to a variety of scalar-tensor theories which predict constant PPN parameters, we investigate the near-future prospects for the measurement of deviations from Einstein relativity using a class of Earth-orbiting atomic clock experiments introduced in our earlier work, Angélil *et al.* (2014) [3].

The PPN parameters are typically calculated for a spacetime consisting of a point source surrounded by vacuum. This assumption is, in general, not appropriate to solve the scalar field equation of motion. For example in chameleon scalar field theories [17, 18] or symmetron theories [19, 20], the field behaves in a complex way inside the Earth due to its high density, significantly altering the external field profile. This also implies that the PPN parameters can depend on the environment. Performing an experiment around Earth may reveal different PPN parameters compared to the same experiment performed in the vicinity of the Sun.

Therefore, to discuss constraints on the PPN parameters in general we introduce a simple formalism containing a free parameter which can depend on the properties of both the theory and the source mass under consideration. It can account for the effects arising from the finite size of the source like screening effects in chameleon theories. We solve the scalar field equation for a massive Brans-Dicke scalar field inside and outside a sphere of constant density and show that our ansatz indeed represents the typical field profile of a massive scalar. The most stringent constraint in the Solar System comes from measurements of the Cassini spacecraft, which limit the size of the γ PPN parameter around the Sun [21]. We use this limit to improve constraints on massive Brans-Dicke theory discussed in [12, 15, 16] by regarding the Sun as a homogeneous sphere instead of a point source. However, while the Sun has low density, it is not an ideal candidate to probe theories that propose hiding mechanisms due to its high compactness M/R. Since both the Earth and the Moon have lower compactness, they are more suitable to test theories such as chameleon theories.

In the second part of the paper, we bring attention to the increasing accuracy of space-qualified atomic clocks. Our estimates show that a space clock that can reach the accuracy of the Atomic Clock Ensemble in Space (ACES) [22] $\Delta f/f \sim 10^{-16}$ in an eccentric orbit around the Earth could place constraints on the β and γ PPN parameters around the Earth of about 10^{-6} over the course of one orbit. It can be expected that in the future, many space missions will use either an ultraprecise atomic clock or a transponder that can reflect signals from clocks on Earth and in space to track the spacecraft. These will allow the ability to constrain or detect signals from alternative theories of gravity. The estimates presented here are obtained by taking the difference between the redshift signal generated by general relativity $\gamma = \beta = 1$, and the signal generated by a theory with γ and β different from one. The numbers obtained here are large enough to suggest detectability if a clock-carrying mission on an orbit like that of the originally proposed satellite Space-Time Explorer and QUantum Equivalence Principle Test (STE-QUEST) were to fly [23]. However, to make any definitive statements further work that aims to recover the signal of specific alternative theory of gravity from realistic data would be needed. We show that the difference in the redshift signal between general relativity and a small deviation peaks around the pericenter. We study the width of these peaks to find the time scale which needs to be resolved in order to be sensitive to such deviations.

The outline of this paper is as follows. In Sec. 2.1.2.1, the parametrized post-Newtonian formalism is briefly reviewed. Section 2.1.2.2 discusses the action and the equations of motion of a scalar-tensor theory in both the Jordan and the Einstein frame. The conformal transformation relating these frames is addressed, whereas more details can be found in Appendix 2.1.2.3. After briefly reviewing the procedure to obtain the PPN parameters in the Jordan frame in 2.1.2.4, we calculate these parameters in detail for any theory formulated in the Einstein frame in Sec. 2.1.2.5. In Sec. 2.1.3, we address constraints on scalar theories. We bring attention to the importance of screening mechanisms and propose a simple framework to constrain scalar theories and discuss current and future experimental constraints. Note that in this paper we restrict attention to local constraints on the PPN parameters and do not discuss cosmological constraints on scalar models. We apply this formalism to some examples: (2.1.3.1) Brans-Dicke theory, the simplest case of a scalar-tensor theory, (2.1.3.2) massless fields with a more general coupling, (2.1.3.3) massive Brans-Dicke theory and (2.1.3.4) chameleon fields, an example for a field with a screening mechanism. Next, in Sec. 2.1.4, we address the possibility of constraining PPN parameters in Earth orbit using satellites endowed with state-of-the-art atomic clocks. To do so, we estimate the relativistic effects coming from varying PPN parameters using a numerical orbit simulation.

Throughout this work we set the units to $c = \hbar = 1$, and therefore the reduced Planck mass is $M_{\mathrm{Pl}} = \sqrt{1/8\pi G}$.

2.1.2 Scalar-tensor theories in the Einstein frame

2.1.2.1 The parametrized post-Newtonian formalism

The most common way to parametrize theories of gravity in the weak field is to use the parametrized post-Newtonian (PPN) formalism [24]. There, the standard general relativistic metric is generalized with a collection of parameters which are permitted to take any value decreed by the alternative theory under consideration.

We start with the Schwarzschild metric written in isotropic coordinates $(t, \chi, \theta, \varphi)$

$$\begin{aligned} ds^2 &= g_{\mu\nu} dx^\mu dx^\nu \\ &= -\frac{\left(1-\frac{GM}{2\chi}\right)^2}{\left(1+\frac{GM}{2\chi}\right)^2} dt^2 + \left(1+\frac{GM}{2\chi}\right)^4 (d\chi^2 + \chi^2 d\Omega^2), \end{aligned} \tag{2.1}$$

where $d\Omega := d\theta^2 + \sin^2\theta d\varphi^2$. This is the vacuum solution of the Einstein field equations outside a spherically symmetric noncharged and nonrotating mass M. G denotes the Newtonian gravitational constant. In this paper, we are interested in Solar System constraints and since within the Solar System gravitational fields are weak and typical velocities are small, it is sufficient to consider the post-Newtonian limit of this metric. To do so, we introduce a parameter ϵ. Its power tracks the order of a term, where $\epsilon \sim GM/r$, although numerically $\epsilon = 1$. Massive particles moving on an orbit typically have velocities $v^2 \approx GM/r$ and therefore $\epsilon \sim v^2$ (note that other authors use the convention $\epsilon \sim v$). Typically, we have $GM/r \ll 1$ within the Solar System. Therefore, after endowing the different terms in the Schwarzschild metric with the appropriate ϵ^n, we can perform an expansion in ϵ and neglect higher order terms. For the post-Newtonian level, we keep terms up to order ϵ^2 in g_{00} and up to order ϵ in g_{ij}. Many alternative theories of gravity predict solutions which start to deviate from the ones predicted by general relativity at this level. Therefore, the parameters γ and β are added to the metric to model deviations from general relativity ($\gamma = \beta = 1$) [24]. Here, we promote the γ and β from constants to functions of χ. Additionally, the gravitational "constant" is allowed to change with distance.

This gives the metric

$$\begin{aligned} ds_{\mathrm{J}}^2 = &-\left(1 - h^{(1)}_{\mathrm{J}00}(\chi)\epsilon - h^{(2)}_{\mathrm{J}00}(\chi)\epsilon^2\right) dt_{\mathrm{J}}^2 \\ &+ \left(1 + h^{(1)}_{\mathrm{J}\chi\chi}(\chi)\epsilon\right)\left(d\chi^2 + \chi^2 d\Omega^2\right) \end{aligned} \tag{2.2}$$

with

$$\begin{aligned} h^{(1)}_{\mathrm{J}00}(\chi) &= \frac{2G_{\mathrm{J}}(\chi)M_{\mathrm{J}}}{\chi} \\ h^{(1)}_{\mathrm{J}\chi\chi}(\chi) &= \gamma(\chi)\frac{2G_{\mathrm{J}}(\chi)M_{\mathrm{J}}}{\chi} \\ h^{(2)}_{\mathrm{J}00}(\chi) &= -\beta(\chi)\frac{4G_{\mathrm{J}}^2(\chi)M_{\mathrm{J}}^2}{2\chi^2}. \end{aligned} \tag{2.3}$$

The index J indicates that this metric is formulated in the Jordan frame (see the next section). Note that if more intricate spacetimes are considered, additional parameters may enter the metric.

2.1.2.2 The choice of frame

The action of a scalar-tensor theory can be written in various ways. In the Jordan frame it is

$$\begin{aligned} S = &\int d^4x\sqrt{-g_{\mathrm{J}}}\frac{M_{\mathrm{Pl}}^2}{2}\left[\varphi R_{\mathrm{J}} - \frac{\omega(\varphi)}{\varphi}\left(\nabla_{\mathrm{J}}\varphi\right)^2 - U(\varphi)\right] \\ &+ \int d^4x\sqrt{-g_{\mathrm{J}}}\mathcal{L}_{\mathrm{m}}^{\mathrm{J}}(\Phi_{\mathrm{m}}, g_{\mu\nu}^{\mathrm{J}}), \end{aligned} \tag{2.4}$$

where the theory is characterized by the coupling function $\omega(\varphi)$ and the scalar potential $U(\varphi)$, both functions of the scalar field. The scalar field is considered to be positive everywhere and we assume that $U \geq 0$ and $\omega > -3/2$.

There are two characteristic properties of this frame. First, the nonminimally coupling term φR_{J} represents the coupling between the scalar field and curvature. Second, matter fields Φ_{m} couple to the frame metric $g_{\mu\nu}^{\mathrm{J}}$ which is used to determine the Christoffel symbols, the Ricci tensor, and to raise and lower indices. By varying this action with respect to the metric and the scalar field, the tensor and the scalar equations of motion

$$\begin{aligned} R_{\mu\nu}^{\mathrm{J}} = \frac{1}{\varphi}\Bigg[&8\pi G\left(T_{\mu\nu}^{\mathrm{J}} - \frac{\omega+1}{2\omega+3}g_{\mu\nu}^{\mathrm{J}}T_{\mathrm{J}}\right) + \nabla_\mu^{\mathrm{J}}\partial_\nu\varphi \\ &+ \frac{\omega}{\varphi}\partial_\mu\varphi\partial_\nu\varphi \quad - \frac{1}{2}g_{\mu\nu}^{\mathrm{J}}\frac{1}{2\omega+3}\frac{\partial\omega}{\partial\varphi}(\nabla_{\mathrm{J}}\varphi)^2 \\ &+ \frac{1}{2}g_{\mu\nu}^{\mathrm{J}}\frac{2\omega+1}{2\omega+3}U + \frac{1}{2}g_{\mu\nu}^{\mathrm{J}}\frac{1}{2\omega+3}\varphi\frac{\partial U}{\partial\varphi}\Bigg] \end{aligned} \tag{2.5a}$$

$$\nabla_{\mathrm{J}}^2\varphi = \frac{1}{2\omega+3}\left[8\pi G T_{\mathrm{J}} - \frac{\partial\omega}{\partial\varphi}\left(\nabla_{\mathrm{J}}\varphi\right)^2 - 2U + \frac{\partial U}{\partial\varphi}\right] \tag{2.5b}$$

are obtained, where $\nabla_{\mathrm{J}}^2 := g_{\mathrm{J}}^{\mu\nu}\nabla_\mu^{\mathrm{J}}\partial_\nu$. By ∇_μ^{J} we denote the covariant derivative obtained from the Jordan frame metric. By $T_{\mu\nu}^{\mathrm{J}}$ and $T_{\mathrm{J}} = g_{\mathrm{J}}^{\mu\nu}T_{\mu\nu}^{\mathrm{J}}$ we denote the stress-energy tensor and its trace in the Jordan frame.

Alternatively, a scalar-tensor theory can be expressed in the Einstein frame

$$\begin{aligned} S = &\int d^4x\sqrt{-g_{\mathrm{E}}}\frac{M_{\mathrm{Pl}}^2}{2}\left[R_{\mathrm{E}} - 2(\nabla_{\mathrm{E}}\phi)^2 - V(\phi)\right] \\ &+ \int d^4x\sqrt{-g_{\mathrm{E}}}\mathcal{L}_{\mathrm{m}}^{\mathrm{E}}(\Phi_{\mathrm{m}}, F(\phi)^{-1}g_{\mu\nu}^{\mathrm{E}}) \end{aligned} \tag{2.6}$$

with the corresponding equations of motion

$$R_{\mu\nu}^{\mathrm{E}} = 8\pi G\left(T_{\mu\nu}^{\mathrm{E}} - \frac{1}{2}g_{\mu\nu}^{\mathrm{E}}T_{\mathrm{E}}\right) + 2\partial_\mu\phi\partial_\nu\phi + \frac{1}{2}g_{\mu\nu}^{\mathrm{E}}V(\phi) \tag{2.7a}$$

$$\nabla_{\mathrm{E}}^2\phi = \frac{8\pi G}{4}\frac{F_{,\phi}}{F}T_{\mathrm{E}} + \frac{1}{4}V_{,\phi}. \tag{2.7b}$$

Here, the theory is determined by the coupling function $F(\phi)$ and the potential $V(\phi)$. In this frame, the field couples minimally to gravity and therefore, the gravity part of the action takes the form of the Einstein-Hilbert action in general relativity. This comes at the price that the matter fields do not couple to the Einstein frame metric directly but to the combination $F(\phi)^{-1}g_{\mu\nu}^{\mathrm{E}}$, and therefore, the coupling explicitly depends on the scalar field. But there is an obvious advantage when working in the Einstein frame: there, the equations of motion (2.7) are much simpler compared to the ones in the Jordan frame (2.5), even though these two frames are mathematically equivalent.

To avoid confusion between these two frames we label quantities with indices J and E, depending on the frame they are coming from. The two frames are related to each other by a conformal transformation

$$g^{\mathrm{J}}_{\mu\nu} = F(\phi)^{-1} g^{\mathrm{E}}_{\mu\nu} \tag{2.8}$$

with $\varphi = F > 0$, i.e., the scalar field in the Jordan frame mimics the coupling function in the Einstein frame. The positiveness of the fields is required to avoid a change of sign in the metric line element when going from one to the other frame.

2.1.2.3 Conformal transformation between Jordan and Einstein frame

In this section, we discuss the conformal transformation relating the metrics in the Jordan and the Einstein frame in detail. Starting in the Jordan frame (the converse is equivalent), we define the Einstein frame metric by $g^{\mathrm{E}}_{\mu\nu} := \varphi g^{\mathrm{J}}_{\mu\nu}$. For the square root of the trace of the metric and the Ricci scalars it holds $\sqrt{-g_{\mathrm{J}}} = \varphi^{-2}\sqrt{-g_{\mathrm{E}}}$ and $R_{\mathrm{J}} = \varphi\left[R_{\mathrm{E}} + 6\nabla^2_{\mathrm{E}} \ln \varphi^{1/2} - 6(\nabla_{\mathrm{E}} \ln \varphi^{1/2})^2\right]$, respectively [25]. Plugging this into the Jordan frame action (2.4) and integrating by parts yields

$$\begin{aligned} S = &\int d^4x \sqrt{-g_{\mathrm{E}}} \frac{M^2_{\mathrm{Pl}}}{2} \left[R_{\mathrm{E}} - \frac{2\omega+3}{2\varphi^2} \left(\nabla_{\mathrm{E}}\varphi\right)^2 - V\right] \\ &+ \int d^4x \sqrt{-g_{\mathrm{E}}} \mathcal{L}^{\mathrm{E}}_{\mathrm{m}}(\Phi_{\mathrm{m}}, \varphi^{-1} g^{\mathrm{E}}_{\mu\nu}), \end{aligned} \tag{2.9}$$

where we defined $V := \varphi^{-2} U$ and $\mathcal{L}^{\mathrm{E}}_{\mathrm{m}} := \varphi^{-2}\mathcal{L}^{\mathrm{J}}_{\mathrm{m}}$. To bring this into the desired form (2.6) we define a new scalar field ϕ by demanding

$$-2(\nabla_{\mathrm{E}}\phi)^2 = -\frac{2\omega+3}{2\varphi^2} \left(\nabla_{\mathrm{E}}\varphi\right)^2, \tag{2.10}$$

implying

$$\left(\frac{\partial\phi}{\partial\varphi}\right)^2 = \frac{2\omega+3}{4\varphi^2}. \tag{2.11}$$

Defining the Einstein frame coupling function by $F := \varphi$, we obtain

$$\left(\frac{\partial F}{\partial\phi}\right)^2 = \frac{4F^2}{2\omega+3}. \tag{2.12}$$

This requires $\omega > -3/2$ everywhere, and therefore $\omega_0 > -3/2$. Solving for ω yields

$$\omega = 2F^2 \left(\frac{\partial F}{\partial\phi}\right)^{-2} - \frac{3}{2}. \tag{2.13}$$

Using $F = \varphi$ and expanding both expressions in powers of ϵ,

$$F = F_0 + F_1(\phi - \phi_0) + F_2(\phi - \phi_0)^2 \tag{2.14a}$$

$$\varphi = \varphi_0 + \varphi_1\epsilon + \varphi_2\epsilon^2, \tag{2.14b}$$

one obtains

$$\begin{aligned} &\varphi_0 = F_0 \qquad \varphi_1 = F_1\phi_1 \qquad \varphi_2 = F_2\phi_1^2 + F_1\phi_2 \\ &\phi_1 = \frac{1}{F_1}\varphi_1 \qquad \phi_2 = \frac{1}{F_1}\varphi_2 - \frac{F_2}{F_1^3}\varphi_1^2. \end{aligned} \tag{2.15}$$

The relations between the coefficients of the couplings in the two frames are given by

$$\begin{aligned}
\omega_0 &= \frac{2F_0^2}{F_1^2} - \frac{3}{2} \qquad \omega_1 = \frac{4F_0}{F_1^2} - \frac{8F_0^2F_2}{F_1^4} \\
F_0 &= \varphi_0 \qquad F_1 = \pm\frac{2\varphi_0}{\sqrt{2\omega_0+3}} \\
F_2 &= \frac{2\varphi_0}{2\omega_0+3}\left(1 - \frac{\varphi_0\omega_1}{2\omega_0+3}\right),
\end{aligned} \tag{2.16}$$

and for the potentials, using $U = F^2V$, one finds

$$\begin{aligned}
U_2 &= \frac{F_0^2}{F_1^2}V_2 \qquad U_3 = \frac{2F_0}{F_1^2}\left(1 - \frac{F_0F_2}{F_1^2}\right)V_2 + \frac{F_0^2}{F_1^3}V_3 \\
V_2 &= \frac{4}{2\omega_0+3}U_2 \\
V_3 &= \pm\frac{8}{(2\omega_0+3)^{3/2}}\left[-\left(1+\frac{\varphi_0\omega_1}{2\omega_0+3}\right)U_2 + \varphi_0U_3\right].
\end{aligned} \tag{2.17}$$

The coordinates in the two frames are related by $t_{\mathrm{J}} = t_{\mathrm{E}}/\sqrt{F_0}$ and $\chi = r/\sqrt{F_0}$. Note, there is a $\pm$-ambiguity when going from the Jordan to the Einstein frame: two theories in the Einstein frame related by $F_1, V_3 \leftrightarrow -F_1, -V_3$ correspond to the same theory in the Jordan frame.

2.1.2.4 PPN parameters in the Jordan frame

The PPN parameters γ and β have been calculated for a general scalar-tensor theory stated in the Jordan frame [15, 16]. Here, we give a very short overview of their derivation. One starts with the ansatz for the metric (2.2) where χ is the radial coordinate in isotropic coordinates. Expanding the scalar field φ, the coupling function ω and the potential U in powers of ϵ (see Sec. 2.1.2.3) and solving the equations of motion (2.5) order by order, one finds [15, 16]

$$G_{\mathrm{J}}(\chi) = \frac{G}{\varphi_0}\left(1 + \frac{1}{2\omega_0+3}e^{-m_{\mathrm{J}}\chi}\right) \tag{2.18a}$$

$$\gamma(\chi) = \frac{1 - \frac{1}{2\omega_0+3}e^{-m_{\mathrm{J}}\chi}}{1 + \frac{1}{2\omega_0+3}e^{-m_{\mathrm{J}}\chi}} \tag{2.18b}$$

$$\begin{aligned}
\beta(\chi) = 1 &+ \frac{\varphi_0\omega_1}{(2\omega_0+3)^3\left(1+\frac{e^{-m_{\mathrm{J}}\chi}}{2\omega_0+3}\right)^2}e^{-2m_{\mathrm{J}}\chi} \\
&+ \frac{m_{\mathrm{J}}\chi}{2(2\omega_0+3)\left(1+\frac{e^{-m_{\mathrm{J}}\chi}}{2\omega_0+3}\right)^2}\Bigg[2e^{-m_{\mathrm{J}}\chi}\ln(m_{\mathrm{J}}\chi) - e^{-2m_{\mathrm{J}}\chi} - 2\left(m_{\mathrm{J}}\chi + e^{m_{\mathrm{J}}\chi}\right)\mathrm{Ei}(-2m_{\mathrm{J}}\chi) \\
&+ \frac{3\varphi_0}{2\omega_0+3}\left(\frac{U_3}{U_2} - \frac{1}{\varphi_0} - \frac{\omega_1}{2\omega_0+3}\right)\left[e^{-m_{\mathrm{J}}\chi}\mathrm{Ei}(-m_{\mathrm{J}}\chi) - e^{m_{\mathrm{J}}\chi}\mathrm{Ei}(-3m_{\mathrm{J}}\chi)\right]\Bigg],
\end{aligned} \tag{2.18c}$$

where

$$m_{\mathrm{J}} := \sqrt{\frac{2U_2\varphi_0}{2\omega_0+3}} \tag{2.19}$$

can be interpreted as the inverse range of the field or, roughly speaking, the mass of the field. In this expression we use the notation $U_2 = U''(\varphi_0)/2$. Here, we make use of the exponential integral

$$\text{Ei(-x)} := -\int_x^\infty da\frac{e^{-a}}{a}. \tag{2.20}$$

2.1.2.5 PPN parameters in the Einstein frame

In this section, we complement the Hohmann *et al.* [15, 16] approach by calculating the PPN parameters for a general scalar-tensor theory formulated in the Einstein frame. To do so, the equations of motion are solved order by order in the Einstein frame. Finally, we transform to the Jordan frame where the PPN parameters are defined. For the sake of understandability we perform the calculation in detail.

Here, we consider a spacetime consisting of a point mass surrounded by vacuum. The stress-energy tensor is given by that of a perfect fluid [24],

$$T^{\mu\nu} = (\rho + \rho\Pi + p)\, u^\mu u^\nu + p g^{\mu\nu}, \tag{2.21}$$

with the rest-mass density ρ, the pressure p, the specific energy density Π and the four-velocity u^μ, satisfying $u_\mu u^\mu = -1$. For Solar System tests we typically have $\rho \gg p$ and $\rho \gg \rho\Pi$, so we may neglect both the effects of pressure and specific energy density. If the mass is at rest ($u^i = 0$), we obtain $T_{\mu\nu} = \mathrm{diag}(\rho, 0, 0, 0)$. For a point source we have $\rho_\mathrm{E} = M_\mathrm{E}\delta(r)\epsilon$, where the index E implies that a quantity is defined in the Einstein frame.

For the metric in the Einstein frame we make the ansatz

$$\begin{aligned} ds_\mathrm{E}^2 = &-\left(1 - h^{(1)}_{\mathrm{E}00}(r)\epsilon - h^{(2)}_{\mathrm{E}00}(r)\epsilon^2\right) dt_\mathrm{E}^2 \\ &+ \left(1 + h^{(1)}_{\mathrm{E}rr}(r)\epsilon\right)\left(dr^2 + r^2 d\Omega^2\right), \end{aligned} \tag{2.22}$$

where we choose isotropic coordinates with radial coordinate r. We expand the scalar field in powers of ϵ and subsequently the coupling function and the potential are expanded around some constant value ϕ_0:

$$\phi(r) = \phi_0 + \phi_1(r)\epsilon + \phi_2(r)\epsilon^2 \tag{2.23a}$$

$$F(\phi) = F_0 + F_1(\phi - \phi_0) + F_2(\phi - \phi_0)^2 + F_3(\phi - \phi_0)^3 \tag{2.23b}$$

$$V(\phi) = V_0 + V_1(\phi - \phi_0) + V_2(\phi - \phi_0)^2 + V_3(\phi - \phi_0)^3 \tag{2.23c}$$

The left-hand sides of the equations (2.7a), the components of the Ricci tensor, are

$$\begin{aligned} R^\mathrm{E}_{00} = &-\frac{1}{2}\nabla_r^2 h^{(1)}_{\mathrm{E}00}\epsilon - \frac{1}{2}\Big(\nabla_r^2 h^{(2)}_{\mathrm{E}00} - h^{(1)}_{\mathrm{E}rr}\nabla_r^2 h^{(1)}_{\mathrm{E}00} \\ &+ \frac{1}{2}(\partial_r h^{(1)}_{\mathrm{E}00})^2 + \frac{1}{2}(\partial_r h^{(1)}_{\mathrm{E}00})(\partial_r h^{(1)}_{\mathrm{E}rr})\Big)\epsilon^2 + \mathcal{O}(\epsilon^3) \end{aligned} \tag{2.24a}$$

$$R^\mathrm{E}_{rr} = \left(-\partial_r^2 h^{(1)}_{\mathrm{E}rr} - \frac{1}{r}\partial_r h^{(1)}_{\mathrm{E}rr} + \frac{1}{2}\partial_r^2 h^{(1)}_{\mathrm{E}00}\right)\epsilon + \mathcal{O}(\epsilon^2) \tag{2.24b}$$

$$R^\mathrm{E}_{\theta\theta} = \frac{1}{2}r^2\left(-\partial_r^2 h^{(1)}_{\mathrm{E}rr} - \frac{3}{r}\partial_r h^{(1)}_{\mathrm{E}rr} + \frac{1}{r}\partial_r h^{(1)}_{\mathrm{E}00}\right)\epsilon + \mathcal{O}(\epsilon^2) \tag{2.24c}$$

$$R^\mathrm{E}_{\varphi\varphi} = R^\mathrm{E}_{\theta\theta}\sin^2\theta + \mathcal{O}(\epsilon^2) \tag{2.24d}$$

to the required orders. All other components are identically zero. The right-hand sides are

$$\begin{aligned}R^{\mathrm{E}}_{\mu\nu} = \frac{1}{2}\eta_{\mu\nu}V_0 + \Bigg[&8\pi G\left(\delta^0_\mu\delta^0_\nu + \frac{1}{2}\eta_{\mu\nu}\right)M_{\mathrm{E}}\delta(r)\\ &+ \frac{1}{2}\left(h^{(1)}_{\mathrm{E}\mu\nu}V_0 + \eta_{\mu\nu}V_1\phi_1\right)\Bigg]\epsilon\\ &+ \Bigg[\frac{8\pi G}{2}\left(h^{(1)}_{\mathrm{E}\mu\nu} + \eta_{\mu\nu}h^{(1)}_{\mathrm{E}00}\right)M_{\mathrm{E}}\delta(r)\\ &+ 2\partial_r\phi_1\partial_r\phi_1\delta^r_\mu\delta^r_\nu + \frac{1}{2}\eta_{\mu\nu}V_2\phi_1^2\\ &+ \frac{1}{2}(h^{(1)}_{\mathrm{E}\mu\nu}\phi_1 + \eta_{\mu\nu}\phi_2)V_1\Bigg]\epsilon^2 + \mathcal{O}(\epsilon^3).\end{aligned} \tag{2.25}$$

The flat-space Minkowski metric is, with our choice of coordinates, $\eta_{\mu\nu} = \mathrm{diag}(-1, 1, r^2, r^2\sin^2\theta)$. Calculating both sides of the scalar equation yields

$$\begin{aligned}\nabla^2_{\mathrm{E}}\phi = \nabla^2_r\phi_1\epsilon + \Bigg[&\nabla^2_r\phi_2 - h^{(1)}_{\mathrm{E}rr}\nabla^2_r\phi_1\\ &+ \frac{1}{2}\left(\partial_r h^{(1)}_{\mathrm{E}rr} - \partial_r h^{(1)}_{\mathrm{E}00}\right)\partial_r\phi_1\Bigg]\epsilon^2\end{aligned} \tag{2.26}$$

and

$$\begin{aligned}\nabla^2_{\mathrm{E}}\phi = \frac{1}{4}V_1 &+ \left[-\frac{F_1}{F_0}2\pi G M_{\mathrm{E}}\delta(r) + \frac{1}{2}V_2\phi_1\right]\epsilon\\ &+ \Bigg[\Bigg(2\pi G M_{\mathrm{E}}\left(\frac{F_1^2}{F_0^2} - \frac{2F_2}{F_0}\right)\phi_1\\ &- 2\pi G M_{\mathrm{E}}\frac{F_1}{F_0}h^{(1)}_{\mathrm{E}00}\Bigg)\delta(r) + \frac{3}{4}V_3\phi_1^2 + \frac{1}{2}V_2\phi_2\Bigg]\epsilon^2.\end{aligned} \tag{2.27}$$

By ∇^2_r we mean the flat space spherical coordinate Laplace operator, $\nabla^2_r := \partial^2_r + 2/r\partial_r$. First, we consider the zeroth-order equations

$$0 = \frac{1}{2}\eta_{\mu\nu}V_0 \tag{2.28a}$$

$$0 = \frac{1}{4}V_1, \tag{2.28b}$$

which require $V_0 = V_1 = 0$. At first order in ϵ, the scalar equation is

$$\left(\nabla^2_r - m^2_{\mathrm{E}}\right)\phi_1 = -\frac{F_1}{F_0}2\pi G M_{\mathrm{E}}\delta(r), \tag{2.29}$$

with solution

$$\phi_1(r) = \frac{F_1}{2F_0}\frac{GM_{\mathrm{E}}}{r}e^{-m_{\mathrm{E}}r}, \tag{2.30}$$

where we have defined

$$m^2_{\mathrm{E}} := \frac{1}{2}V_2. \tag{2.31}$$

The first order 00-tensor equation and its solution are

$$\begin{aligned} -\frac{1}{2}\nabla_r^2 h_{\mathrm{E}00}^{(1)} &= 8\pi G \frac{1}{2} M_\mathrm{E}\delta(r) \\ \rightarrow \quad h_{\mathrm{E}00}^{(1)}(r) &= \frac{2GM_\mathrm{E}}{r}. \end{aligned} \tag{2.32}$$

At the same order, the rr equation is

$$-\partial_r^2 h_{\mathrm{E}rr}^{(1)} - \frac{1}{r}\partial_r h_{\mathrm{E}rr}^{(1)} + \frac{1}{2}\partial_r^2 h_{\mathrm{E}00}^{(1)} = 8\pi G \frac{1}{2} M_\mathrm{E}\delta(r) \tag{2.33}$$

and the $\theta\theta$ equation turns into

$$-\partial_r^2 h_{\mathrm{E}rr}^{(1)} - \frac{3}{r}\partial_r h_{\mathrm{E}rr}^{(1)} + \frac{1}{r}\partial_r h_{\mathrm{E}00}^{(1)} = 8\pi G M_\mathrm{E}\delta(r). \tag{2.34}$$

Summing these two equations yields

$$\nabla_r^2 h_{\mathrm{E}rr}^{(1)} = -8\pi G M_\mathrm{E}\delta(r), \tag{2.35}$$

with solution

$$h_{\mathrm{E}rr}^{(1)}(r) = \frac{2GM_\mathrm{E}}{r}. \tag{2.36}$$

The 00 tensor equation at second order turns into

$$\nabla_r^2 h_{\mathrm{E}00}^{(2)} = -\frac{4G^2M_\mathrm{E}^2}{r^4} + \frac{F_1^2}{4F_0^2}V_2\frac{G^2M_\mathrm{E}^2}{r^2}e^{-2m_\mathrm{E}r}, \tag{2.37}$$

where we dropped a term proportional to $\delta(r)h_{\mathrm{E}rr}^{(1)}$ since it corresponds to gravitational self-energy [15, 16] and we get the solution

$$\begin{aligned} h_{\mathrm{E}00}^{(2)}(r) = -\frac{4G^2M_\mathrm{E}^2}{2r^2}\Bigg[1 - \frac{F_1^2}{4F_0^2}\bigg(&\frac{1}{2}m_\mathrm{E} r e^{-2m_\mathrm{E}r} \\ &+ m_\mathrm{E}^2 r^2 \mathrm{Ei}(-2m_\mathrm{E}r)\bigg)\Bigg]. \end{aligned} \tag{2.38}$$

We notice that the metric component at post-Newtonian order has an additional term compared to the Schwarzschild metric of general relativity. The second order scalar field equation is

$$\begin{aligned} \nabla_r^2\phi_2 - h_{\mathrm{E}rr}^{(1)}\nabla_r^2\phi_1 + \frac{1}{2}\left(\partial_r h_{\mathrm{E}rr}^{(1)} - \partial_r h_{\mathrm{E}00}^{(1)}\right)\partial_r\phi_1 \\ = \frac{3}{4}V_3\phi_1^2 + \frac{1}{2}V_2\phi_2. \end{aligned} \tag{2.39}$$

Also here, we dropped the gravitational self-energy terms proportional to $\phi_1\delta(r)$, $h_{\mathrm{E}00}^{(1)}\delta(r)$ and $h_{\mathrm{E}rr}^{(1)}\delta(r)$. For the solution we find

$$\begin{aligned} \phi_2(r) = \frac{1}{4}\frac{F_1}{2F_0}m_\mathrm{E}&\frac{4G^2M_\mathrm{E}^2}{r} \\ &\times\left[e^{m_\mathrm{E}r}\mathrm{Ei}(-2m_\mathrm{E}r) - e^{-m_\mathrm{E}r}\ln(m_\mathrm{E}r)\right] \\ + \frac{1}{2m_\mathrm{E}}&\frac{3F_1^2}{64F_0^2}V_3\frac{4G^2M_\mathrm{E}^2}{r} \\ &\times\left[e^{m_\mathrm{E}r}\mathrm{Ei}(-3m_\mathrm{E}r) - e^{-m_\mathrm{E}r}\mathrm{Ei}(-m_\mathrm{E}r)\right]. \end{aligned} \tag{2.40}$$

We have thus solved the equations of motion to post-Newtonian order. To determine the PPN parameters we must turn to the Jordan frame where they are defined. The metric line elements in the two frames are related by the conformal transformation (2.8), giving

$$\begin{aligned} ds_{\mathrm{J}}^2 &= F(\phi)^{-1} ds_{\mathrm{E}}^2 \\ &= -\Bigg[1 - \left(h_{\mathrm{E}00}^{(1)} + \frac{F_1}{F_0}\phi_1\right)\epsilon - \Bigg(h_{\mathrm{E}00}^{(2)} - \frac{F_1}{F_0} h_{\mathrm{E}00}^{(1)}\phi_1 \\ &\quad + \left(\frac{F_2}{F_0} - \frac{F_1^2}{F_0^2}\right)\phi_1^2 + \frac{F_1}{F_0}\phi_2\Bigg)\epsilon^2\Bigg] \frac{dt_{\mathrm{E}}^2}{F_0} \\ &\quad + \left[1 + \left(h_{\mathrm{E}rr}^{(1)} - \frac{F_1}{F_0}\phi_1\right)\epsilon\right]\left(\frac{dr^2}{F_0} + \frac{r^2}{F_0} d\Omega^2\right). \end{aligned} \tag{2.41}$$

Comparing this to the metric in the Jordan frame (2.2), we find

$$h_{\mathrm{J}00}^{(1)} = \frac{2G_{\mathrm{J}}M_{\mathrm{J}}}{\chi} \overset{!}{=} h_{\mathrm{E}00}^{(1)} + \frac{F_1}{F_0}\phi_1 \tag{2.42a}$$

$$h_{\mathrm{J}\chi\chi}^{(1)} = \gamma(\chi)\frac{2G_{\mathrm{J}}M_{\mathrm{J}}}{\chi} \overset{!}{=} h_{\mathrm{E}rr}^{(1)} - \frac{F_1}{F_0}\phi_1 \tag{2.42b}$$

$$\begin{aligned} h_{\mathrm{J}00}^{(2)} &= -\beta(\chi)\frac{4G_{\mathrm{J}}^2 M_{\mathrm{J}}^2}{2\chi^2} \\ &\overset{!}{=} h_{\mathrm{E}00}^{(2)} - \frac{F_1}{F_0} h_{\mathrm{E}00}^{(1)}\phi_1 + \left(\frac{F_2}{F_0} - \frac{F_1^2}{F_0^2}\right)\phi_1^2 + \frac{F_1}{F_0}\phi_2 \end{aligned} \tag{2.42c}$$

with

$$t_{\mathrm{J}} = \frac{t_{\mathrm{E}}}{\sqrt{F_0}} \tag{2.43a}$$

$$\chi = \frac{r}{\sqrt{F_0}}. \tag{2.43b}$$

From the $h_{\mathrm{J}00}^{(1)}$ relation we can identify the effective gravitational constant in the Jordan frame

$$G_{\mathrm{J}}(r) = \frac{r}{2F_0 M_{\mathrm{E}}}\left(h_{\mathrm{E}00}^{(1)} + \frac{F_1}{F_0}\phi_1\right), \tag{2.44}$$

where the masses in the Jordan frame satisfy

$$m_{\mathrm{J}} = \sqrt{F_0}\, m_{\mathrm{E}} \tag{2.45a}$$

$$M_{\mathrm{J}} = \sqrt{F_0}\, M_{\mathrm{E}}, \tag{2.45b}$$

such that $m_{\mathrm{J}}\chi = m_{\mathrm{E}} r$. With this we obtain the γ parameter

$$\gamma(r) = \frac{h_{\mathrm{E}rr}^{(1)} - \frac{F_1}{F_0}\phi_1}{h_{\mathrm{E}00}^{(1)} + \frac{F_1}{F_0}\phi_1}. \tag{2.46}$$

Finally, the β parameter is

$$\begin{aligned} \beta(r) &= \frac{2\chi^2}{4G_{\mathrm{J}}^2(r) M_{\mathrm{J}}^2}\left[\frac{F_1}{F_0} h_{\mathrm{E}00}^{(1)}\phi_1 - \left(\frac{F_2}{F_0} - \frac{F_1^2}{F_0^2}\right)\phi_1^2 - \frac{F_1}{F_0}\phi_2 - h_{\mathrm{E}00}^{(2)}\right] \\ &= 1 + \frac{1}{\left(h_{\mathrm{E}00}^{(1)} + \frac{F_1}{F_0}\phi_1\right)^2}\left[\left(\frac{F_1^2}{F_0^2} - \frac{2F_2}{F_0}\right)\phi_1^2 - \left(h_{\mathrm{E}00}^{(1)}\right)^2 - \frac{2F_1}{F_0}\phi_2 - 2h_{\mathrm{E}00}^{(2)}\right]. \end{aligned} \tag{2.47}$$

Inserting the scalar field and metric components determined above, we obtain the PPN parameters for a scalar-tensor theory formulated in the Einstein frame:

$$G_{\mathrm{J}}(r) = \frac{G}{F_0}\left(1 + \frac{F_1^2}{4F_0^2}e^{-m_{\mathrm{E}}r}\right) \tag{2.48a}$$

$$\gamma(r) = \frac{1 - \frac{F_1^2}{4F_0^2}e^{-m_{\mathrm{E}}r}}{1 + \frac{F_1^2}{4F_0^2}e^{-m_{\mathrm{E}}r}}. \tag{2.48b}$$

$$\begin{aligned}\beta(r) = 1 &+ \frac{F_1^2}{4F_0^2\left(1 + \frac{F_1^2}{4F_0^2}e^{-m_{\mathrm{E}}r}\right)^2}\left(\frac{F_1^2}{4F_0^2} - \frac{F_2}{2F_0}\right)e^{-2m_{\mathrm{E}}r} \\ &+ \frac{F_1^2 m_{\mathrm{E}}r}{32F_0^2\left(1 + \frac{F_1^2}{4F_0^2}e^{-m_{\mathrm{E}}r}\right)^2}\Bigg[8e^{-m_{\mathrm{E}}r}\ln m_{\mathrm{E}}r - 4e^{-2m_{\mathrm{E}}r} - 8\left(e^{m_{\mathrm{E}}r} + m_{\mathrm{E}}r\right)\mathrm{Ei}(-2m_{\mathrm{E}}r) \\ &\qquad + 3\frac{F_1}{F_0}\frac{V_3}{V_2}\left(e^{-m_{\mathrm{E}}r}\mathrm{Ei}(-m_{\mathrm{E}}r) - e^{m_{\mathrm{E}}r}\mathrm{Ei}(-3m_{\mathrm{E}}r)\right)\Bigg]\end{aligned} \tag{2.48c}$$

To compare this result to the one found in [15, 16], we use the transformation laws for the coupling functions (2.16) and the potentials (2.17). Indeed, this leads to Eq. (2.18).

If we choose to neglect the second order deviation from the Schwarzschild metric (i.e., $h^{(2)}_{\mathrm{E}00} = -2G^2M_{\mathrm{E}}^2/r^2$) and only consider the leading order scalar field contribution (i.e., we set $\phi_2 = 0$), then the effective coupling constant and the PPN parameters simplify to

$$G_{\mathrm{J}}(r) = \frac{G}{F_0}\left(1 + \frac{F_1}{2F_0}\frac{r}{GM_{\mathrm{E}}}\phi_1\right) \tag{2.49a}$$

$$\gamma(r) = \frac{1 - \frac{F_1}{2F_0}\frac{r}{GM_{\mathrm{E}}}\phi_1}{1 + \frac{F_1}{2F_0}\frac{r}{GM_{\mathrm{E}}}\phi_1} \tag{2.49b}$$

$$\beta(r) = 1 + \frac{\left(\frac{F_1^2}{4F_0^2} - \frac{F_2}{2F_0}\right)\phi_1^2}{\left(\frac{GM_{\mathrm{E}}}{r} + \frac{F_1}{2F_0}\phi_1\right)^2}. \tag{2.49c}$$

We notice that on the one hand, any nontrivial scalar-tensor theory predicts a γ different from its general relativity value 1. On the other hand, it is still possible to have $\beta = 1$: if $F_1^2/F_0 - 2F_2 = 0$. This condition is equivalent to $F'(\phi_0)^2/F(\phi_0) - F''(\phi_0) = 0$ which is solved by $F(\phi) = c_1\exp(c_2\phi)$. An exponential coupling function in the Einstein frame corresponds to a constant coupling function in the Jordan frame, $\omega = \omega_0$, and therefore to a Brans-Dicke-like theory as for instance the original chameleon model (see Secs. 2.1.3.1 and 2.1.3.4).

In the following section we discuss current constraints on the PPN parameters and apply them to our formalism. In particular the constraint on γ coming from the Cassini spacecraft is discussed. This is followed by some important examples of scalar-tensor theories.

2.1.3 Experimental framework and constraints

Above we have discussed the scalar field in vacuum outside a point source in the weak field limit. The assumption of a point source is obviously not correct for experiments performed around extended objects as the Earth or the Sun. Within such an object the field can behave very different to that of a point source and screening mechanisms can show up due to nonlinear effects. But still, since the density in the Solar System is very low, one can expect the field to maintain the form $\phi_1 \sim e^{-mr}/r$ in the low density region outside some source. Therefore, we make the ansatz

$$\varphi(\chi) = \varphi_0 + \varphi_1(\chi) = \varphi_0 + \xi \frac{2}{2\omega_0 + 3} \frac{GM_\mathrm{J}}{\chi} e^{-m_\mathrm{J}(\chi - X)} \tag{2.50a}$$

$$\phi(r) = \phi_0 + \phi_1(r) = \phi_0 + \xi \frac{F_1}{2F_0} \frac{GM_\mathrm{E}}{r} e^{-m_\mathrm{E}(r-R)} \tag{2.50b}$$

for the exterior field up to first order, written in the Jordan and the Einstein frame, respectively. By X (Jordan frame) and $R = \sqrt{F_0}X$ (Einstein frame) we denote the size of the object. Therefore, the field starts falling off exponentially at the surface of the source instead of at its center. Notice that we introduced some arbitrary parameter ξ. By doing so, we are able to discuss constraints on the PPN parameters around more realistic sources, also for theories containing screening mechanisms without knowing their exact nature. The ξ parameter describes how much the exterior field deviates from that generated by a point source ($\xi = 1$) with the same mass. In other words, a source can act as an effective point source of mass ξM. In particular, we will show in Sec. 2.1.3.3 that a massive Brans-Dicke scalar field takes this form if we consider the source to be a sphere with constant density. We find an expression for ξ which depends on both the mass of the scalar field and the radius of the source.

Plugging the ansatz above into (2.49) we find the effective gravitational constant and the PPN parameters

$$\begin{aligned} G_\mathrm{J} &= \frac{G}{F_0}\left(1 + \xi \frac{F_1^2}{4F_0^2} e^{-m_\mathrm{E}(r-R)}\right) \\ &= \frac{G}{\varphi_0}\left(1 + \xi \frac{1}{2\omega_0 + 3} e^{-m_\mathrm{J}(\chi - X)}\right) \end{aligned} \tag{2.51a}$$

$$\gamma = \frac{1 - \xi \frac{F_1^2}{4F_0^2} e^{-m_\mathrm{E}(r-R)}}{1 + \xi \frac{F_1^2}{4F_0^2} e^{-m_\mathrm{E}(r-R)}} = \frac{1 - \frac{\xi}{2\omega_0+3} e^{-m_\mathrm{J}(\chi - X)}}{1 + \frac{\xi}{2\omega_0+3} e^{-m_\mathrm{J}(\chi - X)}} \tag{2.51b}$$

$$\begin{aligned} \beta &= 1 + \frac{\left(1 - \frac{2F_0F_2}{F_1^2}\right)}{\left[1 + \left(\xi \frac{F_1^2}{4F_0^2} e^{-m_\mathrm{E}(r-R)}\right)^{-1}\right]^2} \\ &= 1 + \frac{\frac{\varphi_0 \omega_1}{2\omega_0+3}}{\left[1 + \left(\xi \frac{1}{2\omega_0+3} e^{-m_\mathrm{J}(\chi - X)}\right)^{-1}\right]^2}. \end{aligned} \tag{2.51c}$$

Typically, experimental constraints on PPN parameters are used to limit the $(\omega_0, \tilde{m}_\mathrm{J})$-parameter space [12, 15, 16]. The definition of the ω_0-independent mass

$$\tilde{m}_\mathrm{J} := \sqrt{2U_2\varphi_0} \tag{2.52}$$

is required in order to have two independent parameters since the original mass m_J, defined in (2.19), depends on ω_0. But since we want to incorporate possible screening mechanisms in extended sources, giving us the additional parameter ξ, we consider a slightly different approach. We define a new parameter,

$$\alpha := \frac{\xi}{2\omega_0 + 3} = \xi \frac{F_1^2}{4F_0^2}, \tag{2.53}$$

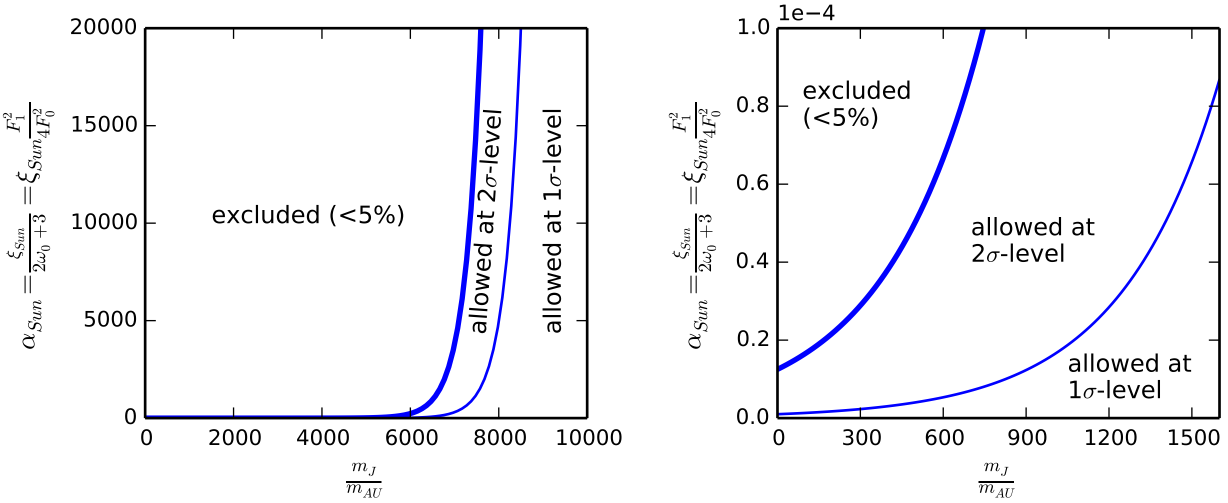

Figure 2.1: Cassini constraint on scalar-tensor theories. The Cassini constraint $\gamma = 1+(2.1\pm2.3)\times10^{-5}$ (at 1σ level) together with Eq. (2.51b) and $\chi - X_{\rm Sun} = 0.6$ solar radii $= 0.00279$AU are used to constrain the $(\alpha_{\rm Sun}, m_{\rm J})$-parameter space. The solid lines divide the plots into regions that are excluded (probability $< 5\%$) and that are allowed at the 2σ level and at the 1σ level, respectively. The x axis shows the mass, i.e., the inverse range, of the scalar field in the Jordan frame in terms of inverse astronomical units $m_{\rm AU} = 1/{\rm AU}$, the y axis shows $\alpha_{\rm Sun} = \xi_{\rm Sun}/(2\omega_0+3) = \xi_{\rm Sun}F_1^2/(4F_0^2)$ where $\xi_{\rm Sun}$ is a parameter characteristic for the Sun.

allowing us to constrain the $(\alpha, m_{\rm J})$-parameter space. Notice that α contains two different kinds of parameters. First, the components of the scalar coupling functions, ω_0 and F_1^2/F_0^2, depend on the underlying theory of gravity only and are the same everywhere. Second, the parameter ξ can depend on properties of the source, as its composition. Therefore, it can vary drastically among different sources.

There are different experimental constraints on the PPN parameters. The most stringent one comes from measuring the frequency shift of a radio signal sent from and to the Cassini spacecraft while close to conjunction with the Sun, with $\gamma = 1 + (2.1 \pm 2.3) \times 10^{-5}$ at the 1σ-confidence level [21]. The closest distance between the propagating signal and the center of the Sun was 1.6 solar radii. We can now use this to constrain the parameter space $(\alpha_{\rm Sun}, m_{\rm E})$, as shown in Fig. 2.1.

The perihelion precession of Mercury gives the constraint $|2\gamma - \beta - 1| < 3 \times 10^{-3}$ [11]. Planetary ephemerides are used to constrain $|\gamma-1|$ and $|\beta-1|$ to the 10^{-5} level [26, 27]. But since the gravitational interaction does not take place at a fixed distance from some massive body, this limit cannot be used to constrain the distance dependent parameters discussed here.

Scalar theories can also be constrained by accurate measurements of the periods of binary pulsars: if scalar radiation is emitted, it results in a change of the orbital period [28].

The GAIA mission launched in 2013, located at the Sun-Earth Lagrange point L2, is expected to improve the constraint on γ to the 10^{-6} level [29] via relativistic astrometry by precisely monitoring the 3D motion of planets and stars in our Galaxy.

In the following subsections, we consider specific theories of gravity and use the above formalism to calculate their PPN parameters. The Cassini measurement can then be used to constrain these theories. As atomic clocks become more accurate, clock carrying satellites that orbit the Earth will place constraints on the value of the PPN parameters around our own planet. We will discuss such measurements in Sec. 2.1.4.

2.1.3.1 Brans-Dicke theory

The simplest example and the prototype of scalar-tensor theories is Brans-Dicke theory [30]. In the Jordan frame it is defined to have a constant coupling $\omega = \omega_0$ and a vanishing scalar potential, leaving the field massless, $m_{\mathrm{J}} = 0$. Therefore, the PPN parameters will not have a distance dependence and we have $\xi = 1$ because no hiding mechanism occurs.

In this theory, ω_0 is the only parameter. With (2.13) and (2.14a) we obtain the coupling function $F(\phi) = F_0 \exp[\pm 2(\phi - \phi_0)/\sqrt{2\omega_0 + 3}]$. Therefore, in the Einstein frame, Brans-Dicke theories have an exponential coupling function with no scalar potential term. This gives $\beta = 1$ as in general relativity and $\gamma = (\omega_0 + 1)/(\omega_0 + 2)$. Using the Cassini constraint on γ, one finds that $\omega_0 > 40000$ at the 2σ level.

2.1.3.2 Eddington-Robertson metric

Assuming that the potential vanishes $U = V = 0$ and then solving the equations of motion yields the PPN parameters

$$G_{\mathrm{J}} = \frac{G}{\varphi_0}\left(1 + \frac{1}{2\omega_0 + 3}\right) = \frac{G}{F_0}\left(1 + \frac{F_1^2}{4F_0^2}\right) \tag{2.54a}$$

$$\gamma = \frac{1 + \omega_0}{2 + \omega_0} = \frac{1 - \frac{F_1^2}{4F_0^2}}{1 + \frac{F_1^2}{4F_0^2}} \tag{2.54b}$$

$$\beta = 1 + \frac{\varphi_0 \omega_1}{(2\omega_0 + 3)(2\omega_0 + 4)^2} = 1 + \frac{\frac{F_1^2}{4F_0^2}\left(\frac{F_1^2}{4F_0^2} - \frac{F_2}{2F_0}\right)}{\left(1 + \frac{F_1^2}{4F_0^2}\right)^2}. \tag{2.54c}$$

Due to the absence of the potential there is no distance dependence in both G_{J} and the PPN parameters. The metric (2.2) with these constant parameters was given by Eddington and Robertson [31]. So, for fixed values of γ and β we can invert these expressions to obtain the components of the coupling function in the Jordan frame,

$$\omega_0 = -\frac{2\gamma - 1}{\gamma - 1} \tag{2.55a}$$

$$\omega_1 = -\frac{4(\beta - 1)(\gamma + 1)}{\varphi_0(\gamma - 1)^3} \tag{2.55b}$$

and accordingly in the Einstein frame

$$\frac{F_1^2}{4F_0^2} = \frac{1 - \gamma}{1 + \gamma} \tag{2.56a}$$

$$\frac{F_2}{2F_0} = \frac{5 - 4\beta - 2\gamma + \gamma^2}{1 - \gamma^2}. \tag{2.56b}$$

2.1.3.3 Massive Brans-Dicke theory

Here, we solve the scalar field equation of a massive Brans-Dicke scalar field generated by a more realistic source than a point mass. We consider a coupling function which is, as in the original Brans-Dicke theory, exponential in the Einstein frame and thus constant ($\omega = \omega_0$) in the Jordan frame.

Further, in the Einstein frame we add a quadratic potential $V = V_2(\phi - \phi_0)^2$ with $V_2 = 2m_\mathrm{E}$. This corresponds to the potential $U = U_2(\varphi - \varphi_0)^2$ in the Jordan frame.

For the case of a point source, constraints on massive Brans-Dicke fields have been discussed in [12, 15, 16]. There, the authors used the Cassini constraint on γ to limit the $(\tilde{m}_\mathrm{J}, \omega_0)$-parameter space. Here, we extend this discussion by replacing the point source with a more realistic density distribution. This will allow us to determine the parameter ξ, introduced in (2.50).

We consider a static spherically symmetric mass with radius R and constant density ρ_{E0} [i.e., $\rho_E(r) = \rho_{E0}$ for $r < R$ and $\rho_E(r) = 0$ otherwise)] and we neglect the gravitational effects of pressure. Further, we assume that the mass is surrounded by vacuum. The equation of motion is given by

$$\left(\nabla_r^2 - m_\mathrm{E}^2\right) \phi_1(r) = -\frac{F_1}{F_0} 2\pi G \rho_\mathrm{E}(r), \tag{2.57}$$

which follows from (2.29). To solve this equation we make use of the Green function $G(\boldsymbol{r}) = -e^{-m_\mathrm{E} r}/4\pi r$, solving the equation $\left(\nabla_r^2 - m_\mathrm{E}^2\right) G(\boldsymbol{r}) = \delta(\boldsymbol{r})$. Then we find the scalar field by integrating

$$\begin{aligned}\phi_1(\boldsymbol{r}) &= \int G(|(\boldsymbol{r}) - (\boldsymbol{s})|) \left(-\frac{F_1}{F_0} 2\pi G \rho_\mathrm{E}(s)\right) d^3\boldsymbol{s} \\ &= \frac{F_1}{F_0} \pi G \rho_{E0} \\ &\quad \times \int_0^\pi \int_0^R \frac{e^{-m_\mathrm{E}\sqrt{r^2+s^2-2rs\cos\theta}}}{\sqrt{r^2+s^2-2rs\cos\theta}} s^2 \sin\theta \, ds \, d\theta.\end{aligned} \tag{2.58}$$

To obtain the exterior solution $\phi_1^\mathrm{ext}(r > R)$, the integrand is expanded around $s/r = 0$, since $r > s$ for all s. This allows each term of the Taylor series to be integrated, giving

$$\begin{aligned}\phi_1^\mathrm{ext}(r > R) =& \frac{F_1}{F_0} \frac{\pi G \rho_{E0}}{r} e^{-m_\mathrm{E} r} \\ &\times \sum_{k=0}^{\infty} m_\mathrm{E}^{2k} R^{2k+3} \frac{2}{(2k+1)!(2k+3)}.\end{aligned} \tag{2.59}$$

Finally, this can be written as

$$\begin{aligned}\phi_1^\mathrm{ext}(r > R) = &\left(3 \frac{m_\mathrm{E} R \cosh(m_\mathrm{E} R) - \sinh(m_\mathrm{E} R)}{R^3 m_\mathrm{E}^3} e^{-m_\mathrm{E} R}\right) \\ &\times \frac{F_1}{2F_0} \frac{G M_\mathrm{E}}{r} e^{-m_\mathrm{E}(r-R)},\end{aligned} \tag{2.60}$$

where in the last step we substituted $M_\mathrm{E} = 4\pi/3 \rho_{E0} R^3$.

The interior solution $\phi_1^\mathrm{ext}(r < R)$ is obtained by splitting the integral over s into two parts. First, we perform the integral $\int_0^r$ where we can expand around $s/r = 0$ and find the solution analogous to the exterior solution. Second, for the integral from $\int_r^R$ we can expand around $r/s = 0$. Together, we find

$$\begin{aligned}\phi_1^\mathrm{int}(r < R) =& 3 \frac{F_1}{2F_0} \frac{G M_\mathrm{E}}{R^3} \left[\frac{e^{-m_\mathrm{E} r}}{m_\mathrm{E}^2} \left(\cosh\left(m_\mathrm{E} r\right) + \sinh\left(m_\mathrm{E} r\right)\right)\right. \\ &\left. - e^{-m_\mathrm{E} R} \frac{1 + m_\mathrm{E} R}{m_\mathrm{E}^3 r} \sinh\left(m_\mathrm{E} r\right)\right].\end{aligned} \tag{2.61}$$

Notice that the exterior solution (2.60) precisely coincides with the general ansatz (2.50) if we choose

$$\xi = 3 \frac{m_\mathrm{E} R \cosh(m_\mathrm{E} R) - \sinh(m_\mathrm{E} R)}{R^3 m_\mathrm{E}^3} e^{-m_\mathrm{E} R}. \tag{2.62}$$

The solution expressed in the Jordan frame is

$$\begin{aligned}
\varphi_1^{\text{ext}}(\chi > X) &= \left(3\frac{m_\text{J} X\cosh(m_\text{J} X) - \sinh(m_\text{J} X)}{X^3 m_\text{J}^3} e^{-m_\text{J} X}\right) \\
&\quad \times \frac{2}{2\omega_0 + 3}\frac{GM_\text{J}}{\chi} e^{-m_\text{J}(\chi - X)} \\
\varphi_1^{\text{int}}(\chi < X) &= \frac{6}{2\omega_0+3}\frac{GM_\text{J}}{X^3} \\
&\quad \times \left[\frac{e^{-m_\text{J}\chi}}{m_\text{J}^2}\left(\cosh\left(m_\text{J}\chi\right) + \sinh\left(m_\text{J}\chi\right)\right)\right. \\
&\qquad \left. - e^{-m_\text{J} X}\frac{1 + m_\text{J} X}{m_\text{J}^3 \chi}\sinh\left(m_\text{J}\chi\right)\right].
\end{aligned} \tag{2.63}$$

Since the γ parameter (2.51b) depends on ξ, it depends on the size of the source. In the massless limit $m_{\text{E/J}} \to 0$, ξ approaches unity. Then, γ depends on properties of the theory only and is independent of R. In the limit of vanishing radius, ξ approaches unity as well, giving the same result as for a point source.

While in [12] the interaction distance is assumed to be $r = 1\,\text{AU}$, Hohmann *et al.* [15, 16] choose $r = 1.6$ solar radii since this is the closest distance between the signal and the Sun. This dramatically improves the constraints on $\tilde{m}_\text{J}$ and ω_0. Including ξ given by (2.62), which accounts for the assumption that the Sun is a sphere with constant density, the constraint on the $(\tilde{m}_\text{J}, \omega_0)$-parameter space given by the Cassini experiment is shown in Fig. 2.2 (solid lines), where we assume that $r = 1.6$ solar radii. Comparing to the dashed lines which represent the analogous result for a point source, we notice that the constraints are more stringent if an extended source is considered. This is due to the fact that, even though $\xi < 1$, the field falls off like $e^{-m_\text{E}(r-R)}$ instead of $e^{-m_\text{E} r}$.

2.1.3.4 Chameleon theory

Another example of a class of scalar-tensor theories are chameleon theories, introduced by Khoury and Weltman [17, 18]. They allow a very light cosmological scalar field that couples to matter with gravitational strength and satisfies current observational constraints. Formulated in the Einstein frame, chameleons have, as Brans-Dicke theory does, an exponential coupling function $F(\phi) = \exp(-2\sqrt{2}k_i\phi)$. The coupling constants k_i may vary for different matter species i, but for simplicity we assume that they take the same value k for all kinds of matter. This assumption is taken in accordance with general relativity where gravitation couples universally to all matter species and thereby ensures that the weak equivalence principle is satisfied. The presence of a scalar field would lead to an additional (or *fifth*) force and consequently, a matter-dependent scalar coupling would lead to violations of the weak equivalence principle. A possible model to explain such a matter-dependent scalar coupling is given by Damour and Donoghue [32].

In contrast to Brans-Dicke, chameleons have a scalar potential, giving the field a mass and therefore a finite range. Typically, runaway potentials like an inverse power-law potential $V \sim \phi^{-n}$ are considered. The interplay between such a potential and the exponential coupling causes the range of the scalar field to depend on the surrounding matter density. In a dense region, like inside the Earth or within its atmosphere, the scalar field becomes so massive that the force corresponding to the scalar field becomes short ranged. This hiding feature makes it very difficult to detect the chameleon field with Earth-based experiments. On larger scales the field is long ranged and it might be detectable by experiments performed in space.

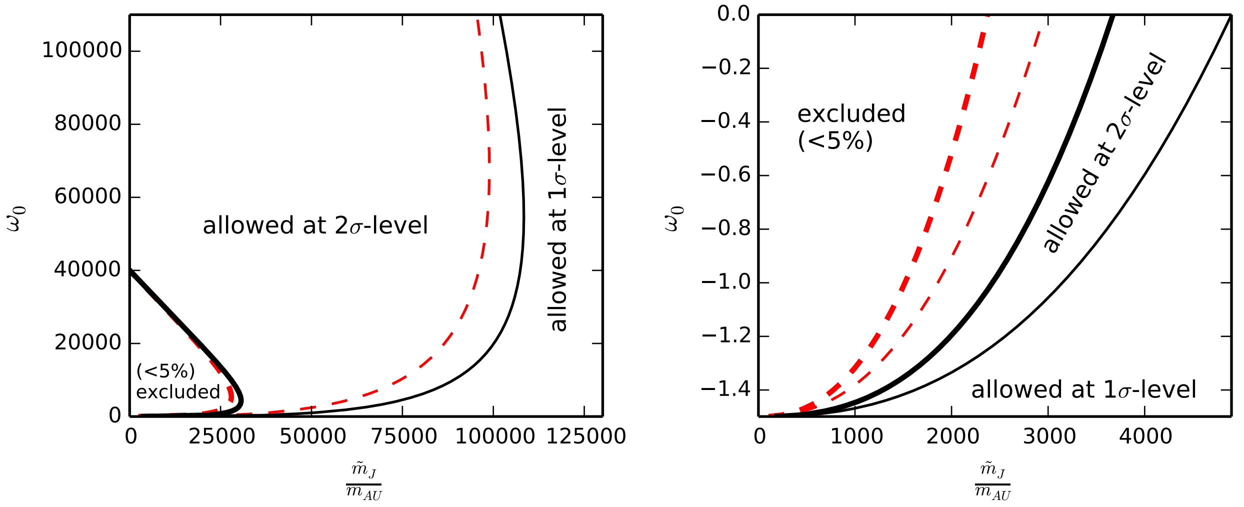

Figure 2.2: Cassini constraint on massive Brans-Dicke theory. The constraint on PPN γ given by the Cassini experiment is used to constrain the $(\tilde{m}_{\mathrm{J}}, \omega_0)$-parameter space for massive Brans-Dicke theory. For this theory, the parameter ξ in the expression for γ is given by (2.62). For the interaction distance we take $\chi - X_{\mathrm{Sun}} = 0.6$ solar radii. The solid lines separate the regions which are excluded (probability $< 5\%$), that are allowed at the 2σ level and at the 1σ level, respectively. The dashed lines show the corresponding boundaries between these regions for the case where the Sun is considered to be a point mass. The x axis shows the ω_0-independent mass $\tilde{m}_{\mathrm{J}}$ in terms of inverse astronomical units $m_{\mathrm{AU}} = 1/\mathrm{AU}$, the y-axis shows ω_0.

The exterior scalar field generated by a compact object like a planet or a star is determined only by the very outer layer of the object, we say that it has a thin shell. It is shown in [17, 18] that the exterior field is

$$\phi(r) = \phi_0 - 3\delta\sqrt{2}k\frac{GM_{\mathrm{E}}}{r}e^{-m_{\mathrm{E}}(r-R)}, \tag{2.64}$$

where $\delta := \Delta R/R \ll 1$ is the thin shell parameter. The chameleon field profile corresponds to the field (2.50) with $\xi = 3\delta$, giving the parameter

$$\gamma(r) = \frac{1 - 6\delta k^2 e^{-m_{\mathrm{E}}(r-R)}}{1 + 6\delta k^2 e^{-m_{\mathrm{E}}(r-R)}}. \tag{2.65}$$

This is the same result as found in [13]. Furthermore, $\beta = 1$ holds since the coupling is mediated by an exponential function.

The thin shell factor is proportional to $(\phi_\infty - \phi_c)/k\Phi_c$ where $\Phi_c = GM/R$ is the Newtonian potential of an object at its surface or, in other words, its compactness. ϕ_c and ϕ_∞ are the field values inside and infinitely far away from the compact object. They are density dependent and therefore the thin shell parameter depends on the composition of an object. Typically, it holds that $\phi_\infty \gg \phi_c$, such that approximately $\delta \sim \phi_\infty/k\Phi_c$, allowing us to compare the ability of testing chameleons around different compact objects in the Solar System just by comparing their Newtonian potentials Φ_c. From this point of view, the Sun is not a promising candidate to probe chameleons due to its high compactness. The Earth, and even better the Moon, are more appropriate.

The Cassini experiment can be used to constrain the $(\delta_{\mathrm{Sun}}, m_{\mathrm{E}})$-parameter space for fixed k using Eq. (2.65). For $k \sim 1$ and small masses for the scalar field, this constrains δ_{Sun} to the 10^{-6} level. For larger masses the thin-shell factor may take much larger values. A constraint on γ in Earth's orbit would produce the analogous result but for the thin-shell factor of the Earth.

It is important to keep in mind that also a satellite which aims to probe gravity is not a test mass and can therefore acquire a thin shell itself. This would further suppress any GR-violating signals. Khoury and Weltman estimate that a typical satellite does not have a thin shell if the condition $10^{-15} < \delta < 10^{-7}$ is satisfied [17, 18].

In [13] it is argued that chameleons are ruled out due to the incompatibility of solar system and cosmological constraints. But anyway, they provide an interesting example of a theory predicting deviations from general relativity which depend not only on the distance from some massive object but also on its mass, radius and composition. It is not only important to probe gravity to high levels of accuracy, but also around different celestial bodies.

2.1.4 Measuring PPN parameters in Earth's exterior field

In 2016, the Atomic Clock Ensemble in Space (ACES) mission will place an atomic clock on the International Space Station (ISS) that is expected to reach a fractional frequency uncertainty of $\Delta f/f \sim 10^{-16}$ [22]. In the future, space clocks will continue to improve. After ACES, there are plans to put an optical clock on the ISS as part of the Space Optical Clock project. The best optical clocks on Earth have already reached accuracies of $\Delta f/f \sim 10^{-18}$ over an integration period of 25000 sec [33, 34], and significant progress is being made towards building optical clocks that are mobile, more compact and more reliable.

In this section, we investigate the effect that the PPN parameters have on a satellite that carries an atomic clock and orbits the Earth. In this experiment, a precise clock on a satellite broadcasts tick signals down to a terrestrial receiving station which records their arrival times using a local, more accurate clock. The rate at which the ticks arrive is the redshift. This setup allows the orbit to be tracked down to the clock accuracy. For given Keplerian initial conditions, we simulate both the general relativistic orbit as well as the orbit in an alternative theory of gravity with parameters different from those of general relativity. This solves the forward problem, and taking the difference of these two signals provides a way to give upper limits on how well the PPN parameters can be constrained by this type of mission. To investigate PPN parameter predictability more thoroughly, the full inverse problem needs to be solved, which entails reconstructing the full four-dimensional trajectory of the satellite by fitting different models to redshift data. Mock redshift data can be generated from solutions to the forward problem with different parameters and added noise. We leave attempts to solve the inverse problem to future work.

We choose an eccentric orbit like that originally proposed for STE-QUEST [23]. We solve the forward problem using the code introduced by Angélil *et al.* [3, 35]. Note that the effects that the PPN parameters have on the orbit dominate, while their effects on the light path between the emitter and the receiver are about 2 orders of magnitude smaller [3, 35].

The trajectory of a spacecraft in Earth's external field is found by integrating Hamilton's equations. We have seen that for general scalar-tensor theories the PPN parameters depend on the location where they are tested. If the potential is set to zero, making the field massless, the PPN parameters γ and

β are constant (see section 2.1.3.2). The corresponding metric in the Jordan frame is

$$g_{tt} = -1 + \frac{2GM}{r}\epsilon - \frac{2G^2M^2}{r^2}(\beta - \gamma)\,\epsilon^2 \tag{2.66a}$$

$$g_{rr} = 1 + \frac{2GM}{r}\gamma\epsilon \tag{2.66b}$$

$$g_{\theta\theta} = r^2 \tag{2.66c}$$

$$g_{\varphi\varphi} = r^2 \sin^2\theta, \tag{2.66d}$$

where we consider nonisotropic Schwarzschild coordinates. (We write r instead of χ for the radial coordinate and drop all J indices.) This is a special case of (2.72) with $A(r) = 1, B(r) = \beta$ and $C(r) = \gamma$. The corresponding Hamiltonian for a satellite's trajectory in Earth's external field is obtained from (2.74),

$$\begin{aligned} H &= -\frac{p_t^2}{2} + \left[-\frac{GMp_t^2}{r} + \frac{p_r^2}{2} + \frac{p_\theta^2}{2r^2} + \frac{p_\varphi^2}{2r^2\sin^2\theta}\right]\epsilon + \left[-\frac{2G^2M^2p_t^2}{r^2}\left(1 - \frac{1}{2}\beta + \frac{1}{2}\gamma\right) - \frac{GMp_r^2}{r}\gamma\right]\epsilon^2 \\ &= -\frac{p_t^2}{2} + \left[-\frac{GMp_t^2}{r} + \frac{\boldsymbol{p}^2}{2}\right]\epsilon + \left[-\frac{2G^2M^2p_t^2}{r^2}\left(1 - \frac{1}{2}\beta + \frac{1}{2}\gamma\right) - \frac{GM}{r}\frac{(\boldsymbol{x}\cdot\boldsymbol{p})^2}{r^2}\gamma\right]\epsilon^2, \end{aligned} \tag{2.67}$$

where we change to Cartesian coordinates in the second line. Notice that β does not show up individually, but only in combination with γ. The equations of motion are given by Hamilton's equations.

We specify the orbit by choosing Keplerian initial conditions. We position the Earth clock beneath perihelion, the satellite's point of closest approach. Hamilton's equations are integrated over 4.5 orbits, once for the general relativistic metric ($\gamma = \beta = 1$), giving the redshift signal z_{GR}, and then for one where these parameters slightly differ from unity, giving $z_{\text{non-GR}}$. Taking the difference of the two signals,

$$\Delta z = z_{\text{GR}} - z_{\text{non-GR}}, \tag{2.68}$$

allows us to find the maximum difference in the redshift, $|\Delta z|_{\max}$, averaged over one orbit. Such a difference in the redshift signal should be detectable if this residual redshift is within the accuracy of the experiment.

There are numerous both relativistic and nonrelativistic effects which enter the dynamics that have not been considered here. They will need to be accurately modeled as part of the parameter recovery procedure. Nonrelativistic effects include atmospheric drag, solar radiation pressure and Earth's Newtonian multipole field. Angélil *et al.* (2014) [3] calculate a host of general relativistic effects on the satellite and the light-path trajectories. The γ and β variations discussed in this paper correspond to modified Schwarzschild terms in the Hamiltonian. The standard GR frame-dragging effect, the Shapiro effect (bent light paths), spin-squared effects on the orbit, as well as further yet weaker effects would need to be included when searching for deviations from non-GR values of γ and β. Effects that come into play at different orders (refer to different blocks in Table 1 in [3]) will not be degenerate with one another due to their fundamentally different r dependence, provided the satellite trajectory is elliptical, inducing a sufficient field strength modulation over the course of the integration time. Further discussion on these effects may also be found in [36].

In our approach, where we subtract the redshift signal predicted by general relativity from that with different PPN parameters, all these effects will cancel out in the subtraction process. A further approximation made is to allow the Earth to be transparent to the tick signals. In reality, however, certain portions of the experiment would miss data during line-of-sight loss. This would be in part

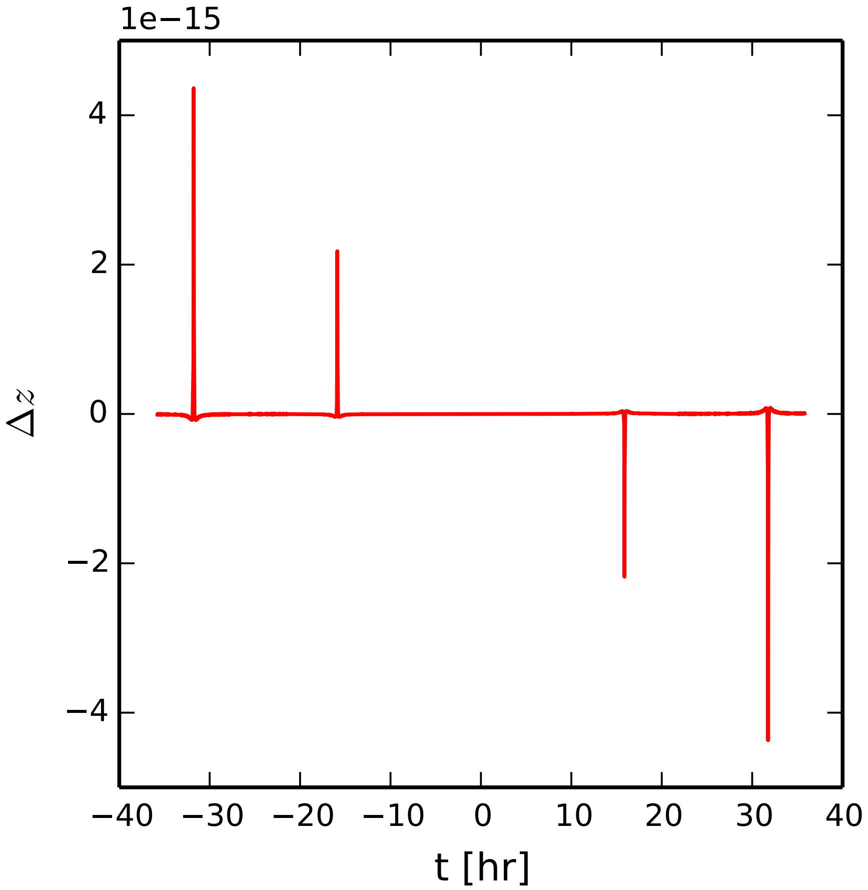

Figure 2.3: Difference in redshift curve. The difference in the redshift signal between the GR orbit and the orbit with $\gamma = 1 + 10^{-5}$ and $\beta = 1$, $\Delta z = z_{\mathrm{GR}} - z_{\text{non-GR}}$, is plotted as a function of time t (in hours).

compensated by having multiple ground stations so that at any given point a clock on Earth will be within the satellite's line of sight.

We choose an eccentric orbit with semimajor axis $a = 32090\,\mathrm{km}$ and eccentricity $e = 0.779$. Such an orbit has a perihelion distance of 7092 km, corresponding to an altitude of about 700 km above ground. This orbit was chosen for the original proposal of the satellite mission STE-QUEST [23] and we take it as our reference orbit. We then compare the general relativity orbit to the orbit with PPN parameters differing from unity by subtracting the redshift signal of the modified orbit from the general relativistic orbit. Fig. 2.3 shows the result for the choice $\gamma = 1 + 10^{-5}$, $\beta = 1$.

We find that the difference peaks around pericenter, and builds up with every orbit. For just one orbit we can read off the maximum difference in redshift $\Delta z = 2 \times 10^{-15}$.

The absolute value of the maximum difference in the redshift signal over one orbit, indicated by its color/grey scale, is plotted for a range of parameters in Fig. 2.4. It is evident that, theoretically, using a clock of accuracy $\Delta f/f \sim 10^{-16}$ one should be able to constrain $|\gamma - 1| \sim |\beta - 1| \sim 10^{-6}$.

Along lines with $\beta - \gamma =$ constant the absolute value of the signal is the same. This comes from the fact that the signal is mainly caused by the term in the Hamiltonian (2.67) proportional to $\tilde{\beta} := 1 - (\beta - \gamma)/2$, while the effect of the one proportional to γ is negligible. Therefore, $|\tilde{\beta} - 1|$ remains the same if β and γ are interchanged, while the sign of the difference in the redshift signal

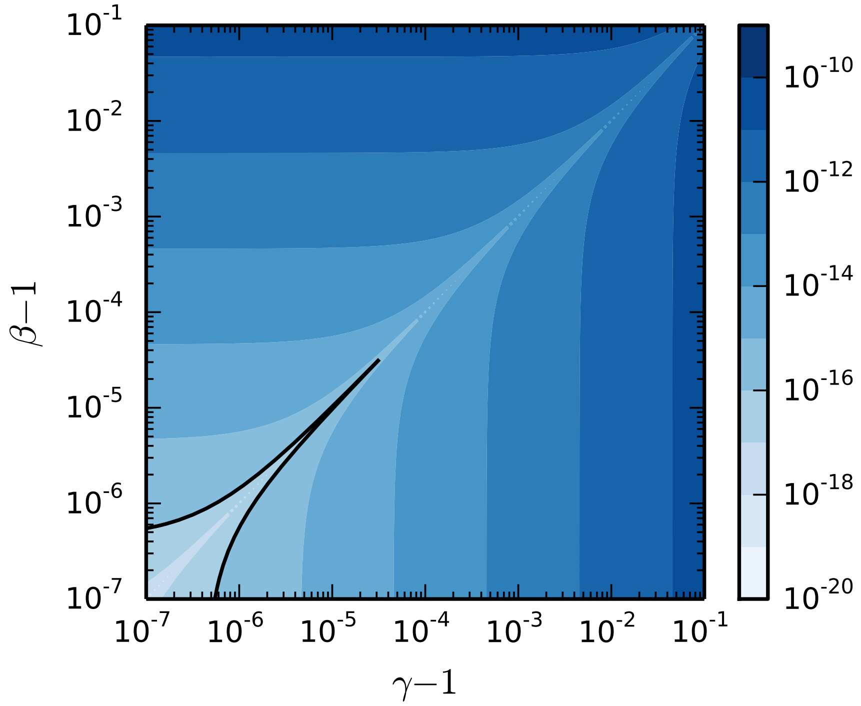

Figure 2.4: Logarithmic parameter space plot. This parameter space plot shows the maximum difference in the redshift between the GR orbit and that for a range of positive values for γ and β over one orbit. The solid line corresponds to the value 10^{-16}. For the orbit we chose our reference orbit.

flips.

Thus, having a clock on our reference orbit would allow to perform interesting tests of gravitational effects. It is instructive to examine several kinds of orbits to see which ones provide the strongest residuals. On the one hand, we want the satellite to pass by the Earth closely, therefore having a small pericenter distance in order to have strong gravitational effects. On the other hand, it should be far enough to minimize effects as inhomogeneities of the Earth's gravitational potential or atmospheric drag [36]. We fix the pericenter distance at $d = 700\,\mathrm{km}$ above the ground. Then, we vary the eccentricity from a circular orbit $e = 0$ to a highly eccentric orbit $e = 0.9$, or equivalently, we vary the semimajor axis a from the pericenter distance (circular orbit) up to $71000\,\mathrm{km}$. These quantities are related by $d = a(1 - e)$. In Fig. 2.5, the maximum difference in the redshift signal over one orbit between general relativity and some scalar-tensor theories with different $\gamma \neq 1$ are shown as a function of the eccentricity and the semimajor axis. We notice that for increasing eccentricity the magnitude of the signal increases significantly.

Now, we investigate the widths of the peaks of the difference in the redshift signals. The peaks are approximated by fitting a Lorentzian $f(t) = A/(2\pi)\Gamma[(t - t_0)^2 + \Gamma^2/4]^{-1} + d$, an example is shown in Fig. 2.6. From the fit we can easily determine the full width at half maximum. In Fig. 2.5, the peak width is plotted against the eccentricity for the case $\gamma = 1 + 10^{-5}$ and $\beta = 1$. Even though the width decreases for growing eccentricities, its value remains of order ~ 100 seconds: this is the time scale that needs to be resolved in order to find deviations coming from nonunity PPN parameters. While the width depends on the orbit, it is essentially independent of the PPN parameters, as the values change very little in the investigated range.

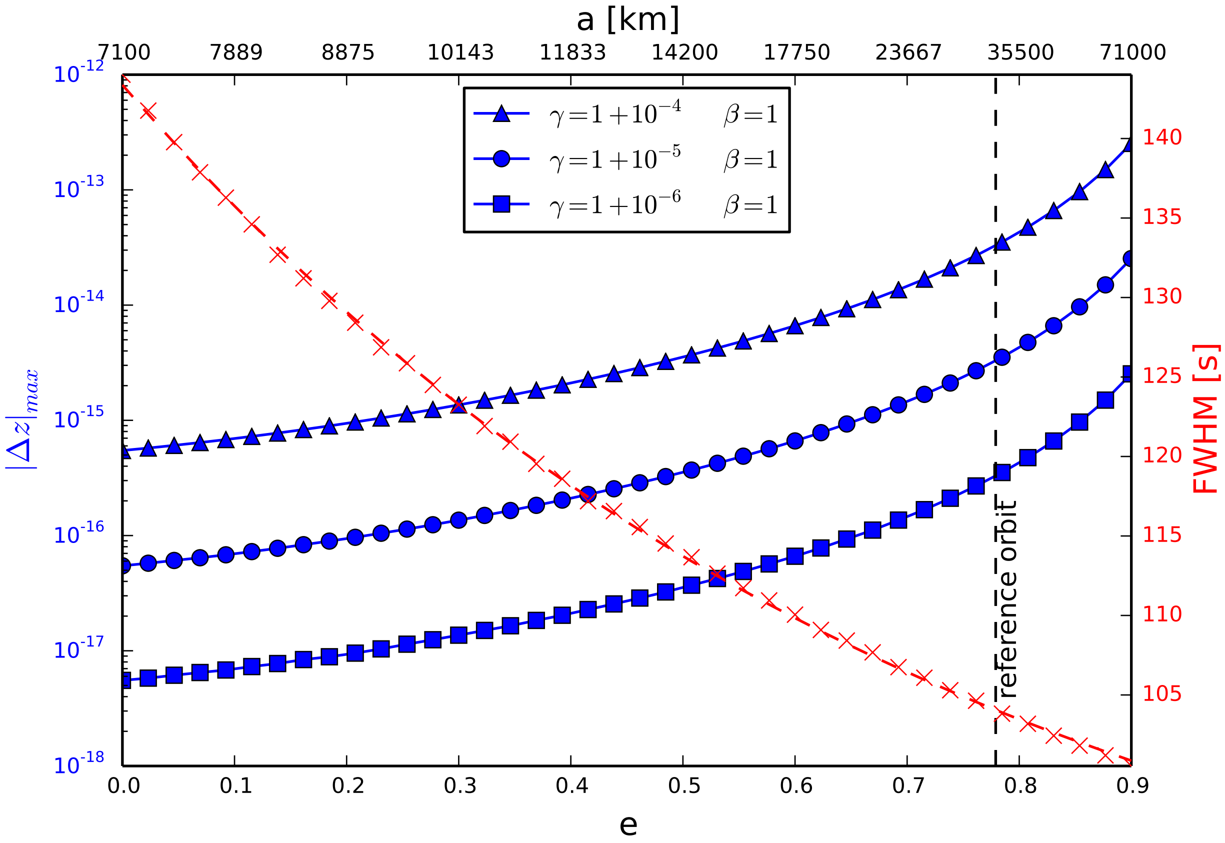

Figure 2.5: Redshift signal and peak width as a function of eccentricity. We compare the GR orbit to ones where γ slightly deviates from one. While the pericenter distance is fixed at $d = 7100\,\text{km}$, i.e., about 700 km above ground, the eccentricity e, or equivalently the semimajor axis a, is changed. The triangle, circle and square data points show the maximum difference in the redshift signal, $|\Delta z|_{\text{max}}$, for one orbit. The cross data points show the full width at half maximum (FWHM) for a signal peak for $\gamma = 1 + 10^{-5}$ and $\beta = 1$. The analogous for other choices of the parameters are omitted since they would yield the same result: the width is essentially constant for varying PPN parameters. We notice that the duration of the peak is of order 100 seconds for all eccentricities. This is the time scale which needs to be resolved to detect possible variations of the PPN parameters from their GR values.

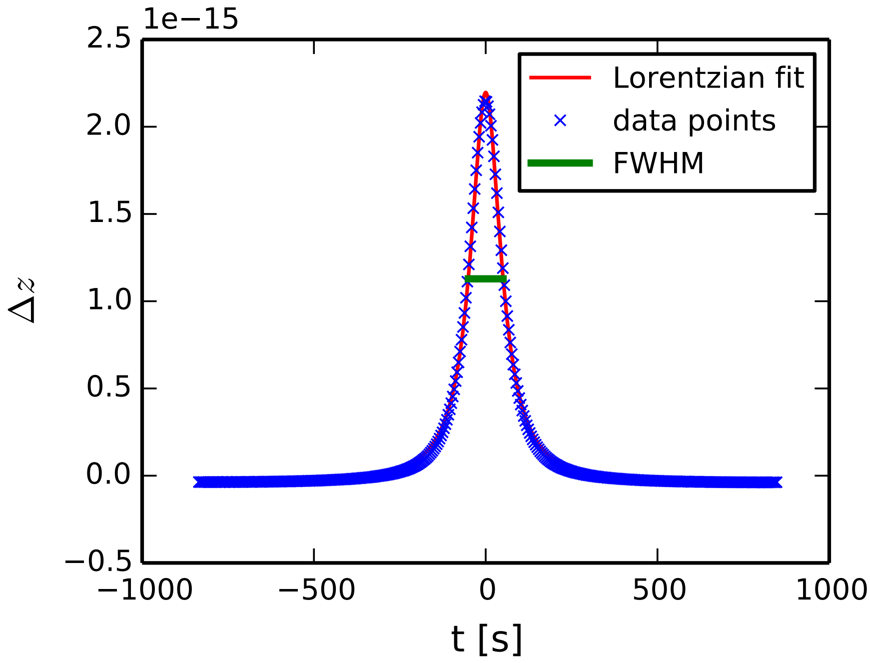

Figure 2.6: Lorentzian fit of a peak. The data points show the difference in the redshift signal between a GR orbit and $\gamma = 1 + 10^{-5}$, $\beta = 1$, as a function of time (in seconds), centered around the pericenter. A Lorentzian $f(t) = A/(2\pi)\Gamma[(t - t_0)^2 + \Gamma^2/4]^{-1} + d$ is fitted, allowing to determine the full width at half maximum.

2.1.5 Conclusions

We calculate the PPN parameters γ and β for scalar-tensor theories formulated in the Einstein frame for the case of a pointlike source. This extends the discussion of such theories in the Jordan frame given in [15, 16]. To discuss tests of gravitation in the vicinity of more realistic sources we introduce a simple formalism which can take into account effects arising from the finite size of the source. We use the Cassini limit on PPN γ to put constraints on this formalism. In particular, we update the constraints on the parameter space of massive Brans-Dicke scalar fields by replacing the assumption of a point source with that of a constant-density sphere. This provides more stringent constraints since the proximity to the source is increased due to the extended radius of the object.

We emphasize that the presence of a scalar potential makes the field finitely ranged and therefore it is crucial to perform tests of gravitation at different distances. Additionally, performing experiments around different sources is particularly interesting because the exterior field profile is likely to depend on properties of an object like its compactness or its composition.

In the second part of the paper we discuss the possibility of testing scalar-tensor theories in Earth orbit using atomic clocks. Their rapid development and the current interest in satellite missions carrying such clocks opens the possibility to perform comprehensive tests of gravitation within the next decade. Such missions will provide constraints on the PPN parameters in the vicinity of the Earth. We calculate the relativistic effects on the satellite orbit coming from non-GR parameters γ and β. High-performance atomic clocks are sensitive to the associated change in the redshift signal. We find that with currently available clock technology and reasonable choices of spacecraft orbits one should be able to constrain $|\gamma - 1| \sim |\beta - 1| \sim 10^{-6}$. Our estimates provide upper limits to PPN parameters that could be measured by a clock in orbit. However, in order to provide more definite answers on possible constraints, one would have to solve the full inverse problem, where the relevant parameters are reconstructed from a redshift signal that contains all relevant effects. We show that a PPN parameter varying from one produces a change in the redshift signal, peaking around pericenter of the eccentric orbit. While the magnitude of the peak is determined by both the value of the parameters and the chosen orbit, its width, and therefore the time scale which needs to be resolved, depends only on the orbit specifications.

2.1.6 Metric in nonisotropic coordinates

The PPN parameters are defined by introducing parameters to the individual terms of the expanded Schwarzschild metric written in isotropic coordinates. But often it is useful to consider the metric expressed in nonisotropic coordinates. This is achieved by defining a new radial coordinate r while the other coordinates remain the same. (Do not confuse the notion of r with the radial coordinate in the Einstein frame used earlier on.) We write the metric in isotropic coordinates in the general form

$$g_{tt} = -\left(1 - \frac{2GM}{\chi}A(\chi)\epsilon + \frac{2G^2M^2}{\chi^2}B(\chi)\epsilon^2\right) + \mathcal{O}(\epsilon^3) : \tag{2.69a}$$

$$g_{\chi\chi} = 1 + \frac{2GM}{\chi}C(\chi)\epsilon + \mathcal{O}(\epsilon^2) \tag{2.69b}$$

$$g_{\theta\theta} = \left(1 + \frac{2GM}{\chi}C(\chi)\epsilon\right)\chi^2 + \mathcal{O}(\epsilon^2) \tag{2.69c}$$

$$g_{\varphi\varphi} = \left(1 + \frac{2GM}{\chi}C(\chi)\epsilon\right)\chi^2\sin^2\theta + \mathcal{O}(\epsilon^2). \tag{2.69d}$$

By introducing a new radial coordinate

$$r := \chi\left(1 + \frac{2GM}{4\chi}C(\chi)\epsilon\right)^2 , \tag{2.70}$$

which can be inverted to (outside the Schwarzschild radius)

$$\chi = r\left(\frac{1}{2} - \frac{GM}{2r}C(r)\epsilon + \frac{1}{2}\sqrt{1 - \frac{2GM}{r}C(r)\epsilon}\right) , \tag{2.71}$$

we obtain

$$g_{tt} = -1 + \frac{2GM}{r}A(r)\epsilon - \frac{2G^2M^2}{r^2}\left[B(r) - A(r)C(r)\right]\epsilon^2 \tag{2.72a}$$

$$g_{rr} = 1 + \frac{2GM}{r}\left[C(r) - C'(r)r\right]\epsilon \tag{2.72b}$$

$$g_{\theta\theta} = r^2 \tag{2.72c}$$

$$g_{\varphi\varphi} = r^2\sin^2\theta. \tag{2.72d}$$

Here, we used that $g_{\chi\chi}d\chi^2 = g_{rr}dr^2$. Transforming to Cartesian coordinates, the metric becomes

$$g_{tt} = -1 + \frac{2GM}{r}A(r)\epsilon - \frac{2G^2M^2}{r^2}\left[B(r) - A(r)C(r)\right]\epsilon^2 \tag{2.73a}$$

$$g_{x_ix_j} = \delta_{ij} + \frac{2GM}{r}\left[C(r) - C'(r)r\right]\frac{x_ix_j}{r^2}\epsilon \tag{2.73b}$$

where we used $F(r)dr^2 + r^2d\theta^2 + r^2\sin^2\theta d\varphi^2 = d\boldsymbol{x}^2 + \left[F(r) - 1\right](\boldsymbol{x}/rd\boldsymbol{x})^2$.

2.1.7 Hamiltonian

The Hamiltonian is given by $H = 1/2 g^{\mu\nu} p_\mu p_\nu$, where p_μ is the canonical four-momentum. Here, we consider the metric (2.72), which we expand in powers of $\epsilon \sim GM/r$. The orbital velocity of a nonrelativistic particle in a weak gravitational field is $v \approx \sqrt{GM/r} \sim \epsilon^{1/2}$, requiring $p_r, p_\theta/r, p_\varphi/(r\sin\theta) \sim v \sim \epsilon^{1/2}$. Plugging the inverse metric into the formula for the Hamiltonian and assigning the terms to the appropriate orders in ϵ yields

$$\begin{aligned} H = &-\frac{p_t^2}{2} + \left[-\frac{GMp_t^2}{r} A(r) + \frac{p_r^2}{2} + \frac{p_\theta^2}{2r^2} + \frac{p_\varphi^2}{2r^2\sin^2\theta} \right] \epsilon \\ &+ \left[-\frac{2G^2M^2p_t^2}{r^2} \left(A(r)^2 - \frac{1}{2}B(r) + \frac{1}{2}A(r)C(r) \right) \right. \\ &\left. -\frac{GMp_r^2}{r} \left(C(r) - rC'(r) \right) \right] \epsilon^2 . \end{aligned} \tag{2.74}$$

From this it is evident why we drop all terms in the spatial metric components that are second and higher order in ϵ: they contribute to the Hamiltonian at third and higher orders. Notice that the expansion of the Hamiltonian for a signal propagating in the same spacetime looks different, since, even though we start with the same Hamiltonian, some terms contribute at different orders. This comes from the fact that photons travel with the speed of light and therefore, $p_t, p_r, p_\theta/r$ and $p_\varphi/(r\sin\theta)$ are of order 1. The equations of motion are given by Hamilton's equations $dp_\mu/d\lambda = -\partial H/\partial x^\mu$ and $dx^\mu/d\lambda = \partial H/\partial p_\mu$.

2.2 Multi scalar-tensor theories

Manuel Hohmann and Andreas Schärer

This paper is work in progress [2].

2.2.1 Introduction

Scalar tensor theories are a class of alternative theories of gravitation. Multi-scalar tensor theories are a further generalization that allows more than one additional scalar degree of freedom to the metric tensor of general relativity. Effective scalar fields can arise e.g. from an underlying theory such as quantum theories of gravity or from compactified extra dimensions.

We consider a general multi-scalar tensor action, expressed in a general frame. I.e., the field is non-minimally coupled to curvature and has an arbitrary potential and coupling to matter.

Alternative theories of gravitation are often discussed in the parametrized post-Newtonian (PPN) approximation. It allows describing such theories in the weak field limit in terms of a number of parameters that might deviate from the parameters predicted by general relativity. The PPN parameters γ and β for single scalar tensor theories have been calculated in the Jordan [37, 38] and in the Einstein frame [1]. For multi-scalar tensor theories, the γ parameter was calculated in [39].

Applying conformal transformations and scalar field redefinitions allows to switch between different physically equivalent frames. This motivates the definition of quantities that are invariant under said transformations [40, 41]. First, we develop a geometric description of multi-scalar tensor theories in terms of such invariants. Second, we want to calculate the β parameter for multi-scalar tensor theories. To calculate the PPN parameters in the single scalar field case [1, 37, 38], the source mass was assumed to be a point source. It turns out that this leads to problems with the boundary conditions for the solutions of the higher order scalar and metric field equations - in both the single and the multi-scalar field case. We argue that the assumption of a point source is not appropriate. We try to circumvent this problem by considering a more realistic source.

2.2.2 Action and field equations

The action of a multi-scalar tensor theory expressed in a general frame is

$$S = \frac{1}{2\kappa^2}\int d^4x\sqrt{-g}\,\Big(\mathcal{A}(\Phi)R - \mathcal{B}_{AB}(\Phi)g^{\mu\nu}\partial_\mu\Phi^A\partial_\nu\Phi^B - 2\kappa^2\mathcal{U}(\Phi)\Big) + S_m[e^{2\alpha(\Phi)}g_{\mu\nu}, \chi]. \qquad (2.75)$$

We consider N scalar fields Φ^α, labeled by indices $\alpha, \beta, \gamma, ... = 1, ..., N$ and by Φ we note the collection of scalar fields $\Phi = (\Phi^1, ..., \Phi^N)$. They couple non-minimally to the Ricci scalar R via the function $\mathcal{A}$. The symmetric $N \times N$ matrix $\mathcal{B}_{AB}$ represents the kinetic coupling of the scalar fields and will later help to define a metric on the scalar field space. The presence of a scalar potential $\mathcal{U}$ will lead to massive scalar fields.

We use $c = \hbar = 1$ units, s.t. [time] = [length] = [mass]$^{-1}$. Then, R has units of [length]$^{-2}$, ∇_μ has dimension [length]$^{-1}$ and the constant $\kappa^2 = \frac{8\pi G}{\hbar c}$ has units of [length]^2. $\mathcal{A}, \alpha, \mathcal{U}, \mathcal{B}_{AB}$ shall be dimensionelss and therefore l must be of dimension [length].

The last term is the matter part of the action. The matter fields are denoted by χ and they couple to matter via the metric $e^{2\alpha(\Phi)}g_{\mu\nu}$. Note that this is not the frame metric $g_{\mu\nu}$ but one that is conformally related.

Often, scalar-tensor theories are expressed in either the Jordan or the Einstein frame.

If $\alpha = 0$, we say that we are in the Jordan frame. The advantage is that the Jordan frame metric can be viewed as the ‘physical’ metric since matter fields couple to this metric directly and therefore it follows geodesics of this metric.

The Einstein frame is obtained by choosing $\mathcal{A} = 1$. Then, the scalar field is minimally coupled and the curvature part in the metric looks exactly like the Einstein-Hilbert action in general relativity. This simplifies the field equations significantly compared to the Jordan or a general frame.

It will turn out to be useful to introduce the quantity

$$\mathcal{F}_{AB} \equiv \frac{2\mathcal{A}\mathcal{B}_{AB} + 3\mathcal{A}_{,A}\mathcal{A}_{,B}}{4\mathcal{A}^2}. \tag{2.76}$$

The metric field equations are obtained by varying the action (2.75) w.r.t. the metric. Written in the trace-reversed form it is

$$\begin{aligned} R_{\mu\nu} &- \frac{\mathcal{A}_{,A}}{\mathcal{A}}\left(\nabla_\mu\nabla_\nu\Phi^A + \frac{1}{2}g_{\mu\nu}\Box\Phi^A\right) - \left(\frac{\mathcal{A}_{,AB}}{\mathcal{A}} + 2\mathcal{F}_{AB} - \frac{3\mathcal{A}_{,A}\mathcal{A}_{,B}}{2\mathcal{A}^2}\right)\partial_\mu\Phi^A\partial_\nu\Phi^B \\ &- \frac{1}{2}g_{\mu\nu}\frac{\mathcal{A}_{,AB}}{\mathcal{A}}g^{\rho\sigma}\partial_\rho\Phi^A\partial_\sigma\Phi^B - \frac{1}{\mathcal{A}}g_{\mu\nu}\kappa^2\mathcal{U} = \frac{\kappa^2}{\mathcal{A}}\left(T_{\mu\nu} - \frac{1}{2}g_{\mu\nu}T\right)\,, \end{aligned} \tag{2.77}$$

where we introduced the notation $X_{,A} \equiv \frac{\partial X}{\partial\Phi^A}, X_{,AB} \equiv \frac{\partial^2 X}{\partial\Phi^A\partial\Phi^B}$ and the d’Alembertian $\Box X \equiv \nabla^2 X = g^{\mu\nu}\nabla_\mu\nabla_\nu X$. Taking the variation w.r.t. the scalar field gives the scalar field equation

$$\begin{aligned} \mathcal{F}_{AB}\Box\Phi^B &+ \frac{1}{2}\left(\mathcal{F}_{AB,C} + \mathcal{F}_{AC,B} - \mathcal{F}_{BC,A} + 2\mathcal{F}_{AB}\frac{\mathcal{A}_{,C}}{\mathcal{A}}\right)g^{\mu\nu}\partial_\mu\Phi^B\partial_\nu\Phi^C \\ &+ \frac{1}{\mathcal{A}^2}\frac{\partial\mathcal{A}}{\partial\Phi^A}\kappa^2\mathcal{U} - \frac{1}{2\mathcal{A}}\kappa^2\frac{\partial\mathcal{U}}{\partial\Phi^A} = -\frac{1}{\mathcal{A}}\mathcal{K}_A T\,. \end{aligned} \tag{2.78}$$

2.2.3 Geometric description

2.2.3.1 Spaces, maps and coordinates

We consider a spacetime manifold M (usually 4-dimensional) and a scalar field manifold Q of dimension N. The set of scalar fields is then described by a map $\Phi : M \to Q$. On M we use coordinates (x^μ), while on Q we use coordinates (X^A). For the scalar fields in these coordinates we also use the notation $\Phi^A = X^A \circ \Phi$. For the coordinate vector fields we introduce the notation

$$\partial_\mu = \frac{\partial}{\partial x^\mu}\,, \quad \eth_A = \frac{\partial}{\partial X^A}\,. \tag{2.79}$$

Further, we introduce induced coordinates (x^μ, y^μ) and (X^A, Y^A) on the tangent bundles TM and TQ such that

$$(x, y) = y^\mu\partial_\mu \in T_xM\,, \quad (X, Y) = Y^A\eth_A \in T_XQ\,. \tag{2.80}$$

For the corresponding coordinate vector fields on TM and TQ we write

$$\partial_\mu = \frac{\partial}{\partial x^\mu}\,, \quad \bar{\partial}_\mu = \frac{\partial}{\partial y^\mu}\,, \quad \eth_A = \frac{\partial}{\partial X^A}\,, \quad \bar{\eth}_A = \frac{\partial}{\partial Y^A}\,. \tag{2.81}$$

Finally, we introduce induced coordinates $(x^\mu, y^\mu, u^\mu, v^\mu)$ and (X^A, Y^A, U^A, V^A) on TTM and TTQ in the same way as we did on TM and TQ, i.e.,

$$(x, y, u, v) = u^\mu\partial_\mu + v^\mu\bar{\partial}_\mu \in T_{(x,y)}TM\,, \quad (X, Y, U, V) = U^A\eth_A + V^A\bar{\eth}_A \in T_{(X,Y)}TQ\,. \tag{2.82}$$

2.2.3.2 Invariant quantities

A (multi)-scalar tensor theory can equivalently be expressed in a different frame by applying a Wely transformation of the metric tensor $g_{\mu\nu} \to \bar{g}_{\mu\nu}$ and a reparametrization of the scalar fields $\Phi \to \bar{\Phi}$

$$g_{\mu\nu} = e^{2\bar{\gamma}(\bar{\Phi})}\bar{g}_{\mu\nu}\,, \tag{2.83a}$$

$$\Phi^A = \bar{f}^A(\bar{\Phi})\,. \tag{2.83b}$$

For derivatives w.r.t. a scalar field it follows:

$$\frac{\partial}{\partial\bar{\Phi}^A} = \frac{\partial\Phi^B}{\partial\bar{\Phi}^A}\frac{\partial}{\partial\Phi^B} = \bar{f}^B_{,A}\frac{\partial}{\partial\Phi^B} \tag{2.84a}$$

$$\frac{\partial}{\partial\Phi^A} = \frac{\partial\bar{\Phi}^B}{\partial\Phi^A}\frac{\partial}{\partial\bar{\Phi}^B} = (\bar{f}^B_{,A})^{-1}\frac{\partial}{\partial\bar{\Phi}^B}\,. \tag{2.84b}$$

Under these transformations, the quantities defining the theory transform as

$$\mathcal{A}(\Phi(\bar{\Phi})) = e^{-2\bar{\gamma}(\bar{\Phi})}\bar{\mathcal{A}}(\bar{\Phi}) \tag{2.85a}$$

$$\mathcal{U}(\Phi(\bar{\Phi})) = e^{-4\bar{\gamma}(\bar{\Phi})}\bar{\mathcal{U}}(\bar{\Phi}) \tag{2.85b}$$

$$\alpha(\Phi(\bar{\Phi})) = \bar{\alpha}(\bar{\Phi}) - \bar{\gamma}(\bar{\Phi}) \tag{2.85c}$$

$$\begin{aligned}\mathcal{B}_{AB}(\Phi(\bar{\Phi})) &= e^{-2\bar{\gamma}(\bar{\Phi})}(\bar{f}^C_{,A})^{-1}(\bar{f}^D_{,B})^{-1} \\ &\quad\times\left(\bar{\mathcal{B}}_{CD}(\bar{\Phi}) - 6\bar{\gamma}_{,C}\bar{\gamma}_{,D}\bar{\mathcal{A}}(\bar{\Phi}) + 3\left(\bar{\gamma}_{,C}\bar{\mathcal{A}}_{,D} + \bar{\gamma}_{,D}\bar{\mathcal{A}}_{,C}\right)\right).\end{aligned} \tag{2.85d}$$

In order to have a frame independent description, we want to express everything in terms of invariants, i.e., quantities that are invariant under the transformations (2.83).

On Q we have two invariant functions [40]

$$\begin{aligned} \mathcal{I}_1 : Q &\to \mathbb{R} & \qquad \mathcal{I}_2 : Q &\to \mathbb{R} \\ X &\mapsto \mathcal{I}_1(X) = \tfrac{e^{2\alpha(X)}}{\mathcal{A}(X)}\,, & X &\mapsto \mathcal{I}_2(X) = \tfrac{\mathcal{U}(X)}{\mathcal{A}^2(X)}\,. \end{aligned} \tag{2.86}$$

Finally, on M we define the invariant metrics

$$g^{\mathfrak{E}}_{\mu\nu} = (\mathcal{A}\circ\Phi)g_{\mu\nu}\,, \quad g^{\mathfrak{J}}_{\mu\nu} = e^{2(\alpha\circ\Phi)}g_{\mu\nu}\,. \tag{2.87}$$

These metrices are labeled with an $\mathfrak{E}$ and a $\mathfrak{J}$ since they resemble the Einstein and the Jordan frame metric, respectively. Note that we are given an action in an arbitrary frame (2.75) with a general metric $g_{\mu\nu}$. For any such metric we can define the corresponding Einstein and Jordan frame metric above. Doing the calculation in the frame given by the metric $g^{\mathfrak{E}}_{\mu\nu}$ gives the benefit of the simplified math of the Einstein frame, even though we consider a theory in an arbitrary frame.

Similarly, we wish to find a metric on the scalar field space Q. A first guess could be $\mathcal{B}_{AB}$, but it does not transform covariantly under the transformations (2.83) as seen in Eq. (2.85d). Therefore, we need a (dimensionless) quantity that is related to $\mathcal{B}_{AB}$ and satisfies the required transformation properties. Actually, this is exactly given by F_{AB} defined in (2.76) and it can be checked that

$$\mathcal{F}_{AB} = (\bar{f}^C_{,A})^{-1}(\bar{f}^D_{,B})^{-1}\bar{\mathcal{F}}_{CD}, \tag{2.88}$$

i.e., $\mathcal{F}_{AB}$ transforms as a tensor under scalar field redefinition and is invariant under Weyl transformation.

So, we can define the metric

$$\mathfrak{G}^{\mathfrak{E}}_{AB} = \mathcal{F}_{AB} \tag{2.89}$$

on Q. There is a second such invariant metric

$$\begin{aligned}\mathfrak{G}^{\mathfrak{J}}_{AB} = \mathfrak{G}_{AB} = e^{-2\alpha}\left[\mathcal{B}_{AB} - 6\mathcal{A}\alpha_{,A}\alpha_{,B} + 3(\mathcal{A}_{,A}\alpha_{,B} + \mathcal{A}_{,B}\alpha_{,A})\right] \\ = \frac{4\mathcal{F}_{AB} - 3(\ln\mathcal{I}_1)_{,A}(\ln\mathcal{I}_1)_{,B}}{2\mathcal{I}_1}\,.\end{aligned} \tag{2.90}$$

2.2.3.3 Derivatives of the scalar fields

First derivative: We have for $\Phi : M \to Q$,as for every map, the pushforward

$$\begin{aligned}\Phi_* : \quad & TM \to TQ \\ & y^\mu\partial_\mu|_x \mapsto y^\mu\partial_\mu\Phi^A\eth_A|_{\Phi(x)}\end{aligned}\,. \tag{2.91}$$

Note that the pushforward is not an arbitrary map, but a vector bundle morphism covering Φ, so that for every $x \in M$ it defines a linear map

$$\Phi_{*x} : T_xM \to T_{\Phi(x)}Q\,. \tag{2.92}$$

Hence, we can regard the pushforward as a section of the homomorphism bundle

$$\mathrm{Hom}(TM, \Phi^*TQ) \cong \Phi^*TQ \otimes T^*M \tag{2.93}$$

of the tangent bundle TM and the pullback bundle Φ^*TQ, and we denote this section by $D\Phi$. Using the latter expression for this bundle, we can write the pullback in coordinates as

$$D\Phi = D_\mu\Phi^A\,\eth_A \otimes dx^\mu = \partial_\mu\Phi^A\,\eth_A \otimes dx^\mu\,, \tag{2.94}$$

where we have slightly abused the notation and written $\eth_A$ for the basis vector fields of the pullback bundle Φ^*TQ.

Second derivative: Analogous to the first derivative, we now aim to construct a section of the bundle

$$\Phi^*TQ \otimes T^*M \otimes T^*M \tag{2.95}$$

from the second pushforward

$$\begin{aligned}\Phi_{**} : \quad & TTM \to TTQ \\ & (u^\mu\partial_\mu + v^\mu\bar{\partial}_\mu)|_{(x,y)} \mapsto \left[u^\mu\partial_\mu\Phi^A\eth_A + (v^\mu\partial_\mu\Phi^A + y^\mu u^\nu\partial_\mu\partial_\nu\Phi^A)\bar{\eth}_A\right]\Big|_{\Phi_*(x,y)}\end{aligned}\,. \tag{2.96}$$

However, for this we need a number of additional structures. In particular, we need the tangent bundles TM and TQ to be equipped with linear connections, which give rise to the following maps. On M we consider the horizontal lift

$$\begin{aligned}\uparrow^h : \quad & TM \times_M TM \to TTM \\ & (y,v)|_x = (y^\mu\partial_\mu, v^\mu\partial_\mu)_x \mapsto (y,v)|^h_x = (v^\mu\partial_\mu - \Gamma^\rho{}_{\nu\mu}y^\nu v^\mu\bar{\partial}_\rho)|_{(x,y)}\end{aligned}\,, \tag{2.97}$$

where $\Gamma^\rho{}_{\nu\mu}$ denotes the connection coefficients of a connection on M. On Q we consider the vertical projection

$$\begin{aligned}\mathbf{v} : \quad & TTQ \to TQ \times_Q TQ \\ & (U^A\partial_A + V^A\bar{\partial}_A)|_{(X,Y)} \mapsto \left(Y^A\partial_A, [V^A + \Gamma^A{}_{BC}Y^BU^C]\partial_A\right)\Big|_X\end{aligned} \tag{2.98}$$

with the connection coefficients $\Gamma^A{}_{BC}$ on Q. Together with the projector pr_2 onto the second factor we then construct the map

$$\begin{aligned}\Phi_{*^2} : TM \times_M TM &\to TQ \\ (y,v)|_x &\mapsto (\mathrm{pr}_2 \circ \mathbf{v} \circ \Phi_{**} \circ \uparrow^h)(y,v)|_x\end{aligned} . \tag{2.99}$$

One easily checks that

$$\begin{aligned}\Phi_{*^2}(y,v)|_x &= (\mathrm{pr}_2 \circ \mathbf{v} \circ \Phi_{**} \circ \uparrow^h)(y,v)|_x \\ &= (\mathrm{pr}_2 \circ \mathbf{v} \circ \Phi_{**})(v^\mu \partial_\mu - \Gamma^\rho{}_{\nu\mu} y^\nu v^\mu \bar{\partial}_\rho)|_{(x,y)} \\ &= (\mathrm{pr}_2 \circ \mathbf{v}) \left[v^\mu \partial_\mu \Phi^A \eth_A + (y^\nu v^\mu \partial_\mu \partial_\nu \Phi^A - \Gamma^\rho{}_{\nu\mu} y^\nu v^\mu \partial_\rho \Phi^A) \bar{\eth}_A\right]\Big|_{\Phi_*(x,y)} \\ &= y^\nu v^\mu \left(\partial_\mu \partial_\nu \Phi^A - \Gamma^\rho{}_{\nu\mu} \partial_\rho \Phi^A + \Gamma^A{}_{CB} \partial_\mu \Phi^B \partial_\nu \Phi^C\right) \eth_A|_{\Phi(x)} .\end{aligned} \tag{2.100}$$

Note that this result is multilinear in the two tangent vectors, and hence defines a section

$$\begin{aligned}D^2\Phi &= D_\mu D_\nu \Phi^A \, \eth_A \otimes dx^\nu \otimes dx^\mu \\ &= \left(\partial_\mu \partial_\nu \Phi^A - \Gamma^\rho{}_{\nu\mu} \partial_\rho \Phi^A + \Gamma^A{}_{CB} \partial_\mu \Phi^B \partial_\nu \Phi^C\right) \eth_A \otimes dx^\nu \otimes dx^\mu\end{aligned} \tag{2.101}$$

of $\Phi^*TQ \otimes T^*M \otimes T^*M$, as we intended to construct.

Chain rule: Given a function $f : Q \to \mathbb{R}$, one easily checks the chain rule

$$\nabla_\mu (f \circ \Phi) = D_\mu \Phi^A \nabla_A f \tag{2.102}$$

and

$$\nabla_\mu \nabla_\nu (f \circ \Phi) = D_\mu D_\nu \Phi^A \nabla_A f + D_\mu \Phi^A D_\nu \Phi^B \nabla_A \nabla_B f . \tag{2.103}$$

2.2.3.4 Relations between invariants

Metrics on M: The invariant metrics on M are related by

$$g^{\mathfrak{J}}_{\mu\nu} = \mathcal{I}_1 g^{\mathfrak{E}}_{\mu\nu} \quad \Rightarrow \quad g^{\mathfrak{E}\,\mu\nu} = \mathcal{I}_1 g^{\mathfrak{J}\,\mu\nu} . \tag{2.104}$$

Hence, the connection coefficients are related by

$$\Gamma^{\mathfrak{J}\,\rho}{}_{\mu\nu} = \Gamma^{\mathfrak{E}\,\rho}{}_{\mu\nu} + \frac{1}{2}\left(\delta^\rho_\nu \partial_\mu \Phi^A + \delta^\rho_\mu \partial_\nu \Phi^A - g^{\mathfrak{E}\,\rho\sigma} g^{\mathfrak{E}}_{\mu\nu} \partial_\sigma \Phi^A\right) (\ln \mathcal{I}_1)_{,A} . \tag{2.105}$$

Metrics on Q: For the invariant metrics on Q holds

$$\mathfrak{G}^{\mathfrak{J}}_{AB} = \frac{4\mathfrak{G}^{\mathfrak{E}}_{AB} - 3(\ln \mathcal{I}_1)_{,A} (\ln \mathcal{I}_1)_{,B}}{2\mathcal{I}_1} . \tag{2.106}$$

Hence, its inverse is given by

$$G^{\mathfrak{J}\,AB} = \frac{\mathcal{I}_1}{2}\left[G^{\mathfrak{E}\,AB} + \frac{3G^{\mathfrak{E}\,AC} G^{\mathfrak{E}\,BD} (\ln \mathcal{I}_1)_{,C} (\ln \mathcal{I}_1)_{,D}}{4 - 3G^{\mathfrak{E}\,EF} (\ln \mathcal{I}_1)_{,E} (\ln \mathcal{I}_1)_{,F}}\right] . \tag{2.107}$$

The connection coefficients are then related by

$$\begin{aligned}\Gamma^{\mathfrak{J}\,C}{}_{AB} &= \Gamma^{\mathfrak{E}\,C}{}_{AB} - \delta^C_{(A} (\ln \mathcal{I}_1)_{,B)} \\ &\quad + \frac{G^{\mathfrak{E}\,CD} (\ln \mathcal{I}_1)_{,D}}{4 - 3G^{\mathfrak{E}\,EF} (\ln \mathcal{I}_1)_{,E} (\ln \mathcal{I}_1)_{,F}} \left(2\mathfrak{G}^{\mathfrak{E}}_{AB} - 3\nabla^{\mathfrak{E}}_A \nabla^{\mathfrak{E}}_B (\ln \mathcal{I}_1) - \frac{3}{2} (\ln \mathcal{I}_1)_{,A} (\ln \mathcal{I}_1)_{,B}\right) .\end{aligned} \tag{2.108}$$

2.2.3.5 Action in terms of geometry

Metric field equation: The left hand side of the metric field equation (2.77) can be written as

$$\begin{aligned} R^{\mathfrak{E}}_{\mu\nu} - 2\mathfrak{G}^{\mathfrak{E}}_{AB}\partial_\mu\Phi^A\partial_\nu\Phi^B - \kappa^2 g^{\mathfrak{E}}_{\mu\nu}\mathcal{I}_2 &= R_{\mu\nu} - \frac{\mathcal{A}_{,A}}{\mathcal{A}}\left(\nabla_\mu\nabla_\nu\Phi^A + \frac{1}{2}g_{\mu\nu}\Box\Phi^A\right) \\ &- \left(\frac{\mathcal{A}_{,AB}}{\mathcal{A}} + 2\mathcal{F}_{AB} - \frac{3\mathcal{A}_{,A}\mathcal{A}_{,B}}{2\mathcal{A}^2}\right)\partial_\mu\Phi^A\partial_\nu\Phi^B - \frac{1}{2}\frac{\mathcal{A}_{,AB}}{\mathcal{A}}g_{\mu\nu}g^{\rho\sigma}\partial_\rho\Phi^A\partial_\sigma\Phi^B - \kappa^2\frac{\mathcal{U}}{\mathcal{A}}g_{\mu\nu} \end{aligned} \tag{2.109}$$

in terms of invariants. Hence, the same holds for the corresponding right hand side

$$\frac{\kappa^2}{\mathcal{A}}\left(T_{\mu\nu} - \frac{1}{2}g_{\mu\nu}g^{\rho\sigma}T_{\rho\sigma}\right) = \kappa^2\left(\frac{T_{\mu\nu}}{\mathcal{A}} - \frac{1}{2}g^{\mathfrak{E}}_{\mu\nu}g^{\mathfrak{E}\,\rho\sigma}\frac{T_{\rho\sigma}}{\mathcal{A}}\right), \tag{2.110}$$

and thus also $T_{\mu\nu}/\mathcal{A}$, must be invariant. It is convenient to define

$$T^{\mathfrak{E}}_{\mu\nu} = \frac{T_{\mu\nu}}{\mathcal{A}}, \quad T^{\mathfrak{E}} = g^{\mathfrak{E}\,\mu\nu}T^{\mathfrak{E}}_{\mu\nu} = \frac{T}{\mathcal{A}^2}, \quad \bar{T}^{\mathfrak{E}}_{\mu\nu} = T^{\mathfrak{E}}_{\mu\nu} - \frac{1}{2}g^{\mathfrak{E}}_{\mu\nu}g^{\mathfrak{E}\,\rho\sigma}T^{\mathfrak{E}}_{\rho\sigma}, \tag{2.111}$$

so that the metric field equation finally reads

$$R^{\mathfrak{E}}_{\mu\nu} - 2\mathfrak{G}^{\mathfrak{E}}_{AB}\partial_\mu\Phi^A\partial_\nu\Phi^B - \kappa^2 g^{\mathfrak{E}}_{\mu\nu}\mathcal{I}_2 = \kappa^2\bar{T}^{\mathfrak{E}}_{\mu\nu}. \tag{2.112}$$

Scalar field equation: We consider the metrics $g^{\mathfrak{E}}_{\mu\nu}$ on M and $\mathfrak{G}^{\mathfrak{E}}_{AB} = \mathcal{F}_{AB}$ on Q, together with their Levi-Civita connections. From the latter we construct

$$D^{\mathfrak{E}}_\mu D^{\mathfrak{E}}_\nu\Phi^A = \partial_\mu\partial_\nu\Phi^A - \Gamma^{\mathfrak{E}\,\rho}{}_{\nu\mu}\partial_\rho\Phi^A + \Gamma^{\mathfrak{E}\,A}{}_{CB}\partial_\mu\Phi^B\partial_\nu\Phi^C. \tag{2.113}$$

We can contract the tangent indices of M with $g^{\mathfrak{E}\,\mu\nu}$ and lower the tangent index of Q with $\mathfrak{G}^{\mathfrak{E}}_{AB}$, which then yields a section of Φ^*T^*Q. In an arbitrary frame, this can be written as

$$\begin{aligned} g^{\mathfrak{E}\,\mu\nu}\mathfrak{G}^{\mathfrak{E}}_{AB}D^{\mathfrak{E}}_\mu D^{\mathfrak{E}}_\nu\Phi^B &= g^{\mathfrak{E}\,\mu\nu}\mathfrak{G}^{\mathfrak{E}}_{AB}\left(\partial_\mu\partial_\nu\Phi^B - \Gamma^{\mathfrak{E}\,\rho}{}_{\nu\mu}\partial_\rho\Phi^B + \Gamma^{\mathfrak{E}\,B}{}_{DC}\partial_\mu\Phi^C\partial_\nu\Phi^D\right) \\ &= \frac{1}{\mathcal{A}}g^{\mu\nu}\mathcal{F}_{AB}\Big\{ - \left[\Gamma^\rho{}_{\nu\mu} + \frac{\mathcal{A}_{,C}}{2\mathcal{A}}\left(\delta^\rho_\mu\partial_\nu\Phi^C + \delta^\rho_\nu\partial_\mu\Phi^C - g^{\rho\sigma}g_{\mu\nu}\partial_\sigma\Phi^C\right)\right]\partial_\rho\Phi^B \\ &\quad + \partial_\mu\partial_\nu\Phi^B + \frac{1}{2}\mathcal{F}^{BE}\left(\mathcal{F}_{ED,C} + \mathcal{F}_{CE,D} - \mathcal{F}_{CD,E}\right)\partial_\mu\Phi^C\partial_\nu\Phi^D\Big\} \\ &= \frac{\mathcal{F}_{AB}}{\mathcal{A}}\Box\Phi^B + \frac{1}{2\mathcal{A}}\left(\mathcal{F}_{AC,B} + \mathcal{F}_{BA,C} - \mathcal{F}_{BC,A} + 2\mathcal{F}_{AB}\frac{\mathcal{A}_{,C}}{\mathcal{A}}\right)g^{\mu\nu}\partial_\mu\Phi^B\partial_\nu\Phi^C \\ &= \frac{1}{\mathcal{A}^2}\left\{\mathcal{A}\mathcal{F}_{AB}\Box\Phi^B + \left[(\mathcal{A}\mathcal{F}_{AB})_{,C} - \frac{1}{2}\mathcal{A}\mathcal{F}_{BC,A}\right]g^{\mu\nu}\partial_\mu\Phi^B\partial_\nu\Phi^C\right\}. \end{aligned} \tag{2.114}$$

Note that this exactly represents the first two terms on the left hand side of the scalar equation (2.78) divided by $\mathcal{A}$. It is entirely constructed from invariants, thus also the rest of the equation, when divided by $\mathcal{A}$, can be written in terms of invariants.

To express the terms containing the potential and its derivative, we consider the invariant one-form

$$d\mathcal{I}_2 = \frac{\mathcal{U}_{,A}\mathcal{A} - 2\mathcal{U}\mathcal{A}_{,A}}{\mathcal{A}^3}dX^A, \tag{2.115}$$

which also induces a section of Φ^*T^*Q via Φ. Then the combination

$$g^{\mathfrak{E}\,\mu\nu}\mathfrak{G}^{\mathfrak{E}}_{AB}D^{\mathfrak{E}}_\mu D^{\mathfrak{E}}_\nu\Phi^B - \frac{\kappa^2}{2}\mathfrak{d}_A\mathcal{I}_2 \tag{2.116}$$

essentially reproduces the left hand side of the scalar field equations in terms of invariant geometric quantities. Further, we have

$$d\mathcal{I}_1 = \frac{\mathcal{A}_{,A} - 2\mathcal{A}\alpha_{,A}}{\mathcal{A}^2} e^{2\alpha} dX^A \,, \tag{2.117}$$

so that the right hand side of the field equations reads

$$\frac{1}{4}\frac{\kappa^2 \mathcal{T}_A}{\mathcal{A}^3} = \frac{1}{4}\kappa^2 \frac{\mathcal{A}_{,A} - 2\mathcal{A}\alpha_{,A}}{\mathcal{A}} \frac{T}{\mathcal{A}^2} = -\frac{1}{4}\kappa^2 \frac{\mathcal{I}_{1,A}}{\mathcal{I}_1} T^{\mathfrak{E}} = -\frac{1}{4}\kappa^2 (\ln \mathcal{I}_1)_{,A} T^{\mathfrak{E}} \,, \tag{2.118}$$

and is hence also invariant.

Finally, the scalar field equation can be written as

$$g^{\mathfrak{E}\,\mu\nu} \mathfrak{G}^{\mathfrak{E}}_{AB} D^{\mathfrak{E}}_{\mu} D^{\mathfrak{E}}_{\nu} \Phi^B - \frac{\kappa^2}{2} \mathcal{I}_{2,A} = -\frac{1}{4}\kappa^2 (\ln \mathcal{I}_1)_{,A} T^{\mathfrak{E}} \,. \tag{2.119}$$

2.2.3.6 PPN formalism in terms of geometry and invariants

For the PPN formalism we choose a fixed set of coordinates (x^μ) on M and demand that there exists some $\Phi_0 \in Q$ such that

$$\begin{array}{rl} \mathcal{O}\left(g^0\right)^{\mathfrak{J}} : & M \to T^0_2 M \\ & x \mapsto \eta_{\mu\nu} dx^\mu \otimes dx^\nu \end{array} , \qquad \begin{array}{rl} \mathcal{O}\left(\Phi^0\right) : & M \to Q \\ & x \mapsto \Phi_0 \end{array} \tag{2.120}$$

is a vacuum solution of the field equations. We then perform the usual PPN perturbation ansatz

$$g^{\mathfrak{J}}_{00} = -1 + \mathcal{O}\left(h^2\right)^{\mathfrak{J}}_{00} + \mathcal{O}\left(h^4\right)^{\mathfrak{J}}_{00} + \mathcal{O}(6) \,, \tag{2.121a}$$

$$g^{\mathfrak{J}}_{0i} = \mathcal{O}\left(h^3\right)^{\mathfrak{J}}_{0i} + \mathcal{O}(5) \,, \tag{2.121b}$$

$$g^{\mathfrak{J}}_{ij} = \delta_{ij} + \mathcal{O}\left(h^2\right)^{\mathfrak{J}}_{ij} + \mathcal{O}(4) \,, \tag{2.121c}$$

$$\Phi^A = \Phi^A_0 + \mathcal{O}\left(\phi^2\right)^A + \mathcal{O}\left(\phi^4\right)^A + \mathcal{O}(6) \,. \tag{2.121d}$$

A similar expansion of $g^{\mathfrak{E}}_{\mu\nu}$ can be defined as

$$\begin{gathered} I_1 g^{\mathfrak{E}}_{00} = -1 + \mathcal{O}\left(h^2\right)^{\mathfrak{E}}_{00} + \mathcal{O}\left(h^4\right)^{\mathfrak{E}}_{00} + \mathcal{O}(6) \,, \quad I_1 g^{\mathfrak{E}}_{0i} = \mathcal{O}\left(h^3\right)^{\mathfrak{E}}_{0i} + \mathcal{O}(5) \,, \\ I_1 g^{\mathfrak{E}}_{ij} = \delta_{ij} + \mathcal{O}\left(h^2\right)^{\mathfrak{E}}_{ij} + \mathcal{O}(4) \,. \end{gathered} \tag{2.122}$$

One easily checks the relations

$$\mathcal{O}\left(h^2\right)^{\mathfrak{E}}_{00} = \mathcal{O}\left(h^2\right)^{\mathfrak{J}}_{00} + \frac{I_{1,A}}{I_1} \mathcal{O}\left(\phi^2\right)^A \,, \tag{2.123a}$$

$$\mathcal{O}\left(h^2\right)^{\mathfrak{E}}_{ij} = \mathcal{O}\left(h^2\right)^{\mathfrak{J}}_{ij} - \frac{I_{1,A}}{I_1} \mathcal{O}\left(\phi^2\right)^A \delta_{ij} \,, \tag{2.123b}$$

$$\mathcal{O}\left(h^3\right)^{\mathfrak{E}}_{0i} = \mathcal{O}\left(h^3\right)^{\mathfrak{J}}_{0i} \,, \tag{2.123c}$$

$$\begin{aligned} \mathcal{O}\left(h^4\right)^{\mathfrak{E}}_{00} = {} & \mathcal{O}\left(h^4\right)^{\mathfrak{J}}_{00} + \frac{I_{1,A}}{I_1} \mathcal{O}\left(\phi^4\right)^A + \frac{I_1 I_{1,AB} - 2 I_{1,A} I_{1,B}}{2 I_1^2} \mathcal{O}\left(\phi^2\right)^A \mathcal{O}\left(\phi^2\right)^B \\ & - \frac{I_{1,A}}{I_1} \mathcal{O}\left(\phi^2\right)^A \mathcal{O}\left(h^2\right)^{\mathfrak{J}}_{00} \,. \end{aligned} \tag{2.123d}$$

Conversely, one finds

$$\mathcal{O}\left(h^2\right)^{\mathfrak{J}}_{00} = \mathcal{O}\left(h^2\right)^{\mathfrak{E}}_{00} - \frac{I_{1,A}}{I_1}\mathcal{O}\left(\phi^2\right)^A , \tag{2.124a}$$

$$\mathcal{O}\left(h^2\right)^{\mathfrak{J}}_{ij} = \mathcal{O}\left(h^2\right)^{\mathfrak{E}}_{ij} + \frac{I_{1,A}}{I_1}\mathcal{O}\left(\phi^2\right)^A \delta_{ij} , \tag{2.124b}$$

$$\mathcal{O}\left(h^3\right)^{\mathfrak{J}}_{0i} = \mathcal{O}\left(h^3\right)^{\mathfrak{E}}_{0i} , \tag{2.124c}$$

$$\mathcal{O}\left(h^4\right)^{\mathfrak{J}}_{00} = \mathcal{O}\left(h^4\right)^{\mathfrak{E}}_{00} - \frac{I_{1,A}}{I_1}\mathcal{O}\left(\phi^4\right)^A - \frac{I_{1,AB}}{2I_1}\mathcal{O}\left(\phi^2\right)^A\mathcal{O}\left(\phi^2\right)^B + \frac{I_{1,A}}{I_1}\mathcal{O}\left(\phi^2\right)^A\mathcal{O}\left(h^2\right)^{\mathfrak{E}}_{00} . \tag{2.124d}$$

For the energy-momentum tensor we use the standard perfect fluid form

$$T^{\mathfrak{J}\,00} = \rho\left(1 + \mathcal{O}\left(h^2\right)^{\mathfrak{J}}_{00} + v^2 + \Pi\right) + \mathcal{O}(6) , \tag{2.125a}$$

$$T^{\mathfrak{J}\,0i} = \rho v^i + \mathcal{O}(5) , \tag{2.125b}$$

$$T^{\mathfrak{J}\,ij} = \rho v^i v^j + p\delta^{ij} + \mathcal{O}(6) . \tag{2.125c}$$

Lowering the indices with the corresponding metric $g^{\mathfrak{J}}_{\mu\nu}$ yields

$$T^{\mathfrak{J}}_{00} = \rho\left(1 - \mathcal{O}\left(h^2\right)^{\mathfrak{J}}_{00} + v^2 + \Pi\right) + \mathcal{O}(6) , \tag{2.126a}$$

$$T^{\mathfrak{J}}_{0i} = -\rho v_i + \mathcal{O}(5) , \tag{2.126b}$$

$$T^{\mathfrak{J}}_{ij} = \rho v_i v_j + p\delta_{ij} + \mathcal{O}(6) . \tag{2.126c}$$

The trace is given by

$$T^{\mathfrak{J}} = -\rho - \rho\Pi + 3p + \mathcal{O}(5) . \tag{2.127}$$

After trace-reversal we thus find

$$\bar{T}^{\mathfrak{J}}_{00} = \rho\left(\frac{1}{2} - \frac{\mathcal{O}\left(h^2\right)^{\mathfrak{J}}_{00}}{2} + v^2 + \frac{\Pi}{2} + \frac{3p}{2\rho}\right) + \mathcal{O}(6) , \tag{2.128a}$$

$$\bar{T}^{\mathfrak{J}}_{0i} = -\rho v_i + \mathcal{O}(5) , \tag{2.128b}$$

$$\bar{T}^{\mathfrak{J}}_{ij} = \rho\left[v_i v_j + \frac{\mathcal{O}\left(h^2\right)^{\mathfrak{J}}_{ij}}{2} + \left(\frac{1}{2} + \frac{\Pi}{2} - \frac{p}{2\rho}\right)\delta_{ij}\right] + \mathcal{O}(6) . \tag{2.128c}$$

For the related invariant energy-momentum tensor $T^{\mathfrak{E}}_{\mu\nu} = \mathcal{I}_1 T^{\mathfrak{J}}_{\mu\nu}$ we then have

$$T^{\mathfrak{E}}_{00} = I_1\rho\left(1 + \frac{2I_{1,A}}{I_1}\mathcal{O}\left(\phi^2\right)^A - \mathcal{O}\left(h^2\right)^{\mathfrak{E}}_{00} + v^2 + \Pi\right) + \mathcal{O}(6) , \tag{2.129a}$$

$$T^{\mathfrak{E}}_{0i} = -I_1\rho v_i + \mathcal{O}(5) , \tag{2.129b}$$

$$T^{\mathfrak{E}}_{ij} = I_1(\rho v_i v_j + p\delta_{ij}) + \mathcal{O}(6) . \tag{2.129c}$$

And the trace is given by

$$T^{\mathfrak{E}} = I_1^2\left(-\rho + 3p - \rho\,\Pi - 2\frac{I_{1,A}}{I_1}\rho\,\mathcal{O}\left(\phi^2\right)^A\right) . \tag{2.130}$$

Similarly, the trace-reversed energy-momentum tensors are given by

$$\bar{T}^{\mathfrak{E}}_{00} = I_1\rho \left(\frac{1}{2} + \frac{I_{1,A}}{I_1} \mathcal{O}\left(\phi^2\right)^A - \frac{\mathcal{O}\left(h^2\right)^{\mathfrak{E}}_{00}}{2} + v^2 + \frac{\Pi}{2} + \frac{3p}{2\rho} \right) + \mathcal{O}(6)\,, \tag{2.131a}$$

$$\bar{T}^{\mathfrak{E}}_{0i} = -I_1\rho v_i + \mathcal{O}(5)\,, \tag{2.131b}$$

$$\bar{T}^{\mathfrak{E}}_{ij} = I_1\rho \left[v_i v_j + \frac{\mathcal{O}\left(h^2\right)^{\mathfrak{E}}_{ij}}{2} + \left(\frac{1}{2} + \frac{I_{1,A}}{I_1} \mathcal{O}\left(\phi^2\right)^A + \frac{\Pi}{2} - \frac{p}{2\rho} \right) \delta_{ij} \right] + \mathcal{O}(6)\,, \tag{2.131c}$$

with trace

$$\bar{T}^{\mathfrak{E}} = -T^{\mathfrak{E}} = I_1^2 \left(\rho - 3p + \rho\,\Pi + 2\frac{I_{1,A}}{I_1} \rho\, \mathcal{O}\left(\phi^2\right)^A \right)\,. \tag{2.132}$$

Chapter 3

Probing relativistic effects

In this section, we discuss relativistic effects and the prospects of measuring them in terrestrial and planetary satellite missions.

For a given metric we can calculate the corresponding Hamiltonian. Satellite orbits are geodesics of the metric which can be calculated by solving Hamilton's equations. The motion of satellites in the Solar System is mostly determined by Newtonian motion with, general relativity only providing very small perturbations. This will allow us to expand the Hamiltonian in terms of velocity orders. The leading order terms then lead to Keplerian orbits plus a time dilation effect accounting for the variation of time along the orbit. The higher order terms then lead to different relativistic effects.

In Sec. 3.1, we develop the necessary tools in order to write a code for investigating these relativistic effects. Sec. 3.2 contains a publication using these tools to investigate relativistic effects with terrestrial and planetary satellite missions.

3.1 Framework for investigating relativistic effects

If not stated otherwise, we work in gravitational units, i.e., $c = 1$ and $GM = 1$.

3.1.1 Hamiltonian theory

In general relativity, the geodesics are derived from the Lagrangian

$$L = \frac{1}{2} g_{\mu\nu} \frac{dx^\mu}{d\lambda} \frac{dx^\nu}{d\lambda} \,, \tag{3.1}$$

where λ is an affine parameter. By doing a Legendre transformation we obtain the corresponding Hamiltonian H, which is numerically the same as the Lagrangian $H = L$. Using the relativistic 4-momentum $p_\mu = \frac{dx_\mu}{d\lambda}$ it is

$$H = \frac{1}{2} g^{\mu\nu} p_\mu p_\nu \,. \tag{3.2}$$

The equations of motion are then obtained from Hamilton's equations

$$\frac{dp_\mu}{d\lambda} = -\frac{\partial H}{\partial x^\mu} \,, \qquad \frac{dx^\mu}{d\lambda} = +\frac{\partial H}{\partial p_\mu} \,. \tag{3.3}$$

Along a geodesic, the Hamiltonian H is constant, i.e., $dH/dt = 0$. In a static spacetime, H does not depend on t explicitly, resulting in p_0 being constant. Then, either H or p_0 can be chosen freely, which fixes the parametrization and the other value. For example, if we choose the proper time as the affine parameter $\lambda = \tau$ ($ds^2 = -d\tau^2$ in $c = 1$ units), the Hamiltonian is $H = \frac{1}{2}\frac{ds^2}{d\tau^2} = -\frac{1}{2}$.

From $d\tau^2 = -ds^2 = -g^{\mu\nu}dx_\mu dx_\nu = -2H d\lambda^2$ it follows that $d\tau = \sqrt{-2H}d\lambda$ s.t.

$$\sqrt{-2H} = \frac{d\tau}{d\lambda} = \frac{d\tau}{dt}\frac{dt}{d\lambda} = \frac{p^0}{u^0}\,. \tag{3.4}$$

Therefore, the 4-velocity $u^\mu = \frac{dx^\mu}{d\tau}$ and the 4-momentum $p_\mu = \frac{dx_\mu}{d\lambda}$ are related by

$$u^\mu = \frac{dx^\mu}{d\tau} = \frac{d\lambda}{d\tau}\frac{dx^\mu}{d\lambda} = \frac{1}{\sqrt{-2H}}p^\mu = \frac{u^0}{p^0}p^\mu\,, \tag{3.5a}$$

$$\rightarrow p_\mu = \sqrt{-2H}u_\mu = \frac{p^0}{u^0}u_\mu\,. \tag{3.5b}$$

With $\mu = 0$ it follow that $\frac{p_0}{u_0} = \frac{p^0}{u^0}$, s.t. we can write

$$\sqrt{-2H} = \frac{p^0}{u^0} = \frac{p_0}{u_0}\,, \tag{3.6a}$$

$$H = -\frac{1}{2}\left(\frac{p^0}{u^0}\right)^2 = -\frac{1}{2}\left(\frac{p_0}{u_0}\right)^2\,. \tag{3.6b}$$

The coordinate velocity $v^\mu = \frac{dx^\mu}{dt}$ is related to the momentum by

$$v^\mu = \frac{dx^\mu}{dt} = \frac{dx^\mu}{d\lambda}\frac{d\lambda}{dt} = \frac{p^\mu}{p^0}\,, \tag{3.7a}$$

$$\rightarrow p_\mu = p^0 v_\mu\,. \tag{3.7b}$$

and to the 4-velocity by

$$u^\mu = \frac{dx^\mu}{d\tau} = \frac{dt}{d\tau}\frac{dx^\mu}{dt} = u^0 v^\mu = \frac{1}{\sqrt{-g_{\alpha\beta}v^\alpha v^\beta}}v^\mu\,. \tag{3.8}$$

In the last step we used

$$u^0 = \frac{1}{\sqrt{-g_{\mu\nu}v^\mu v^\nu}}\,, \tag{3.9}$$

which follows from

$$-1 = g_{\mu\nu}u^\mu u^\nu = g_{\mu\nu}\frac{dx^\mu}{d\tau}\frac{dx^\nu}{d\tau} = g_{\mu\nu}\frac{dx^\mu}{dt}\frac{dx^\nu}{dt}\left(\frac{dt}{d\tau}\right)^2 = g_{\mu\nu}v^\mu v^\nu\left(u^0\right)^2\,. \tag{3.10}$$

The orbit of a satellite is obtained by integrating the Hamiltonian equations of motion. Typically, the initial conditions are determined by initial instantaneous Keplerian elements, from which the initial position and (coordinate) velocity can be obtained. Given the initial position $\boldsymbol{x}$ and velocity $\boldsymbol{v}$, thus $v^\mu = (1, \boldsymbol{v})$, we determine the metric $g_{\mu\nu}$ and the inverse metric $g^{\mu\nu}$ at this position. We are free to choose some value for p_0, typically $p_0 = -1$. Then, all required quantities can be calculated by

$$H = -\frac{1}{2}\left(\frac{p_0}{g_{0\nu}u^\nu}\right)^2\,, \qquad u^0 = \frac{1}{\sqrt{-g_{\mu\nu}v^\mu v^\nu}}\,, \tag{3.11a}$$

$$u^j = u^0 v^j\,, \qquad p_j = \sqrt{-2H}g_{j\nu}u^\nu\,. \tag{3.11b}$$

Alternatively, we can fix the value for H, typically $H = -\frac{1}{2}$, and the required formulas are

$$u^0 = \frac{1}{\sqrt{-g_{\mu\nu}v^\mu v^\nu}}\,, \qquad u^j = u^0 v^j\,, \qquad p_\mu = \sqrt{-2H}g_{\mu\nu}u^\nu\,. \tag{3.12}$$

3.1.2 Expansion of Hamiltonian

We expand the Hamiltonian in terms of ϵ, which indicates at which velocity order a term appears, i.e., $v \sim \frac{1}{r^{1/2}} \sim \epsilon$. While the Hamiltonian is the same for massless and massive particles, the expansion works differently. The reason is the following: For massive particles, the 0−component of the momentum has a different order as the the i−components: $p_0 \approx -1 \sim \epsilon^0 = 1$ and $p_i \sim v \sim \epsilon$. In contrast, for massless particles $p_\mu \sim \epsilon^0 = 1$, since massless particles move with the speed of light.

3.1.2.1 Kepler Hamiltonian

Kepler orbits correspond to the Hamiltonian.

$$H = -\frac{1}{r} + \frac{\boldsymbol{p}^2}{2}. \tag{3.13}$$

Compared to the relativistic Hamiltonians below, there is no p_t.

3.1.2.2 Schwarzschild Hamiltonian

We discuss the Schwarzschild Hamiltonian for two different coordinates: the ‘standard’ Schwarzschild coordinates and isotropic coordinates.

In **standard spherical Schwarzschild coordinates**, the metric is

$$g_{\mu\nu} = \operatorname{diag}\left[-\left(1-\frac{2}{r}\right), \left(1-\frac{2}{r}\right)^{-1}, r^2, r^2\sin^2\theta\right]. \tag{3.14}$$

Then, we introduce pseudo-Cartesian coordinates the usual way

$$x = r\sin\theta\cos\phi\,, \tag{3.15a}$$
$$y = r\sin\theta\sin\phi\,, \tag{3.15b}$$
$$z = r\cos\theta\,. \tag{3.15c}$$

In these coordinates, the non-zero components of the metric are

$$g_{tt} = -\left(1-\frac{2}{r}\right), \qquad g_{ij} = \delta_{ij} + \frac{2x^i x^j}{\left(1-\frac{2}{r}\right) r^3}, \tag{3.16}$$

and the Hamiltonian is

$$H = -\frac{1}{2}\left(1-\frac{2}{r}\right)^{-1} p_t^2 + \frac{\boldsymbol{p}^2}{2} - \frac{(\boldsymbol{x}\cdot\boldsymbol{p})^2}{r^3}. \tag{3.17}$$

Expanding for the massive case yields

$$H = -\frac{p_t^2}{2} + \left(-\frac{p_t^2}{r} + \frac{\boldsymbol{p}^2}{2}\right)\epsilon^2 + \left(-\frac{2p_t^2}{r^2} - \frac{(\boldsymbol{x}\cdot\boldsymbol{p})^2}{r^3}\right)\epsilon^4 - \frac{4p_t^2}{r^3}\epsilon^6 + \mathcal{O}\left(\epsilon^8\right), \tag{3.18}$$

and for the massless case it is

$$H = \left(-\frac{p_t^2}{2} + \frac{\boldsymbol{p}^2}{2}\right) + \left(-\frac{p_t^2}{r} - \frac{(\boldsymbol{x}\cdot\boldsymbol{p})^2}{r^3}\right)\epsilon^2 - \frac{2p_t^2}{r^2}\epsilon^4 + \mathcal{O}\left(\epsilon^6\right). \tag{3.19}$$

In **isotropic coordinates**, the Schwarzschild metric is

$$g_{\mu\nu} = \operatorname{diag}\left[-\frac{\left(1-\frac{2}{4r}\right)^2}{\left(1+\frac{2}{4r}\right)^2}, \left(1+\frac{2}{4r}\right)^4, \left(1+\frac{2}{4r}\right)^4, \left(1+\frac{2}{4r}\right)^4\right], \tag{3.20}$$

and the Hamiltonian is

$$H = -\frac{p_t^2}{2}\frac{\left(1+\frac{2}{4r}\right)^2}{\left(1-\frac{2}{4r}\right)^2} + \frac{\boldsymbol{p}^2}{2}\left(1+\frac{2}{4r}\right)^{-4}. \tag{3.21}$$

This Hamiltonian holds for both pseudo-Cartesian and spherical coordinates with $r = \sqrt{x^2+y^2+z^2}$ and $\boldsymbol{p}^2 = p_x^2 + p_y^2 + p_z^2 = p_r^2 + \frac{p_\theta^2}{r^2} + \frac{p_\phi^2}{r^2\sin^2\theta}$. The expandsion of the metric is

$$g_{tt} = -1 + \frac{2}{R}\epsilon^2 - \frac{2}{R^2}\epsilon^4 + \mathcal{O}\left(\epsilon^6\right), \qquad g_{jj} = 1 + \frac{2}{R}\epsilon^2 + \frac{3}{2R^2}\epsilon^4 + \mathcal{O}\left(\epsilon^6\right), \tag{3.22}$$

and all off-diagonal elements are zero. For the massive case, the expansion of the Hamiltonian is

$$H = -\frac{p_t^2}{2} + \left(-\frac{p_t^2}{r} + \frac{\boldsymbol{p}^2}{2}\right)\epsilon^2 + \left(-\frac{p_t^2}{r^2} - \frac{\boldsymbol{p}^2}{r}\right)\epsilon^4 + \mathcal{O}\left(\epsilon^6\right), \tag{3.23}$$

and for the massless case

$$H = \left(-\frac{p_t^2}{2} + \frac{\boldsymbol{p}^2}{2}\right) + \left(-\frac{p_t^2}{r} - \frac{\boldsymbol{p}^2}{r}\right)\epsilon^2 + \left(-\frac{p_t^2}{r^2} + \frac{5\boldsymbol{p}^2}{4r^2}\right)\epsilon^4 + \mathcal{O}\left(\epsilon^6\right). \tag{3.24}$$

The standard (sta) and isotropic (iso) coordinates are related by

$$r_{\text{sta}} = r_{\text{iso}}\left(1 + \frac{2}{4\,r_{\text{iso}}}\right)^2, \tag{3.25a}$$

$$x_{j\,\text{sta}} = x_{j\,\text{iso}}\left(1 + \frac{2}{4\,r_{\text{iso}}}\right)^2, \tag{3.25b}$$

and the inverse transformation (valid outside the Schwarzschild horizon) is

$$r_{\text{iso}} = r_{\text{sta}}\left(\frac{1}{2} - \frac{2}{4r_{\text{sta}}} + \frac{1}{2}\sqrt{1 - \frac{2}{r_{\text{sta}}}}\right), \tag{3.26a}$$

$$x_{j\,\text{iso}} = x_{j\,\text{sta}}\left(\frac{1}{2} - \frac{2}{4r_{\text{sta}}} + \frac{1}{2}\sqrt{1 - \frac{2}{r_{\text{sta}}}}\right). \tag{3.26b}$$

3.1.2.3 Kerr Hamiltonian

The Kerr metric is the vacuum solution of a rotating non-charged black hole. In spherical Boyer-Lindquist coordinates (t, r, θ, ϕ) it is given by

$$\begin{aligned} ds^2 = &-\left(1 - \frac{2r}{\rho^2}\right)dt^2 - \frac{4sr\sin^2\theta}{\rho^2}dt\,d\phi + \frac{\rho^2}{\Delta}dr^2 + \rho^2 d\theta^2 \\ &+ \frac{\sin^2\theta}{\rho^2}\left(\left(r^2 + s^2\right)^2 - s^2\Delta\sin^2\theta\right)d\phi^2, \end{aligned} \tag{3.27}$$

where $\Delta \equiv r^2 - 2r + s^2$, $\rho^2 \equiv r^2 + s^2\cos^2\theta$ and $s = J/M$ is the spin per unit mass.

For a black hole, $s < 1$. However, the Kerr metric can also be used to describe the spacetime of e.g., a rotating planet and, in such cases, the spin can take much higher values. For solar system planets, it is typically a few 100s to a few 1000s.

We will expand the metric and the Hamiltonian up to the first order that includes a spin-square term.

In **spherical Boyer-Lindquist coordinates**, the Kerr Hamiltonian is

$$H = -\frac{(r^2+s^2)^2 - s^2\Delta\sin^2\theta}{2\rho^2\Delta}p_t^2 + \frac{\Delta}{2\rho^2}p_r^2 + \frac{1}{2\rho^2}p_\theta^2 + \frac{\Delta - s^2\sin^2\theta}{2\rho^2\Delta\sin^2\theta}p_\phi^2 - \frac{2sr}{\rho^2\Delta}p_t p_\phi . \tag{3.28}$$

For a **massive particle** ($r \sim \frac{1}{\epsilon^2}, p_r \sim \epsilon, p_\theta \sim p_\phi \sim \frac{1}{\epsilon}$) like a satellite, the expansion up to the order that contains spin-square is

$$\begin{aligned} H = &-\frac{p_t^2}{2} + \left[-\frac{p_t^2}{r} + \frac{1}{2}\left(p_r^2 + \frac{p_\theta^2}{r^2} + \frac{p_\phi^2}{r^2\sin^2\theta}\right)\right]\epsilon^2 + \left[-\frac{2p_t^2}{r^2} - \frac{p_r^2}{r}\right]\epsilon^4 \\ &- s\frac{2p_t p_\phi}{r^3}\epsilon^5 + \left[-\frac{4p_t^2}{r^3} + s^2\left(\frac{\cos^2\theta\, p_t^2}{r^3} + \frac{\sin^2\theta\, p_r^2}{2r^2} - \frac{\cos^2\theta\, p_\theta^2}{2r^4} - \frac{p_\phi^2}{2r^4\sin^2\theta}\right)\right]\epsilon^6 , \end{aligned} \tag{3.29}$$

and the **expansion for massless particles (photons)** ($r \sim \frac{1}{\epsilon^2}, p_r \sim 1, p_\theta \sim p_\phi \sim \frac{1}{\epsilon^2}$) is

$$\begin{aligned} H = &\left[-\frac{p_t^2}{2} + \frac{1}{2}\left(p_r^2 + \frac{p_\theta^2}{r^2} + \frac{p_\phi^2}{r^2\sin^2\theta}\right)\right] + \left[-\frac{p_t^2}{r} - \frac{p_r^2}{r}\right]\epsilon^2 \\ &+ \left[-\frac{2p_t^2}{r^2} - s\frac{2p_t p_\phi}{r^3} + s^2\left(\frac{\sin^2\theta\, p_r^2}{2r^2} - \frac{\cos^2\theta\, p_\theta^2}{2r^4} - \frac{p_\phi^2}{2r^4\sin^2\theta}\right)\right]\epsilon^4 . \end{aligned} \tag{3.30}$$

It is worth noting that for photons, the lowest order where the spin parameter appears is $\mathcal{O}\left(\epsilon^4\right)$. At this order, there are two terms containing s and s^2, respectively, while for massive particles the spin-square effects are much smaller compared to the spin effects, they are comparable for photons.

When introducing **pseudo-Cartesian coordinates** (3.15), the expanded metric has the components

$$g_{tt} = -1 + \frac{2}{r}\epsilon^2 - s^2\frac{2z^2}{r^5}\epsilon^6 , \tag{3.31a}$$

$$g_{xx} = 1 + \frac{2x^2}{r^3}\epsilon^2 + \left(\frac{4x^2}{r^4} + \frac{s^2}{r^2}\left(1 - \frac{2x^2}{r^2}\right)\right)\epsilon^4 , \qquad g_{tx} = s\frac{2y}{r^3}\epsilon^4 , \tag{3.31b}$$

$$g_{yy} = 1 + \frac{2y^2}{r^3}\epsilon^2 + \left(\frac{4y^2}{r^4} + \frac{s^2}{r^2}\left(1 - \frac{2y^2}{r^2}\right)\right)\epsilon^4 , \qquad g_{ty} = -s\frac{2x}{r^3}\epsilon^4 , \tag{3.31c}$$

$$g_{zz} = 1 + \frac{2z^2}{r^3}\epsilon^2 + \frac{4z^2}{r^4}\epsilon^4 , \qquad g_{tz} = 0 , \tag{3.31d}$$

$$g_{xy} = \frac{2xy}{r^3}\epsilon^2 + \left(\frac{4xy}{r^4} - s^2\frac{2xy}{r^4}\right)\epsilon^4 , \qquad g_{xz} = \frac{2xz}{r^3}\epsilon^2 + \left(\frac{4xz}{r^4} - s^2\frac{xz}{r^4}\right)\epsilon^4 , \tag{3.31e}$$

$$g_{yz} = \frac{2yz}{r^3}\epsilon^2 + \left(\frac{4yz}{r^4} - s^2\frac{yz}{r^4}\right)\epsilon^4 . \tag{3.31f}$$

These coordinates are clearly not isotropic. The expansion for the **massive case** is

$$\begin{aligned}H = &-\frac{p_t^2}{2} + \left[-\frac{p_t^2}{r} + \frac{\boldsymbol{p}^2}{2}\right]\epsilon^2 + \left[-\frac{2p_t^2}{r^2} - \frac{(\boldsymbol{x}\cdot\boldsymbol{p})^2}{r^3}\right]\epsilon^4 - s\frac{2(xp_y - yp_x)p_t}{r^3}\epsilon^5 \\ &+ \left[-\frac{4p_t^2}{r^3} + s^2\left[\frac{z^2p_t^2}{r^5} + \frac{1}{2r^4}\left(1-\frac{z^2}{r^2}\right)\left((\boldsymbol{x}\cdot\boldsymbol{p})^2 - \left(zp_z - \frac{z^2}{r^2}\frac{xp_x+yp_y}{1-\frac{z^2}{r^2}}\right)^2 - \frac{(xp_y-yp_x)^2}{\left(1-\frac{z^2}{r^2}\right)^2}\right)\right]\right]\epsilon^6 \\ &+ \mathcal{O}\left(\epsilon^8\right) ,\end{aligned} \tag{3.32}$$

and for the **massless case** it is

$$\begin{aligned}H = &\left(-\frac{p_t^2}{2} + \frac{\boldsymbol{p}^2}{2}\right) + \left(-\frac{p_t^2}{r} - \frac{(\boldsymbol{x}\cdot\boldsymbol{p})^2}{r^3}\right)\epsilon^2 + \left[-\frac{2p_t^2}{r^2} - s\frac{2(xp_y-yp_x)p_t}{r^3}\right. \\ &\left.+ s^2\frac{1}{2r^4}\left(1-\frac{z^2}{r^2}\right)\left((\boldsymbol{x}\cdot\boldsymbol{p})^2 - \left(zp_z - \frac{z^2}{r^2}\frac{xp_x+yp_y}{1-\frac{z^2}{r^2}}\right)^2 - \frac{(xp_y-yp_x)^2}{\left(1-\frac{z^2}{r^2}\right)^2}\right)\right]\epsilon^4 \\ &+ \mathcal{O}\left(\epsilon^6\right) .\end{aligned} \tag{3.33}$$

3.1.2.4 PPN Hamiltonian

For investigating relativistic effects it can be advantageous to consider the parametrized post-Newtonian (PPN) metric instead of the Kerr metric since it allows to consider an arbitrary mass distribution instead of a black hole. The components of the metric are [11]

$$\begin{aligned} g_{tt} &= -1 + 2U\epsilon - 2\beta U^2\epsilon^4 , \\ g_{ij} &= (1 + 2\gamma U\epsilon^2)\delta_{ij} , \\ g_{0i} &= -(1+\gamma)\frac{1}{r^3}(\boldsymbol{s}\times\boldsymbol{x})^i\epsilon^4 . \end{aligned} \tag{3.34}$$

U is the Newtonian gravitational potential and $\boldsymbol{s}$ is the spin vector of the rotating central object. γ and β are the PPN parameters. In general relativity both are unity, while alternative theories predict them to take different values or even be functions depending on the position as we have seen for scalar-tensor theories in Sec. 2. There is a much more general form of the PPN metric with additional parameters but for our purpose the metric above is sufficient.

We see that with this metric we can describe the orbits of massive particles up to order $\mathcal{O}\left(\epsilon^5\right)$. Spin-square effects appear at one order higher, which would require the knowledge of g_{tt} to $\mathcal{O}\left(\epsilon^6\right)$ and g_{ij} to $\mathcal{O}\left(\epsilon^4\right)$. For photons, this metric can describe their trajectories up to $\mathcal{O}\left(\epsilon^2\right)$, which yields the Shapiro light deflection. Spin effects can not be described since this would require g_{ij} up to $\mathcal{O}\left(\epsilon^4\right)$.

The corresponding Hamiltonian for non-relativistic orbits is

$$\begin{aligned} H = &-\frac{p_t^2}{2} + \left(-Up_t^2 + \frac{\boldsymbol{p}^2}{2}\right)\epsilon^2 + \left(-(2-\beta)U^2p_t^2 - \gamma U\boldsymbol{p}^2\right)\epsilon^4 \\ &- (1+\gamma)\frac{(\boldsymbol{p}(\boldsymbol{s}\times\boldsymbol{x}))\,p_t}{r^3}\epsilon^5 + \mathcal{O}\left(\epsilon^6\right) , \end{aligned} \tag{3.35}$$

and for photons

$$H = \left(-\frac{p_t^2}{2} + \frac{\boldsymbol{p}^2}{2}\right) + \left(-Up_t^2 - \gamma U\boldsymbol{p}^2\right)\epsilon^2 + \mathcal{O}\left(\epsilon^2\right) . \tag{3.36}$$

If we consider a point source $U = 1/r$, GR $\gamma = \beta = 1$, and a spin vector pointing along the z-axis ($s \equiv s_z$), the PPN Hamiltonian becomes (massive)

$$H = -\frac{p_t^2}{2} + \left(-\frac{p_t^2}{r} + \frac{\boldsymbol{p}^2}{2}\right)\epsilon^2 + \left(-\frac{p_t^2}{r^2} - \frac{\boldsymbol{p}^2}{r}\right)\epsilon^4 - 2s\frac{(xp_y - yp_x)\,p_t}{r^3}\epsilon^5 + \mathcal{O}\left(\epsilon^6\right) , \tag{3.37}$$

and (massless)

$$H = \left(-\frac{p_t^2}{2} + \frac{\boldsymbol{p}^2}{2}\right) + \left(-\frac{p_t^2}{r} - \frac{\boldsymbol{p}^2}{r}\right)\epsilon^2 + \mathcal{O}\left(\epsilon^4\right) . \tag{3.38}$$

These expressions are equivalent to the Kerr Hamiltonians (3.32) and (3.33) if we drop the terms $\mathcal{O}\left(\epsilon^6\right)$ in the massive and $\mathcal{O}\left(\epsilon^4\right)$ in the massless case, respectively. Note that the PPN metric is written in isotropic coordinates, while the Kerr metric is written in non-isotropic Boyer-Lindquist coordinates (similar to standard Schwarzschild coordinates). The two metrics can be transformed into each other by using the transformations (3.25) and (3.26). However, note that with these coordinate transformations the Kerr metric in Boyer-Lindquist coordinates can only be ‘isotropisized’ up to the order discussed here. When going to higher orders it does not work anymore.

3.1.3 Relativistic effects

The expansion of the Hamiltonian allows the discussion of different relativistic effects on non-relativistic orbits and photon trajectories.

3.1.3.1 Effects on orbit

For this case, we consider the expanded Hamiltonian (3.35) with the GR values for γ and β

$$H = -\frac{p_t^2}{2} + \left(-Up_t^2 + \frac{\boldsymbol{p}^2}{2}\right)\epsilon^2 + \left(-U^2p_t^2 - U\boldsymbol{p}^2\right)\epsilon^4 - 2\frac{(\boldsymbol{p}(\boldsymbol{s}\times\boldsymbol{x}))\,p_t}{r^3}\epsilon^5 + \mathcal{O}\left(\epsilon^6\right) . \tag{3.39}$$

The different relativistic effects will arise due to the terms in the Hamiltonian at different orders. For the relativistic effects we consider the point source contribution $U = 1/r$ only. We will discuss the effect of the multipole moments below.

Below, we discuss the effect of the multipole moments, but non-relativistically below.

The equations of motion corresponding to the purely Newtonian Hamiltonian (3.13) are

$$\frac{dp_i}{d\lambda} = -\frac{\partial H}{\partial x^i} = -\frac{x^i}{r^3} , \tag{3.40a}$$

$$\frac{dx^i}{d\lambda} = \frac{\partial H}{\partial p_i} = p_i \, . \tag{3.40b}$$

These equations of motion yield a perfect **Keplerian ellipse**.

A **time dilation** effect is obtained when considering the Hamiltonian (3.39) up to second order in ϵ, i.e.,

$$H_{\text{TD}} = -\frac{p_t^2}{2} + \left(-\frac{p_t^2}{r} + \frac{\boldsymbol{p}^2}{2}\right)\epsilon^2, \tag{3.41}$$

which has the equations of motion

$$\frac{dp_t}{d\lambda} = -\frac{\partial H_{\text{TD}}}{\partial t} = 0\,, \qquad \frac{dp_i}{d\lambda} = -\frac{\partial H_{\text{TD}}}{\partial x^i} = -\frac{x^i p_t^2}{r^3}\epsilon^2\,, \tag{3.42a}$$

$$\frac{dt}{d\lambda} = \frac{\partial H_{\text{TD}}}{\partial p_t} = -p_t - \frac{2p_t}{r}\epsilon^2\,, \qquad \frac{dx^i}{d\lambda} = \frac{\partial H_{\text{TD}}}{\partial p_i} = p_i\epsilon^2\,. \tag{3.42b}$$

The first equation tells us that p_t is constant and we can choose it freely, typically $p_t = -1$. This gives us the same equations of motion for the spatial coordinates. Thus, the orbit is still a perfect Keplerian ellipse, but the flow of time varies depending on the position in the gravitational field as can be seen from the $dt/d\lambda$ equation. This is a special relativistic effect, arising from the metric $g_{tt} = -\left(1 - \frac{2}{r}\right), g_{ij} = \delta_{ij}$. Note that also the higher order effects lead to time dilation.

What we call **Schwarzschild curvature** is the effect that arises due to the terms of 4th order in ϵ. The terms of this order in the Hamiltonian (3.39)

$$\triangle H_{\text{SS}} = -\frac{p_t^2}{r^2} - \frac{\boldsymbol{p}^2}{r}\,, \tag{3.43}$$

modify the equations of motion by (of order ϵ^4)

$$\frac{d\triangle p_t}{d\lambda} = -\frac{\partial \triangle H_{\text{SS}}}{\partial t} = 0\,, \qquad \frac{d\triangle p_i}{d\lambda} = -\frac{\partial \triangle H_{\text{SS}}}{\partial x^i} = -\frac{x^i}{r}\left(\frac{2p_t^2}{r^3} + \frac{\boldsymbol{p}^2}{r^2}\right)\,, \tag{3.44a}$$

$$\frac{d\triangle t}{d\lambda} = \frac{\partial \triangle H_{\text{SS}}}{\partial p_t} = -\frac{2p_t}{r^2}\,, \qquad \frac{d\triangle x^i}{d\lambda} = \frac{\partial \triangle H_{\text{SS}}}{\partial p_i} = -\frac{2p_i}{r}\,. \tag{3.44b}$$

This Schwarzschild curvature effect leads to the famous precession of perihelion.

The 5th order term

$$\triangle H_{\text{Spin1}} = -2\frac{(\boldsymbol{p}(\boldsymbol{s} \times \boldsymbol{x}))\,p_t}{r^3} = -2\frac{(\boldsymbol{x}(\boldsymbol{p} \times \boldsymbol{s}))\,p_t}{r^3}\,, \tag{3.45}$$

leads to what we call the **first order spin** effect, which is a frame-dragging effect. The equations of motion are (of order ϵ^5)

$$\frac{d\triangle p_t}{d\lambda} = -\frac{\partial \triangle H_{\text{Spin1}}}{\partial t} = 0\,, \tag{3.46a}$$

$$\frac{d\triangle p_i}{d\lambda} = -\frac{\partial \triangle H_{\text{Spin1}}}{\partial x^i} = -\frac{2p_t}{r^5}\left(3(\boldsymbol{p} \times \boldsymbol{s})x^i - (\boldsymbol{p} \times \boldsymbol{s})^i\boldsymbol{x}\right) \cdot \boldsymbol{x}\,, \tag{3.46b}$$

$$\frac{d\triangle t}{d\lambda} = \frac{\partial \triangle H_{\text{Spin1}}}{\partial p_t} = -2\frac{\boldsymbol{x} \cdot (\boldsymbol{p} \times \boldsymbol{s})}{r^3}\,, \tag{3.46c}$$

$$\frac{d\triangle x^i}{d\lambda} = \frac{\partial \triangle H_{\text{Spin1}}}{\partial p_i} = -\frac{2(\boldsymbol{s} \times \boldsymbol{x})^i p_t}{r^3}\,. \tag{3.46d}$$

Taking **all relativistic effects** together gives the equations of motion

$$\frac{dp_t}{d\lambda} = 0\,, \tag{3.47a}$$

$$\frac{dp_i}{d\lambda} = -\frac{x^i p_t^2}{r^3}\epsilon^2 - \frac{x^i}{r}\left(\frac{2p_t^2}{r^3} + \frac{\boldsymbol{p}^2}{r^2}\right)\epsilon^4 - \frac{2p_t}{r^5}\left(3(\boldsymbol{p} \times \boldsymbol{s})x^i - (\boldsymbol{p} \times \boldsymbol{s})^i\boldsymbol{x}\right) \cdot \boldsymbol{x}\,\epsilon^5\,, \tag{3.47b}$$

$$\frac{dt}{d\lambda} = -p_t - \frac{2p_t}{r}\epsilon^2 - \frac{2p_t}{r^2}\epsilon^4 - 2\frac{\boldsymbol{x} \cdot (\boldsymbol{p} \times \boldsymbol{s})}{r^3}\epsilon^5\,, \tag{3.47c}$$

$$\frac{dx^i}{d\lambda} = p_i\epsilon^2 - \frac{2p_i}{r}\epsilon^4 - \frac{2(\boldsymbol{s} \times \boldsymbol{x})^i p_t}{r^3}\epsilon^5\,. \tag{3.47d}$$

In satellite missions, of course the **multipole moments** have to be considered as well. They account for the non-spherical mass distribution of the central mass and the presence of other masses, that can have a significant influence on the orbit at a Newtonian level. Thus, in order to be able to extract the tiny relativistic signals, these effects have to be well understood. Of course, the multipoles will also affect the relativistic effects, but since they are very small anyway, we neglect this and include multipoles in the Newtonian part of the Hamiltonian only. The Newtonian gravitational potential can be expressed as

$$U = \frac{GM}{r}\left(1 - \sum_{n=2}^{\infty} J_n \left(\frac{R}{r}\right)^n P_n(\cos\theta)\right), \tag{3.48}$$

where J_n are the multipole moments, θ is the polar angle in spherical coordinates and P_n are the Legendre polynomials

$$P_n(x) = \frac{1}{2^n}\sum_{k=0}^{n}\binom{n}{k}^2 (x-1)^{n-k}(x+1)^k, \tag{3.49}$$

the first few being

$$P_0(x) = 1\,, \qquad P_1(x) = x\,, \tag{3.50}$$

$$P_2(x) = \frac{1}{2}(3x^2-1)\,, \qquad P_3(x) = \frac{1}{2}(5x^3-3x)\,. \tag{3.51}$$

Note that the $n = 1$ contribution to the potential vanishes by conservation of momentum and because the coordinate center coincides with the center of mass. To express the Legendre polynomials in Cartesian coordinates use the relation $\frac{z}{r} = \cos\theta$.

3.1.3.2 Equatorial and polar orbits

In this section, we discuss two special types of orbits, equatorial and polar orbits. We consider a point source and coordinates s.t. the spin axis shows into the z-direction.

First, we consider an initially **equatorial orbit**, i.e., the orbit shall start in the xy-plane ($z_0 = p_{z0} = 0$). In a small time step $\triangle\lambda$, the z components of the coordinates and momentum will not change since

$$\triangle z = \left.\frac{d\triangle z}{d\lambda}\right|_0 \triangle\lambda = 0\,, \tag{3.52a}$$

$$\triangle p_z = \left.\frac{d\triangle p_z}{d\lambda}\right|_0 \triangle\lambda = 0\,, \tag{3.52b}$$

and thus, the orbit is in fact a true equatorial orbit. Here, time dilation ($\sim \epsilon^2$), Schwarzschild curvature ($\sim \epsilon^4$) and spin ($\sim \epsilon^5$) were included.

Later on, we will be interested in the difference in the redshift signal between the relativistic and non-relativistic orbit. For this reason, we look at what happens at pericenter: We choose the coordinates s.t. pericenter (or equivalently apocenter) is at $y = p_x = 0$. Thus, the only changes in coordinates and momentum are

$$\frac{dy}{d\lambda} = p_y\epsilon^2 - \frac{2p_y}{r}\epsilon^4 - s\frac{2xp_t}{r^3}\epsilon^5\,, \tag{3.53a}$$

$$\frac{dp_x}{d\lambda} = -\frac{xp_t^2}{r^3}\epsilon^2 - \frac{x}{r}\left(\frac{2p_t^2}{r^3} + \frac{p_y^2}{r^2}\right)\epsilon^4 - s\frac{4p_tp_y}{r^3}\epsilon^5\,, \tag{3.53b}$$

$$\frac{dt}{d\lambda} = -p_t - \frac{2p_t}{r}\epsilon^2 - \frac{2p_t}{r^2}\epsilon^4 - s\frac{2xp_y}{r^3}\epsilon^5\,. \tag{3.53c}$$

Second, we consider an initially **polar orbit**. We choose coordinates s.t. the orbit is initially in the yz-plane, i.e., $x_0 = p_{x0} = 0$. Now, the coordinate and the momentum will both gain a component in the x-direction (see Eq. (3.46))

$$\triangle x = \left.\frac{d\triangle x}{d\lambda}\right|_0 \triangle\lambda = s \left.\frac{2p_t y}{r^3}\right|_0 \triangle\lambda\,, \tag{3.54}$$

$$\triangle p_x = \left.\frac{d\triangle p_x}{d\lambda}\right|_0 \triangle\lambda = s \left.\frac{2p_t p_y}{r^3}\right|_0 \triangle\lambda\,, \tag{3.55}$$

that pushes the satellite out of the plane. If there was no spin, the orbit would stay in the plane. Assuming pericenter is at $z = 0$, then there $p_y = 0$. The non-vanishing equations of motion are

$$\frac{dx}{d\lambda} = s\frac{2yp_t}{r^3}\epsilon^5, \qquad \frac{dz}{d\lambda} = p_z\epsilon^2 - \frac{2p_z}{r}\epsilon^4, \tag{3.56a}$$

$$\frac{dp_y}{d\lambda} = -\frac{yp_t^2}{r^3}\epsilon^2 - \frac{y}{r}\left(\frac{2p_t^2}{r^3} + \frac{p_z^2}{r^2}\right)\epsilon^4, \qquad \frac{dt}{d\lambda} = -p_t - \frac{2p_t}{r}\epsilon^2 - \frac{2p_t}{r^2}\epsilon^4\,. \tag{3.56b}$$

If, on the other hand, the pericenter is at $y = 0$ ($p_z = 0$) the equations are

$$\frac{dy}{d\lambda} = p_y\epsilon^2 - \frac{2p_y}{r}\epsilon^4\,, \qquad \frac{dp_x}{d\lambda} = s\frac{2p_t p_y}{r^3}\epsilon^5\,, \tag{3.57a}$$

$$\frac{dp_z}{d\lambda} = -\frac{zp_t^2}{r^3}\epsilon^2 - \frac{z}{r}\left(\frac{2p_t^2}{r^3} + \frac{p_y^2}{r^2}\right)\epsilon^4\,, \qquad \frac{dt}{d\lambda} = -p_t - \frac{2p_t}{r}\epsilon^2 - \frac{2p_t}{r^2}\epsilon^4\,. \tag{3.57b}$$

3.1.4 Redshift measurement

The energy of a particle (null or timelike) moving with 4-momentum p_μ as measured by an observer having four-velocity $U^\mu = \frac{dx^\mu}{d\tau}$ is $E = -p_\mu U^\mu$. To avoid confusion, timelike momenta and velocities will be denoted by capital letters and those of null trajectories by lower case letters in this section.

The frequency ν of a photon is proportional to its energy. Therefore, the redshift is given by

$$z = \frac{\nu_{\mathrm{E}}}{\nu_{\mathrm{O}}} - 1 = \frac{p^{\mathrm{E}}_\mu U^\mu_{\mathrm{E}}}{p^{\mathrm{O}}_\nu U^\nu_{\mathrm{O}}} - 1, \tag{3.58}$$

where E and O refers to the emitter and the observer, respectively.

We perform the calculation in detail for the case of a moving emitter (satellite) at $\boldsymbol{r}_{\mathrm{E}}$ and a stationary observer (on Earth) at $\boldsymbol{r}_{\mathrm{O}}$. Therefore, $U^\mu_{\mathrm{O}} = (\sqrt{-1/g^{\mathrm{O}}_{tt}}, 0, 0, 0)$. At some instant of time, the emitter emits a photon with 4-momentum $p^{\mathrm{E}}_\mu = (p^{\mathrm{E}}_t, \boldsymbol{p}^{\mathrm{E}})$. In a curved spacetime, the photon will not travel on a straight line (in a 'Minkowskian' sense). Therefore, a shooting method is employed to find the right initial direction s.t. the photon eventually will arrive at the observer. However, since in a weak field the deflection will be very small, $\boldsymbol{p}_{\mathrm{E}} = (\boldsymbol{r}_{\mathrm{O}} - \boldsymbol{r}_{\mathrm{E}})/k$ (as in flat spacetime) is a good guess. Since $g^{\mu\nu}p^{\mathrm{E}}_\mu p^{\mathrm{E}}_\nu = 0$, the arbitrary constant k fixes the constant value of p^{E}_t, or vice versa. A typical choice is $k = |\boldsymbol{r}_{\mathrm{O}} - \boldsymbol{r}_{\mathrm{E}}|$ s.t. $p^{\mathrm{E}}_t \approx -1$.

The 4-velocity U^μ of the satellite is obtained from its 4-momentum P_μ (not to confuse with the signal 4-momentum!). Remember, both P_t and H remain constant. One of the two can be chosen freely which fixes the value of the other.

We determine the redshift for an observer that is infinitely far away from the satellite orbiting a planet. We consider relativistic effects on the orbit only and neglect effects on the signal photons. Since the observer is far away and at rest, its 4-velocity is $U^\mu_{\mathrm{O}} = (1, 0, 0, 0)$. The observer is located in the direction of the unit vector $\hat{n}_{\mathrm{Obs}}$. The emitter (satellite) has 4-velocity $U^\mu_{\mathrm{E}} = (U^t_{\mathrm{E}}, \boldsymbol{U})$ and the signal photon has 4-momentum $p_\mu = (p_t, \boldsymbol{p}) = (p_t, p\,\hat{n}_{\mathrm{Obs}}) = (-1, \hat{n}_{\mathrm{Obs}})$ at both the position of the emitter and the observer. Here, we make use of the fact that p_t can be chosen freely and $p^2 = \eta^{\mu\nu} p_\mu p_\nu = 0$ (no signal effects: $g_{\mu\nu} \to \eta_{\mu\nu}$). Therefore, the redshift is

$$\begin{aligned} z &= \frac{p^{\mathrm{E}}_\mu U^\mu_{\mathrm{E}}}{p^{\mathrm{O}}_\nu U^\nu_{\mathrm{O}}} - 1 = \frac{p_t U^t_{\mathrm{E}} + \boldsymbol{p}\boldsymbol{U}}{p_t} - 1 = U^t_{\mathrm{E}} - \hat{n}_{\mathrm{Obs}}\boldsymbol{U} - 1 \\ &= U^t_{\mathrm{E}} - U_{\mathrm{LOS}} - 1\,, \end{aligned} \tag{3.59}$$

where $U_{\mathrm{LOS}} = \hat{n}_{\mathrm{Obs}}\boldsymbol{U}$ is the velocity along the line of sight. Thus, the redshift consists of two parts: a time dilation part U^t_{E} and a velocity part $-U_{\mathrm{LOS}}$. The first accounts for the difference in time due to the different positions of the satellite and the observer in the gravitational field. The second is a Doppler shift that depends on the geometry. Typically, the velocity term will be the dominant one.

The size of a relativistic effect signal is given by the difference in the redshift signal Δz between the relativistic redshift signal z_{GR} (i.e., the relativistic term in the Hamiltonian turned on) and the non-relativistic reference signal z_{nonGR}:

$$\Delta z = z_{\mathrm{GR}} - z_{\mathrm{nonGR}} = \Delta U^t_{\mathrm{E}} - \Delta U_{\mathrm{LOS}} \approx \Delta\left(\frac{dt}{d\lambda}\right) - \Delta\left(\frac{d\boldsymbol{x}}{d\lambda}\right)\bigg|_{\mathrm{LOS}}\,. \tag{3.60}$$

Thus, in order to have a redshift signal, we need a relativistic contribution in the temporal equation of motion $\frac{dt}{d\lambda}$ and/or in the spatial equation $\frac{d\boldsymbol{x}}{d\lambda}$ along the line of sight.

Let us have a closer look at the Schwarzschild and the first order spin effect. The dominant contribution to the redshift signal z is the velocity component due to an effect along the line of sight. For Schwarzschild this is

$$\Delta z_{\mathrm{SS}} \approx \Delta U^{\mathrm{SS}}_{\mathrm{LOS}} = \frac{\partial \Delta H_{\mathrm{SS}}}{\partial \boldsymbol{p}} \cdot \hat{b} = -\frac{2\boldsymbol{p}}{r} \cdot \hat{b}\,, \tag{3.61}$$

and for spin it is

$$\Delta z_{\mathrm{spin}} \approx \Delta U^{\mathrm{spin}}_{\mathrm{LOS}} = \frac{\partial \Delta H_{\mathrm{spin}}}{\partial \boldsymbol{p}} \cdot \hat{b} = -\frac{2}{r^3}(\boldsymbol{s} \times \boldsymbol{r}) \cdot \hat{b} = -\frac{2}{r^2}\boldsymbol{s} \cdot (\hat{r} \times \hat{b})\,. \tag{3.62}$$

$\boldsymbol{r}$ is the satellite's position, $\hat{r}$ the corresponding unit vector, $\boldsymbol{s}$ is the spin vector and $\hat{b}$ is the unit vector pointing from the satellite towards the observer. Note that the redshift, apart from the spin, only depends on the positions of satellite and observer. It is independent of the satellite's velocity.

3.1.5 Orbit discussion

Relativistic effects peak at the pericenter of an orbit since there the velocity is the highest and the distance to the central object is minimal. In order to estimate the size of a relativistic effect, we determine Δz at pericenter for different extreme cases of orbit and observer configurations. We always assume that the distance to the observer is large compared to the orbit size. This is of course not appropriate for terrestrial satellite missions, where the observer is on the Earth's surface. Further, we choose the affine parametrization with $p_t = -1$ and choose the spin axis to be in z-direction.

Schwarzschild curvature only depends on the total mass of the central object and not the spin, and thus only the orientation of the orbit w.r.t. the observer matters. In a Schwarzschild metric, orbits are (not perfect) ellipses with precessing pericenter in a plane. For the spin effect, in contrast, the orientation of the orbit-observer system w.r.t. the spin axis matters, thus there are more cases to consider. Important for this case is that spin can cause the orbit to leave the initial Keplerian orbital plane.

First, we consider an **equatorial orbit**. We choose coordinates s.t. the orbit is in the xy-plane ($\theta = 90°$) with pericenter at $y = 0$. Then the contributions to the relativistic redshift signal (Schwarzschild at $\mathcal{O}(\epsilon^4)$, Spin at $\mathcal{O}(\epsilon^5)$) at pericenter are

$$\Delta\left(\frac{dt}{d\lambda}\right) = \frac{2}{r^2}\epsilon^4 - s\frac{2xp_y}{r^3}\epsilon^5\,, \tag{3.63a}$$

$$\Delta\left(\frac{d\boldsymbol{x}}{d\lambda}\right) = \left(0, -\frac{2p_y}{r}\epsilon^4 + s\frac{2x}{r^3}\epsilon^5, 0\right)\,. \tag{3.63b}$$

Due to the non-vanishing $\Delta\left(\frac{dt}{d\lambda}\right)$ we can see both effects for all observers. However, if the observer is located on the $z-$axis, there is no velocity contribution at all, the signal is expected to be smallest. For an equatorial orbit there is no acceleration out of the initial plane due to spin. For an observer on the x-axis there is no velocity component at pericenter but on the rest of the orbits. In order to maximize the signal, the observer should sit on the y-axis.

Second, we consider a **polar orbit** in the yz-plane with pericenter at $z = 0$. The redshift contributions are

$$\Delta\left(\frac{dt}{d\lambda}\right) = \frac{2}{r^2}\epsilon^4\,, \tag{3.64a}$$

$$\Delta\left(\frac{d\boldsymbol{x}}{d\lambda}\right) = \left(-s\frac{2y}{r^3}\epsilon^5, 0, -\frac{2p_z}{r}\epsilon^4\right)\,. \tag{3.64b}$$

All observers see a temporal redshift contribution due to Schwarzschild curvature, but none caused by spin. If the observer is located on the x-axis, he sees a velocity contribution due to spin: the one pushing the satellite out of the Keplerian plane. For an observer on the y-axis, no relativistic velocity contribution is seen at pericenter, and for an observer on the z-axis, a Schwarzschild velocity contribution is seen only.

If we consider a polar orbit with pericenter at $y = 0$ (while still in yz-plane), the redshift at pericenter is determined by

$$\Delta\left(\frac{dt}{d\lambda}\right) = -\frac{2p_t}{r^2}\epsilon^4\,, \tag{3.65a}$$

$$\Delta\left(\frac{d\boldsymbol{x}}{d\lambda}\right) = \left(0, -\frac{2p_y}{r}\epsilon^4, 0\right)\,. \tag{3.65b}$$

For this configuration, no observer on any of the three axes does see a spin effect at pericenter. However, all see a temporal Schwarzschild contribution and an observer on the y-axis does see a Schwarzschild velocity contribution.

All polar orbits have a velocity component pointing out of the Keplerian plane. However, it vanishes at the poles and therefore a polar orbit with pericenter close to a pole will experience less drift compared to one having pericenter closer to the equator.

3.1.6 Keplerian elements

A Keplerian orbit is characterized by the six Keplerian elements: the semi-major axis a, the eccentricity e, the inclination I, the argument of periapsis ω, the longitude of ascending node Ω and the true anomaly ν. Along a perfect Keplerian orbit, the first five elements stay constant while the true anomaly describes the momentary position along the orbit. This corresponds to a purely Newtonian

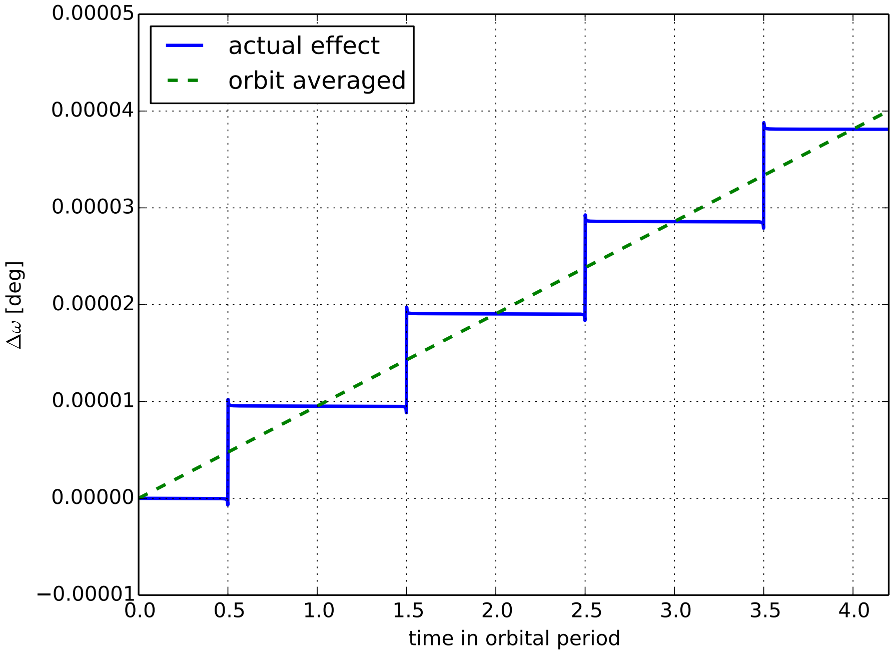

Figure 3.1: Perihelion precession for *Juno* type orbit around Jupiter. The dashed line gives the averaged precession of perihelion $\Delta\omega$ due to Schwarzschild space curvature as given by Eq. (3.66). The solid line shows the actual change along the orbit. We see that during most of the orbit, ω stays essentially the same and only undergoes a significant change during the pericenter passage.

orbit along a spherically symmetric central body. If general relativity is included, this will not hold true anymore and, at first appearance, it might seem that it does not make sense to talk of Keplerian elements at all in relativity. However, we can consider instantaneous Keplerian elements, i.e., at each point along a relativistic orbit we can take its position and velocity and calculate the Keplerian elements of the Keplerian orbit corresponding to the given position and velocity. The elements will now vary continuously along the orbit.

For an eccentric orbit, the change of the Keplerian elements will not happen evenly along the orbit but will peak at pericenter. However, usually the net change of an element averaged over many orbits is considered. For example, the Schwarzschild space curvature leads to a precession of perihelion

$$\Delta\omega_{\mathrm{SS}} = \frac{6\pi}{a(1-e^2)} \tag{3.66}$$

per orbit. Fig. 3.1 shows the precession of perihelion for a typical orbit of the *Juno* orbiter in its final stage when orbiting Jupiter, which is discussed in more detail in section 3.2.4.1. The presence of spin also leads to a perihelion precession, given by [42]

$$\Delta\omega_{\mathrm{Spin1}} = -s\frac{12\pi\cos I}{[a(1-e^2)]^{3/2}} \tag{3.67}$$

per orbit. There is also a non-relativistic perihelion shift due to multipoles. The shift per orbit caused by J_2 is

$$\Delta\omega_{\mathrm{J2}} = \frac{9\pi}{4}\frac{J_2}{(1-e^2)^2}\left(\frac{R}{a}\right)^2\left(1+\frac{5}{3}\cos 2I\right), \tag{3.68}$$

where R is the radius of the central object.

3.2 Prospects for Measuring Planetary Spin and Frame-Dragging in Spacecraft Timing Signals

Andreas Schärer, Ruxandra Bondarescu, Prasenjit Saha, Raymond Angélil, Ravit Helled and Philippe Jetzer

Submitted to Frontiers in Astronomy and Space Sciences [4].

Abstract

Satellite tracking involves sending light signals to Earth. Both the orbit of the satellite and the light signals themselves are affected by the curvature of space-time. The arrival time of the pulses is compared to the ticks of local clocks to reconstruct the orbital path of the satellite to high accuracy, and implicitly measure general relativistic effects. In particular, Schwarzschild space curvature and frame-dragging due to the planet's spin affects the satellite's orbit, and space curvature further affects the path of the signal photons (Shapiro delay). We compute these effects for some current and proposed space missions, using a Hamiltonian formulation in four dimensions which we solve numerically including extended precision. For highly eccentric orbits, such as in the Juno mission and in the Cassini Grand Finale, relativistic effects are not like steady precession as usually envisaged. They instead have a kick-like nature, which could be advantageous for detection if their signature is understood as a function of time. Frame-dragging appears, in principle, measurable by Juno and Cassini, though not by Galileo 5 and 6. Practical measurement would require disentangling frame-dragging from the Newtonian "foreground" such as the gravitational quadrupole. The foreground problem remains to be solved.

3.2.1 Introduction

General relativity describes gravitation as a consequence of a curved four dimensional spacetime. In most astrophysical systems, however, dynamics are dominated by Newtonian physics and GR only provides very small perturbations. Near a mass M, the relativistic perturbations on an orbiting or passing body depend mostly on the pericenter distance, which we call p, in units of the gravitational radius GM/c^2. Newtonian effects are of order $O(p^{-1/2})$. The largest relativistic perturbation is time dilation, and is of $O(p^{-1})$. Space curvature, referring to space-space terms in the metric tensor, enters dynamics at $O(p^{-3/2})$. At $O(p^{-2})$ mixed space-time metric terms enter the dynamics; these correspond to frame-dragging effects, in which a spinning mass drags spacetime in its vicinity and thereby affects the orbit and orientation of objects in its gravitational field. Gravitational radiation corresponds to dynamical effects of $O(p^{-3})$. In post-Newtonian notation, PN X corresponds to $O(p^{-\mathrm{X}-1/2})$. In the Solar System, p is very large in gravitational terms: $\sim 10^8$ or more. In close binary systems p can be much less. In binary pulsars the combination of comparatively low $p \sim 10^5$ with the long-term stability of pulsar timing enables the measurement of relativistic effects down to gravitational radiation[43, 44].

All the same effects are, in principle, present for artificial Earth satellites, but since $p \sim 10^9$, they are much weaker. Nonetheless, the frame-dragging effect of the Earth's spin has been successfully detected in two different ways: the LAGEOS and LARES satellites used laser ranging to measure orbital perturbations from frame-dragging [45, 46]; Gravity Probe B measured the effects of frame-dragging on the orientation of onboard gyroscopes [47–49]. GPS satellites are well known to be sensitive to time dilation [50] and upcoming missions will put ever more precise clocks in orbit. In the Atomic Clock Ensemble in Space (ACES) mission [51], two atomic clocks will be brought to the ISS in order to perform such experiments. However, the ISS is not the optimal place to probe GR and a dedicated satellite on a highly eccentric orbit would be desirable. Its proximity to Earth and high velocity at pericenter boosts relativistic effects and therefore improves the measurements. Several such satellites equipped with an onboard atomic clock and a microwave or optical link on very eccentric orbits, such as STE-QUEST, have been discussed and studied [52]. Such missions would not only be very interesting to probe gravity but also have a plethora of applications, e.g., in geophysics [5, 53].

Missions like *Juno* and *Cassini* present new possibilities for measuring relativistic effects around the giant planets in our Solar System. The basic idea goes back to the early days of general relativity, when Lense and Thirring [54] showed that the orbital plane of a satellite precesses about the spin axis of the planet —that is, what we now call frame-dragging— and identified the expected precession of Amalthea's orbit by $1' \, 53''$ per century as the most interesting case. Recent work has drawn attention to the corresponding precession in the case of *Juno* [55–57].

The classical Lense-Thirring precession is an orbit-averaged effect. This comes with the problem that the very small precession due to relativity is masked by much larger non-relativistic precession, making it very hard to identify the relativistic contribution. For example, only about 7% of Mercury's observed precession is due to relativity. Therefore, it is better to have something with a specific time dependence that can be filtered out. Here, we further study the model problem that was investigated before for terrestrial satellites [3] and the Galactic center [35, 42, 58–62] and apply it to other planets in the Solar System. Since the orbits are dominated by Newtonian physics, and relativity only contributes very small perturbations, their investigation is numerically challenging. Therefore, in some earlier work [3] the orbits were simulated with smaller semi-major axes compared to the real orbit and then, by knowing how the individual effects scale, the redshift curves were obtained by correctly scaling up. Here, we use an arbitrary precision code instead.

Note that we look at an idealized model where a spacecraft, carrying a clock, sends time ticks to a ground station. In contrast, *Juno* and *Cassini* carry transponders that allow two-way signal transfer. That is, we work with spacecraft-to-ground signals, whereas the actual signal is a sum of ground-to-spacecraft and spacecraft-to-ground signals.

To estimate the relativistic effects, we solve for the trajectory of

1. the satellite in a curved spacetime, and
2. the photons (or propagating ticks from the frequency standard) as they propagate to the receiving station

in a given gravitational field. Specifically, we compute the redshift z arising when two photons emitted by the spacecraft at an interval of proper time $\Delta\tau$ travel through curved space-time hitting an observer with a difference in the arrival time $\Delta t = \Delta\tau(1+z)$. Both trajectories are generated numerically via a simulation code that handles multiple scales through variable precision. The effects are modulated by the varying gravitational field.

The paper proceeds as follows: Sec. 3.2.2 describes the approximations we make for the spacetime outside a planet. It presents the Hamiltonian system that is being solved numerically with the higher order relativistic effects, and their respective scalings with orbital size. We then compute the magnitude of the spin parameter, of Schwarzschild precession and frame-dragging effects for the established planets in our Solar System, and report them relative to the effects around Earth for orbits of similar proportionality. Sec. 3.2.4 A and B apply this formalism to the *Juno* and *Cassini* Missions. Sec. 3.2.4 C discusses the Galileo 5 and 6 satellites and other proposed Earth-bound missions. In particular, it discusses the importance of eccentricity in detecting relativistic effects.

Conclusions and potential future directions are presented in Sec. 3.2.5.

3.2.2 General relativistic effects

Calculating relativistic effects fundamentally involves two things: the metric and the geodesic equations. The well-known epigram by J.A. Wheeler states *Spacetime tells matter how to move, matter tells spacetime how to curve.* The metric is known explicitly in terms of the masses, including mass multipoles, and spin rates. The geodesic equations, however, require a numerical solution. We wish to understand how different terms in the metric, in particular the spin part, affect the observable redshift signal. To do this, we will numerically integrate the geodesic equations with different metric terms turned on and off and compare the results.

3.2.2.1 Basic formulation

We work with the geodesic equations in four dimensions, in Hamiltonian form. The independent variable is not time, but the affine parameter, which is just the proper time in arbitrary units. Although the formalism seems complex, it actually tends to lead to simpler equations [3, 3] than other formulations.

For any spacetime metric, the geodesic equations may be expressed in Hamiltonian form as

$$\frac{dx^\mu}{d\lambda} = \frac{\partial H}{\partial p_\mu} \qquad \frac{dp_\mu}{d\lambda} = -\frac{\partial H}{\partial x^\mu} \tag{3.69}$$

where

$$H = \tfrac{1}{2} g^{\mu\nu}(x^\alpha) p_\mu p_\nu \tag{3.70}$$

with $x^\mu = (t, r^i)$ being the four-dimensional coordinates, $p_\mu = (p_t, p_i)$ being the canonical momenta, and λ being the affine parameter.

The satellite at position $\boldsymbol{r} = (r^i)$ orbiting with 4-velocity u^μ_{emit} emits a photon with 4-momentum p^{emit}_μ which arrives at an observer (having velocity u^ν_{obs}) with momentum p^{obs}_ν. The redshift is then given by

$$z = \frac{p^{\text{emit}}_\mu u^\mu_{\text{emit}}}{p^{\text{obs}}_\nu u^\nu_{\text{obs}}} - 1. \tag{3.71}$$

For a distant observer at rest, the redshift for orbital effects reduces to

$$z = \frac{1}{c} u^t_{\text{emit}} - \frac{1}{c} u^{\text{LOS}}_{\text{emit}} - 1, \tag{3.72}$$

where $u^{\text{LOS}}_{\text{emit}}$ is the satellite's velocity along the line of sight.

3.2.2.2 The Hamiltonian

In this subsection we use geometrized units. That is, $\boldsymbol{r}$ is measured in units of GM/c^2 where M is the planetary mass, while t is measured in units of GM/c^3. The momentum is dimensionless. Since the orbits considered are close to Keplerian, the order-of-magnitude relations

$$|\boldsymbol{p}| \sim \frac{v}{c}, \qquad r \sim \left(\frac{v}{c}\right)^{-2} \tag{3.73}$$

will hold, where v is the orbital speed. The 'time-momentum' is constant p_t and its value only affects internal units of a calculation. It is convenient to set $p_t = -1$.

As usual in post-Newtonian celestial mechanics, we order contributions in powers of v/c. These correspond to different physical effects. Moreover, the ordering in powers of v/c is different for the spacecraft orbit and the light signals. Accordingly, we consider two Hamiltonians, as follows.

$$\begin{aligned} H^{\text{orbit}} &= H^{\text{equiv-prin}} + H^{\text{Schwarzschild}} + H^{\text{spin}} \\ H^{\text{signal}} &= H^{\text{Minkowski}} + H^{\text{Shapiro}} \end{aligned} \tag{3.74}$$

Since there is only one spacetime, H^{orbit} and H^{signal} are just different approximations to the same underlying Hamiltonian.

The orbit of the satellite is dominated by

$$H^{\text{equiv-prin}} = -\frac{p_t^2}{2} + \left(-p_t^2\, U(\boldsymbol{r}\,) + \frac{\boldsymbol{p}^{\,2}}{2} \right) \tag{3.75}$$

where $U(\boldsymbol{r})$ is minus the Newtonian gravitational potential, to leading order $1/r$ but also including multipole moments J_n as well as the tidal potential due to the Sun and other planets. The first term on the right is of order unity, while the bracketed part is of order v^2/c^2. This Hamiltonian leads to a Newtonian orbit and redshift contribution of order v/c, together with a time dilation effect of order v^2/c^2. Gravitational time dilation is a basic consequence of the geometric description of spacetime, i.e., the principle of equivalence. Indeed, equation (3.75) is the simplest Hamiltonian consistent with the equivalence principle that gives the correct Newtonian limit. Moving clocks tick slower than stationary ones. So do clocks in a gravitational field. For an orbiting clock, both effects are equal to leading order. The ground station will have its own time dilation too, of course, and the difference is what matters. Time dilation causes the localization of a satellite to be off by kilometers, which has already been taken into account by the first GPS. While this relativistic effect is well established, the Galileo satellites will measure it to unprecedented precision.

Since higher order relativistic effects cause small changes in the redshift, they can be studied perturbatively. We investigate each effect individually by adding it to $H^{\text{equiv-prin}}$, and computing the cumulative redshift. The redshift perturbation is obtained by subtracting the redshift when the effect is artificially turned off.

The next contribution to H^{orbit} is

$$H^{\text{Schwarzschild}} = -\frac{p_t^2}{r^2} - \frac{\boldsymbol{p}^{\,2}}{r^2} \tag{3.76}$$

which introduces the effect of space curvature in the Schwarzschild spacetime. It is easy to verify from equation (3.73) that the Hamiltonian terms are of order $s\,v^4/c^4$, and they contribute to redshift at order $s\,v^3/c^3$.

The leading-order frame-dragging effect arises when adding the term

$$H^{\text{spin}} = -\frac{2p_t}{r^3}\,\boldsymbol{p}\cdot(\boldsymbol{s}\times\boldsymbol{r}). \tag{3.77}$$

This term is of order $s\,v^5/c^5$ and contributes a redshift effect of order $s\,v^4/c^4$. Frame-dragging is due to the rotation of the central mass, which spins with $\boldsymbol{s}$, and depends linearly on the spin parameter $s = |\boldsymbol{s}|$. At next higher order, the dominant term is a spin-squared term, i.e., it is proportional to s^2 [3]. This effect has never been measured before. But since s is quite large for planets (see Table 3.1), probing this effect should be within the scope of future satellite missions.

The main contribution to the redshift comes from the velocity along the line of sight. Therefore, in order to measure a certain relativistic effect, it is desirable to have an orbit-observer-configuration where the relativistic effect has a significant contribution to the line of sight velocity. For first order spin, the leading contribution is given by

$$\Delta z_{\text{spin}} = -\frac{2}{r^2}\boldsymbol{s}\cdot(\hat{r}\times\hat{b}), \tag{3.78}$$

where $\hat{b}$ is the unit vector pointing from the satellite towards the observer. Interestingly, the redshift contribution has no explicit dependence on the satellite's velocity.

The signal photons travel to leading order on a straight line. The leading relativistic effect, leading to a slight bending, is Shapiro delay. This part is best done after transforming to a Solar System frame. The signal Hamiltonian is given by

$$H^{\text{Minkowski}} = -\frac{p_t^2}{2} + \frac{\boldsymbol{p}^2}{2} \tag{3.79}$$

$$H^{\text{Shapiro}} = -U(\boldsymbol{p})\left(p_t^2 + \boldsymbol{p}^2\right). \tag{3.80}$$

At the next order of expansion, further Shapiro-like terms as well as spin terms enter. However, they are expected to be too small to be measured.

3.2.2.3 The spin parameter

The dimensionless spin parameter is given by

$$s = \frac{c}{GM^2}\int \rho(\boldsymbol{x})\,\omega(\boldsymbol{x})\,r_\perp^2\,d^3\boldsymbol{x}\,. \tag{3.81}$$

For solid-body rotation ($\omega = 2\pi/P$, where P is the spin period) the above expression reduces to

$$s = 2\pi \times \text{MoI} \times \frac{c}{gP} \tag{3.82}$$

where

$$\text{MoI} = \frac{1}{MR^2}\int \rho(\boldsymbol{x})\,r_\perp^2\,d^3\boldsymbol{x} \tag{3.83}$$

is the dimensionless moment of inertia and $g = GM/R^2$ is the surface gravity, where R is the notional radius. For realistic density and ω profiles

$$s \sim \frac{c}{gP} \tag{3.84}$$

is still a useful rough estimate. It may be convenient to remember it as the number of days needed to reach the speed of light from an acceleration of one g.

For yet another interpretation of the spin parameter, let us consider two speeds: the surface speed of a spinning planet $v_s \sim R/P$ and the launching speed needed to send something into orbit from the surface $v_l^2 \sim gR$. In terms of these speeds, the approximate formula (3.84) becomes

$$s \sim \frac{cv_s}{v_l^2}. \tag{3.85}$$

The maximal-spinning situation $v_s \approx v_l$ corresponds to a planet spinning so fast that it almost breaks up under centrifugal forces. In this limit $s \sim c/v_l$. Recalling the orders in H^{spin} in equation (3.77), we can see that that Hamiltonian term will be of order v^4/c^4 and the corresponding redshift effect will be of order v^3/c^3. That is, for a low-orbiting spacecraft above a maximally-spinning planet, relativistic spin effects will be comparable in size to space-curvature effects.

3.2.2.4 Keplerian elements

A Keplerian orbit is described by the Keplerian elements a, e, Ω, I and ω. While a and e describe the size and the eccentricity of the ellipse, the 3 angles describe its orientation with respect to some reference plane.

For a relativistic orbit this is not true anymore, as the relativistic effects induce deviations from Keplerian motion. In principle, however, it is still possible to determine the instantaneous Keplerian elements at each point along the orbit: These correspond to a Keplerian orbit having exactly the same velocity as the relativistic one at a given position.

It is well-known that space curvature leads to a precession of the pericenter

$$\Delta\omega_{\mathrm{SS}} = \frac{GM}{c^2}\frac{6\pi}{a(1-e^2)} \tag{3.86}$$

for one orbit.

However, ω is not shifted evenly along the orbit, in fact, there is almost no shift during most of the orbit, but around pericenter there is a kick-like shift. Similarly, there is a precession of the pericenter due to frame-dragging [54, 63]

$$\Delta\omega_{\mathrm{Spin1}} = -s\frac{12\pi\sqrt{GM}\cos I}{[a(1-e^2)]^{3/2}} \tag{3.87}$$

per orbit and also there is a precession of the longitude of the ascending node

$$\Delta\Omega_{\mathrm{Spin1}} = s\frac{4\pi\sqrt{GM}}{[a(1-e^2)]^{3/2}} \tag{3.88}$$

per orbit. Fig. 3.2 shows the precession of the longitude of the ascending node together with the actual shift for a typical *Juno* orbit.

Measuring time-averaged precessions is not actually a useful strategy, because the slightest use of spacecraft engines changes all the Keplerian elements. But similarly to the Keplerian elements, relativistic effects affect the observed redshift in a kick-like manner at pericenter. Therefore, relativistic effects influence a single pericenter passage and when the instrument is accurate enough, they can be probed as a function of time vs. waiting for their build up over many orbits.

3.2.2.5 Scaling

The size of the effects scale with the size of the orbit [35]. For Schwarzschild space curvature and first order spin, the respective scaling laws for the residual redshifts are $\Delta z^{\mathrm{SS}} \sim (r_G/r)^{3/2}$ and $\Delta z^{\mathrm{Spin1}} \sim s(r_G/r)^2$ where $r_G = GM/c^2$ is the gravitational radius. Writing distances in terms of planetary radii $r = \alpha R$, we obtain

$$\frac{\Delta z_1}{\Delta z_2} = \left(\frac{s_1}{s_2}\right)^m \left(\frac{r_G^1}{r_G^2}\frac{r_2}{r_1}\right)^n = \left(\frac{s_1}{s_2}\right)^m \left(\frac{U_1}{U_2}\frac{\alpha_2}{\alpha_1}\right)^n, \tag{3.89}$$

where $U_i = GM_i/(R_i c^2)$ is the gravitational potential at the surface of planet i and $m = 0, 1$ and $n = 3/2, 2$ for Schwarzschild curvature and first order spin effect, respectively. For similar orbits around different planets, i.e., $\alpha_1 = \alpha_2$ with the same eccentricity and identical Keplerian angles, this reduces to $\Delta z_1/\Delta z_2 = (s_1/s_2)^m(U_1/U_2)^n$. Thus, the higher the compactness M/R of a planet, the higher the relativistic effect. For frame-dragging effects, the spin parameter has also to be taken into account.

Using the expression above, we can compare the sizes of relativistic effects of orbits around the planets, the Moon and the Sun to terrestrial orbits. The ratio between the signals for similar orbits is given in Table 3.1.

3.2.3 Planetary parameters

The planetary parameters relevant for calculating relativistic effects are summarised in Table 3.1. The Moon and the Sun are also included for comparison.

The values of the gravitational potential U at the surface are ordered as one might expect. Jupiter with 2×10^{-8} has the highest, while for the Earth the value is 30 times smaller.

The values of the spin parameter may be surprising. Black holes must have $s < 1$ as is well known, but planets can have $s \gg 1$. Mars has the highest $s \sim 2090$, while Venus has the lowest $s \sim 3$, but most planets have an s with a value that is typically in the hundreds. Incidentally, the Sun's spin parameter will be small: The Sun has a much larger g than any planet, and it spins differentially, roughly once a month; as a result, the Sun has a much smaller s than the Earth. The uncertainty in s depends on the uncertainties in the MoI and in the spin period.

Although neither the density profile nor internal differential rotation can be measured directly, internal-structure models provide MoI values for the gas giants, and these are thought to be accurate to a few percent [55, 64, 65]. The Radau-Darwin approximation [66] relates the MoI to the gravitational quadrupole J_2 and the ratio of centrifugal to gravitational acceleration at the equator. The estimated MoI is ~ 0.265 for Jupiter [55] and ~ 0.220 for Saturn [64, 67]. Evidently, Saturn is more centrally condensed than Jupiter.

The rotation period remains somewhat uncertain for all the giant planets other than Jupiter [68–70]. Saturn's internal rotation period is unknown to within $\sim$ 10 minutes. It has been acknowledged that the rotation period is unknown since *Cassini*'s Saturn kilometric radiation (SKR) measured a rotation period of 10h 47m 6s [71], longer by about eight minutes than the radio period of 10h 39m 22.4s measured by Voyager [72]. In addition, during *Cassini*'s orbit around Saturn the radio period was found to be changing with time. It then became clear that SKR measurements do not represent the rotation period of Saturn's deep interior. Due to the alignment of the magnetic pole with the rotation axis, Saturn's rotation period cannot be obtained from magnetic field measurements [73]. Theoretical efforts to infer the rotation period [70, 74, 75] indicate further sources of uncertainty. Saturn's rotation period is thought to be between $\sim$ 10h 32m and $\sim$ 10h 47m. For Uranus and Neptune, the uncertainty could be as large as 4% and 8%, respectively [68].

A further complexity arises from the fact that the giant planets could have non-body rotations (e.g., differential rotation on cylinders/spheres) and/or deep winds. However, in that case, the deviation from a mean solid-body rotation period is expected to be small. Future space missions to Uranus and/or Neptune, performing accurate measurements of their gravitational fields, could be used to determine the spin parameter of these planets.

3.2.4 Relativistic effects for current and planned missions

We now consider missions to Jupiter, Saturn and Earth orbit.

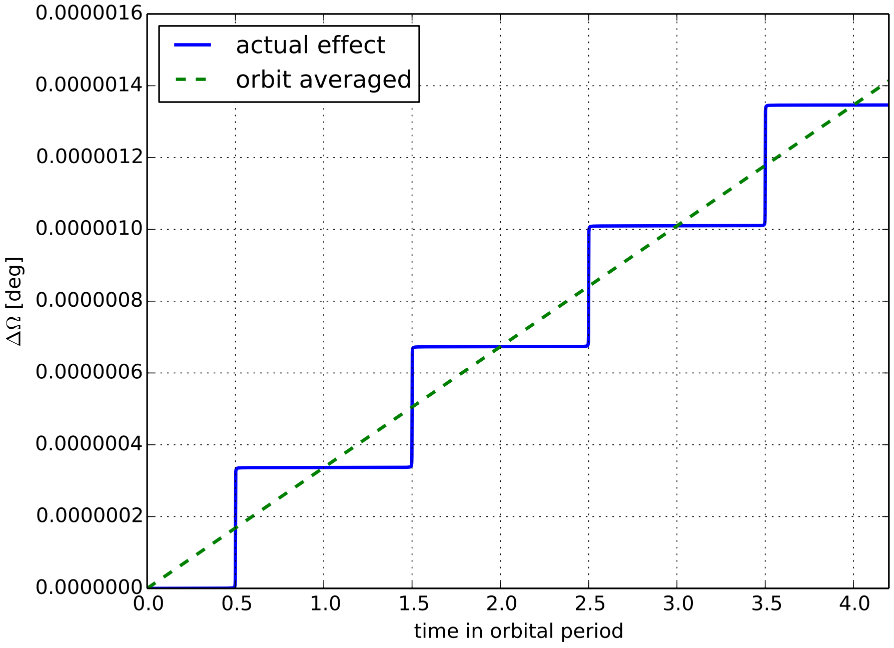

Figure 3.2: Change of the longitude of the ascending node Ω for a typical *Juno* orbit due to spin. The solid line shows the actual change of Ω, while the dashed line represents the averaged change given by Eq. (3.88).

3.2.4.1 Jupiter orbit

On July 4, 2016, the *Juno* mission arrived at Jupiter and started orbiting the planet. It is equipped to perform high precision measurements (operating at X-band and Ka-band) of its gravitational field. The 53-days orbits are polar with perijove being at ~ 1.09 Jupiter radii and apojove at ~ 120 Jupiter radii. Such orbits provide ideal conditions for gravitational field measurements, and allow the spacecraft to avoid most of the Jovian radiation field. After more than four years of measurementes and ~ 32 orbits around Jupiter, *Juno* is planned to make one last orbit and then perform the deorbiting maneuver (see e.g., [76]).

We compute the leading-order relativistic effects for the *Juno* mission. They measure the precession of the orbit due to the curvature of the spacetime and contain a part that accumulates as well as a transient part, which has never been measured. The effect that occurs due to the Schwarzschild term in the Hamiltonian produces a Mercury-like precession (solid red curve), while the other is referred to as frame-dragging due to the spin of Jupiter. Measuring the latter directly constrains the spin parameter of the planet, which is proportional to its moment of inertial and angular momentum. It thus reveals important information about the planet's internal density structure that is not necessarily identical to that contained in the gravitational moments.

The *Juno* orbiter has already entered a highly elliptical polar orbit around Jupiter. It is measuring deviations in the velocity of the spacecraft $\sim 10\mu m/\mathrm{sec}\ (\tau/60\ \mathrm{sec}\ )^{-1/2}$. This corresponds to a sensitivity to redshift change of $\Delta z \sim 3 \times 10^{-14}$.

At each pericenter passage of *Juno*, both the instantaneous Keplerian elements and the orientation to the observer change. Therefore, in order to discuss relativistic effects on the basis of the *Juno* mission, we consider a typical orbit with average values $a = 60 \times R_{\mathrm{Jupiter}}$, $e = 0.981$, $\Omega = 253°$, $I = 93.3°$, $\omega = 170°$ and observer position $\theta_{\mathrm{obs}} = 92.9°$ (polar angle), $\phi_{\mathrm{obs}} = 15.0°$ (azimuthal angle). Fig. 3.3 shows the characteristic redshift curves for the different effects for such a *Juno* orbit. For all science

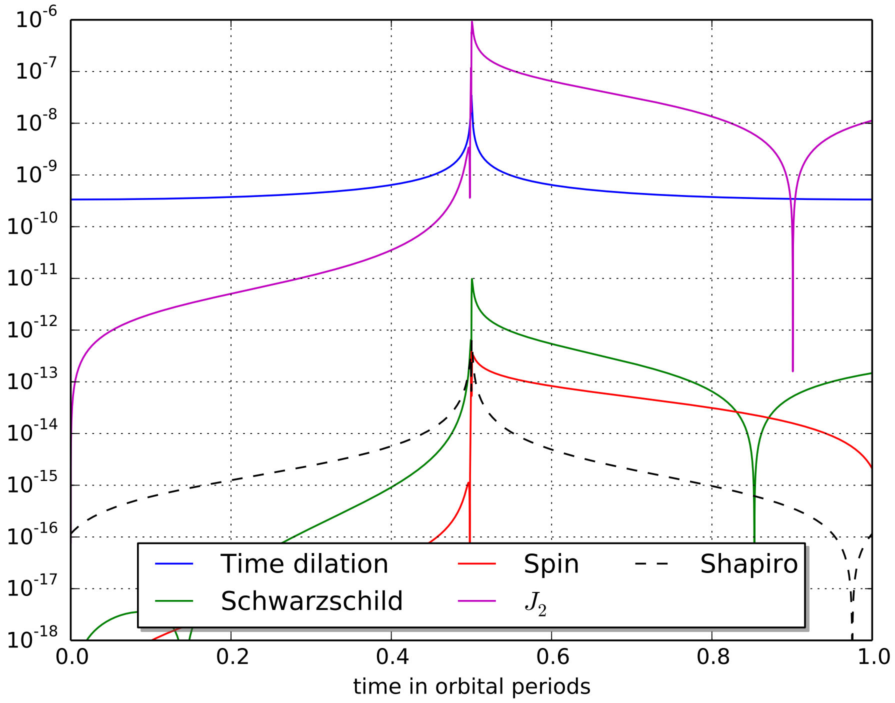

Figure 3.3: Higher order relativistic effects for the *Juno* orbiter. The plot shows the magnitude of the redshift signal due to the different relativistic effects. The parameters chosen correspond to a typical science orbit. The curves change slightly for other orbits, however, the order of magnitude of the effects is the same. Also the Newtonian effect due to J_2 is shown.

orbits, the sizes of the effects, in particular of the spin effect, are similar.

Fig. 3.4 shows the part in the redshift due to the presence of Jupiter's spin over one orbit. After pericenter passage, the relativistic and the non-relativistic orbit are out of sync and a comparison does not make sense anymore. The lower panel of the figure zooms into the peak around pericenter, revealing that the interesting time span is of order ~ 1 hour. This is the phase that needs to be observed in order for seeking the characteristic imprint of frame-dragging in the redshift data.

Over any one orbit, only one component of the spin vector contributes at leading order, namely the spin component along $\hat{r}_{\mathrm{peri}} \times \hat{b}$ (see Eq. 3.78). To be sensitive to all components of the spin, orbits with different orientations of $\hat{r}_{\mathrm{peri}} \times \hat{b}$ are needed. Fig. 3.5 shows the polar and azimuthal angles of this vector for all the *Juno* science orbits. The orientations are varied, and hence *Juno* is sensitive to all three components of the spin vector.

The frame-dragging effect will, moreover, be a pathfinder to measuring yet weaker effects. The spin terms depend on the spin profile inside the planet. Measuring the spin profile would therefore play a role in constraining planet properties and formation models. Future deep-space missions could enable tests of general relativity around other planets in the Solar System whose composition and internal structure are unknown.

3.2.4.2 Saturn orbit

The *Cassini* mission is planned to finish its exploration of the Saturnian system with proximal orbits around Saturn that will provide accurate measurements of the gravitational field of the planet. The *Cassini* spacecraft is planned to execute 22 highly inclined (63.4 degree) orbits with a periapsis of

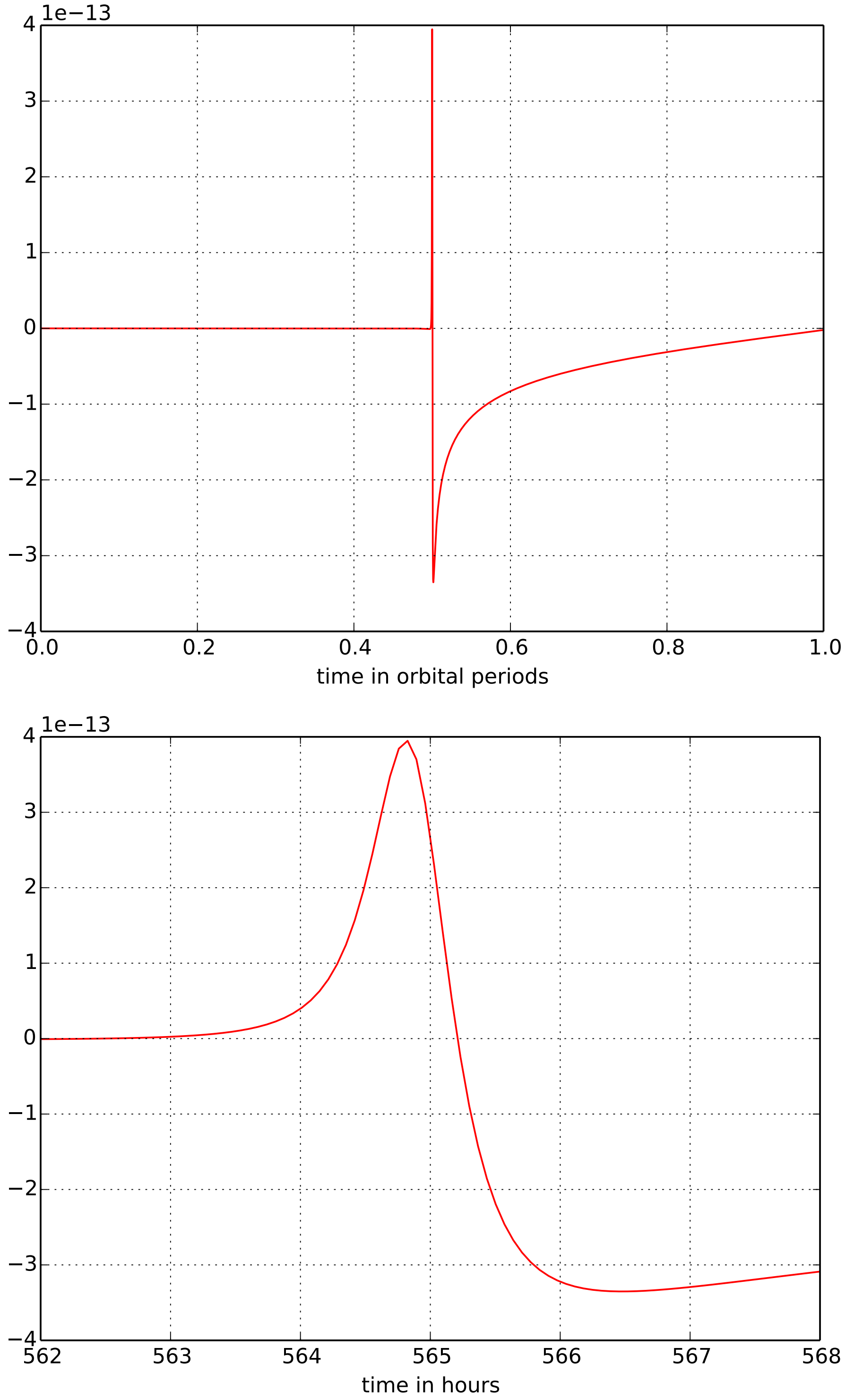

Figure 3.4: *Upper:* contribution to the redshift from frame-dragging by Jupiter's spin, for the same orbit as in Fig. 3.3. The signal peaks at the orbit pericenter passage. *Lower:* zoom into pericenter passage.

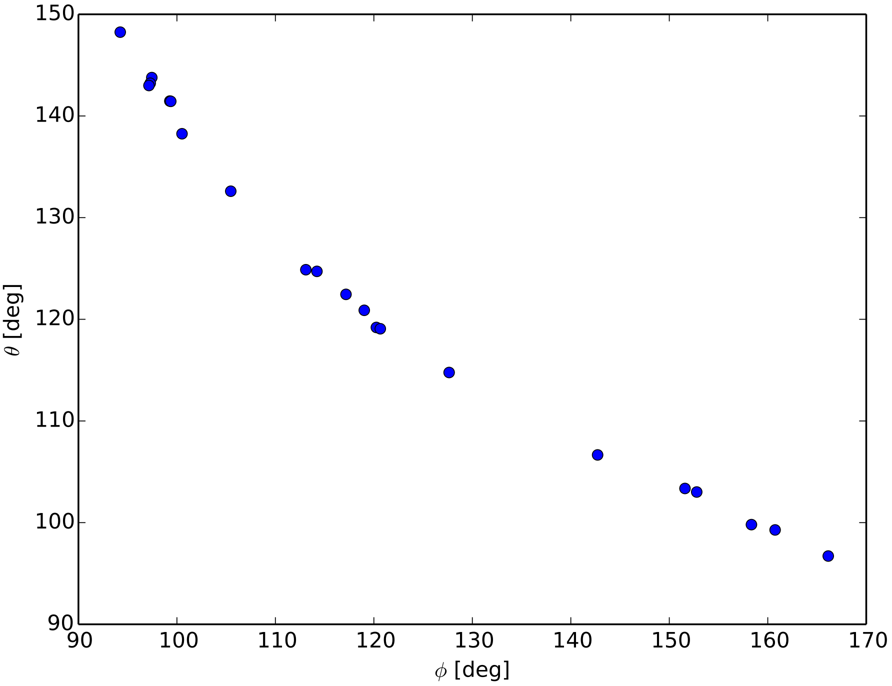

Figure 3.5: Orientation of the vector $\hat{r}_{\text{peri}} \times \hat{b}$ for *Juno* science orbits. Here $\hat{b}$ is the line of sight to *Juno*, and θ, ϕ in the Figure are with respect to to Jupiter's axis. The timing signal is sensitive to the planetary spin projected along these various directions.

$\sim$ 1.02 Saturn radii [77]. These proximal orbits, known as *Cassini Grand Finale*, operating at X-band, are also ideal for gravity measurements. They are expected to provide range rate accuracies of $\sim 12\mu$m/sec at 1000 second integration times, being about four times noisier than *Juno*.

Both the *Juno* and the *Cassini* spacecrafts will terminate their operations by descending into the atmospheres of Jupiter and Saturn, respectively, and will disintegrate and burn up in order to fulfill the requirements of NASA's Planetary Protection Guidelines.

Cassini has a sensitivity that is about $\Delta z \sim 10^{-13}$. Relativistic effects peak around the pericenter with the frame-dragging effect of maximum amplitude $\sim 10^{-13}$ and the Schwarzschild curvature term of $\sim 10^{-11}$. Ideally, the goal would be to resolve both the Schwarzschild and frame-dragging parts of the precession as a function of time. If they can be modeled effectively, they would be less likely to be drowned by Newtonian noise than as a cumulative effect.

Fig. 3.6 shows the corresponding curves for a typical *Cassini* orbit. For *Cassini*, we chose the values $a = 10 \times R_{\text{Saturn}}$, $e = 0.9$, $\Omega = 175°$, $I = 62°$, $\omega = 187°$, $\theta_{\text{obs}} = 63.3°$ and $\phi_{\text{obs}} = -5°$.

3.2.4.3 Earth orbit

Next we discuss satellites in Earth orbit. To illustrate the importance of eccentricity, Fig. 3.7 shows the redshift curve for a typical terrestrial satellite with a low eccentricity ($e = 0.1561, a = 27'977$km) as for the Galileo 5 & 6 satellites and a high eccentricity ($e = 0.779, a = 32'090$km) orbit while leaving all other Keplerian elements as well as the observer's position constant. However, the actual curve depends highly on the orientation of the orbit and the position of the observer and must be computed individually for each orbit-observer-configuration. Also, that the visibility of the satellite around pericenter might not be provided needs to be taken into account. For the Galileo satellites, the curve would be significantly flatter - without a clear peak around pericenter due to the low eccentricity.

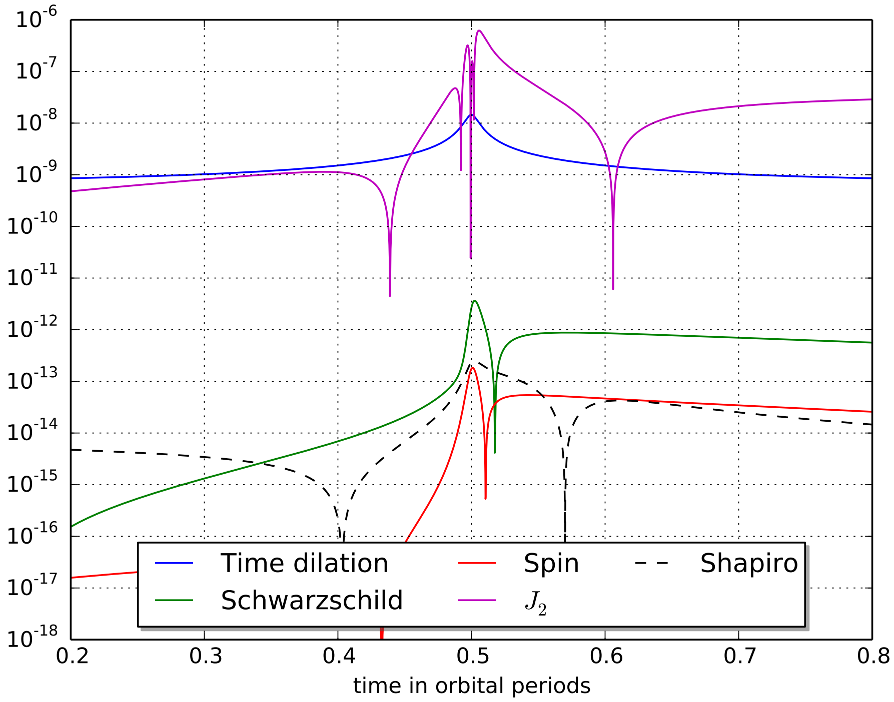

Figure 3.6: Higher order relativistic effects for *Cassini*.

The only relativistic effect that is within the measurability range is the Schwarzschild space curvature effect.

3.2.5 Conclusions

A spinning body causes spacetime to rotate around it, thus making nearby angular momentum vectors precess. This had already been considered theoretically in the early days of general relativity [54]. Only in recent years, however, has the effect entered the experimental realm [45–47].

Frame-dragging is usually thought of as a steady precession. For highly eccentric orbits, however, this is far from the case. While having a minor impact along most of the orbit, frame-dragging kicks in around pericenter. This can be seen in Fig. 3.2 which shows the change of the longitude of ascending node due to spin for some example orbits of the *Juno* spacecraft. An analogous situation applies to the S stars in orbit around the Galactic-center black hole [61]. We suggest that these pericenter-kicks could provide a distinctive signature in timing signals obtained from spacecraft tracking.

The frame-dragging contribution to the redshift of spacecraft signals is

$$\Delta z_{\text{spin}} = -2\left(\frac{GM}{c^2 r}\right)^2 \boldsymbol{s}\cdot(\hat{r}\times\hat{b}) \tag{3.90}$$

(given in geometrized units as Eq. 3.78) where $\hat{b}$ is the line of sight to the spacecraft, and $\boldsymbol{s}$ is the dimensionless spin vector. Substituting the approximation expression (3.84) for the spin parameter, and assuming that the spacecraft has a low pericenter, so that r_{peri} is of the same order as the planetary radius, gives

$$\Delta z_{\text{spin}} \sim \frac{GM}{c^3 P} \tag{3.91}$$

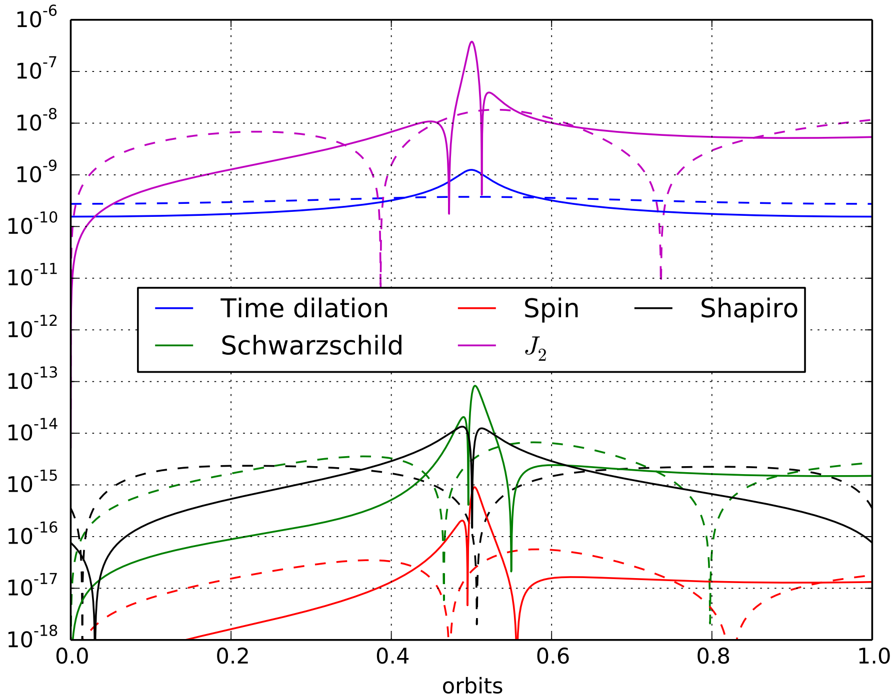

Figure 3.7: Redshift curves of terrestrial satellites. The dashed curves give the results for an orbit with the semi-major axis and eccentricity corresponding to the ones of the Galileo 5 & 6 satellites. The solid lines give the results for a typical satellite with high eccentricity while all the other Keplerian elements and the observer's position were left the same.

where P is the spin period. Jupiter has $GM/c^3 \sim 5\,\mathrm{nanosec}$ and $P \sim 10\,\mathrm{hr}$, indicating $\Delta z_{\mathrm{spin}} \sim 10^{-13}$. Furthermore, as Fig. 3.4 shows, the frame-dragging signal is concentrated over a duration of two hours around the pericenter.

Figures 3.3, 3.6 and 3.7 show example orbits of *Juno, Cassini,* and the eccentric *Galileo* spacecraft respectively. They also show the effect of the quadrupole J_2, which is orders of magnitude larger than the spin effect, but has a different time dependence.

Measurability centers on whether the frame-dragging signal can be disentangled from the much larger quadrupole and other "foreground" effects. The specific and known time-dependence of the frame-dragging signal offers some hope of doing so, but the question remains open.

Object	$U \equiv GM/(c^2R)$	$g \equiv GM/R^2$ $[m/s^2]$	MoI	s	spin period [days]	$\frac{\Delta z_{\mathrm{SS,Obj}}}{\Delta z_{\mathrm{SS,Earth}}}$	$\frac{\Delta z_{\mathrm{Spin,Obj}}}{\Delta z_{\mathrm{Spin,Earth}}}$
Mercury	1.00×10^{-10}	3.7	0.35	35.2	58.65	5.5×10^{-2}	9.9×10^{-4}
Venus	5.98×10^{-10}	8.9	0.33	3.3	243.02	8.0×10^{-1}	3.3×10^{-3}
Earth	6.95×10^{-10}	9.8	0.3308	738.3	1.00	1.0	1.0
Moon	3.12×10^{-11}	1.6	0.394	194.8	27.32	9.5×10^{-3}	5.3×10^{-4}
Mars	1.40×10^{-10}	3.7	0.366	2093.5	1.02	9.1×10^{-2}	1.2×10^{-1}
Jupiter	2.02×10^{-8}	25.9	0.265	564.0	0.41	1.6×10^{2}	6.4×10^{2}
Saturn	7.00×10^{-9}	10.4	0.21	988.0	0.44–0.45	3.2×10^{1}	1.4×10^{2}
Uranus	2.52×10^{-9}	8.9	0.225	770.1	0.67–0.76	6.9	1.4×10^{1}
Neptune	3.06×10^{-9}	11.1	0.236	691	0.63–0.71	9.2	1.8×10^{1}
Sun	2.12×10^{-6}	273.7	0.07	0.2	25.05	1.7×10^{5}	2.8×10^{3}

Table 3.1: Gravitational and spin parameters for the planets and the Moon. For the gravitational potential U and acceleration g, values at the surface are given; values from orbit will be somewhat smaller. MoI values for the giant planets are derived using interior models that reproduce the gravitational fields of the planets [70]. All other quantities are derived using parameters provided by NASA [http://nssdc.gsfc.nasa.gov/planetary/factsheet]. The two columns on the right give the ratio between the redshift signals of orbits around the respective object and the signals for a similar orbit around Earth.

Chapter 4

Geophysical Applications of General Relativity

4.1 Atomic clocks as tools to monitor vertical surface motion

R. Bondarescu, Andreas Schärer, Andrew Lundgren, György Hetényi, Nicolas Houlié, Philippe Jetzer and Mihai Bondarescu

Published in Geophys. J. Int. **202**, 1770 (2015) [5].

Abstract

According to general relativity, a clock experiencing a shift in the gravitational potential ΔU will measure a frequency change given by $\Delta f/f \approx \Delta U/c^2$. The best clocks are optical clocks. After about 7 hours of integration they reach stabilities of $\Delta f/f \sim 10^{-18}$, and can be used to detect changes in the gravitational potential that correspond to vertical displacements of the centimetre level. At this level of performance, ground-based atomic clock networks emerge as a tool that is complementary to existing technology for monitoring a wide range of geophysical processes by directly measuring changes in the gravitational potential. Vertical changes of the clock's position due to magmatic, post-seismic or tidal deformations can result in measurable variations in the clock tick rate. We illustrate the geopotential change arising due to an inflating magma chamber using the Mogi model, and apply it to the Etna volcano. Its effect on an observer on the Earth's surface can be divided into two different terms: one purely due to uplift (free-air gradient) and one due to the redistribution of matter. Thus, with the centimetre-level precision of current clocks it is already possible to monitor volcanoes. The matter redistribution term is estimated to be 3 orders of magnitude smaller than the uplift term. Additionally, clocks can be compared over distances of thousands of kilometres over short periods of time, which improves our ability to monitor periodic effects with long-wavelength like the solid Earth tide.

4.1.1 Introduction

Vertical deformation transients are key to characterising many geological processes such as magmatic or tectonic deformation (Fig. 4.1). Many of these processes have timescales from hours to years which are difficult to measure with existing instruments. Atomic clocks provide a new tool to resolve vertical displacement, with a current precision of about 1 cm in equivalent height after an integration time of 7 hours [34, 78, 79].

In the past, we argued [53] that clocks provide the most direct local measurement of the geoid, which is the equipotential surface (constant clock tick rate) that extends the mean sea level to continents. Since a clock network is ground-based, it can provide variable spatial resolution and can be used to calibrate and add detail to satellite maps, which suffer from aliasing (errors due to effects faster than the sampling rate) and from the attenuation of the gravitational field at the location of the satellite.

In this paper, we consider dynamic sources that cause both vertical displacement and underground mass redistribution which produce changes in the local geopotential. Geopotential differences ΔU are directly measured by the changes in clock tick rate $\Delta f/f \approx \Delta U/c^2$, where c is the speed of light. To be useful, a clock must always be compared to a reference clock, which could be nearby or thousands of kilometres away. Clocks are connected via ultra-precise fiber links that are capable of disseminating their frequency signals over thousands of kilometers with a stability beyond that of the clock [80]. As a concrete example we present the case of the inflation (or deflation) of an underground magma chamber, computed analytically [81], and apply it to the Etna volcano. We explore whether the magma filling could be detected using one or two clocks located on the volcanic edifice.

The primary tools currently used to monitor vertical displacement are InSAR and GPS. Interferometric Synthetic Aperture Radar (InSAR) measures millimetre displacements in the line of sight of radar satellites over wide areas (e.g. Bürgmann *et al.* 2000; Biggs *et al.* 2011), but with limited sampling rates (days to weeks). GPS is able to measure vertical displacements of 1 cm over short timescales ($\sim$ an hour) only when the displacement is very localized in the network and/or the frequency of motion is different from the frequency of various artefacts that impact GPS accuracy. After surveying areas for more than 10 years, the level of accuracy of GPS techniques is close to the millimetre level [82, 83] or better, enabling us to better characterize the crustal elastic contrast of plate boundaries [84, 85]. Since the primary source of noise in GPS measurements is due to signal dispersion through the atmosphere, both differential GPS and post-processed GPS data perform better if networks are dense (e.g. Khan *et al.* 2010; Houlié *et al.* 2014) because many artefacts cancel across networks over which the ionosphere and troposphere can be assumed to be constant. For timescales of seconds, broadband seismometers can be used [86], but their bandwidth is unsuited for resolving long-term displacements [87].

Unlike the GPS or InSAR measurements, local atomic clock measurements are insensitive to atmospheric perturbations, and could resolve ground displacement over shorter integration timescales (hours to months). Further, clocks in conjunction with gravimeters are also able to resolve density changes in the Earth crust that do not, or just partially, lead to uplift or subsidence. In the case of a spherical magma chamber, the geopotential term resulting from mass redistribution is inversely proportional to the distance to the source $\sim 1/R$, whereas the ground displacement term scales with $1/R^2$. As opposed to this, both terms have the same $1/R^2$ scaling in gravity surveys. Comparing the measured gravity change to the uplift, $\Delta g/\Delta h$, can reduce this degeneracy to model processes a volcano is undergoing before eruption [88]and also more general processes (see Fig. 1 and De Linage *et al.* 2007).

Even in areas without active seismic or volcanic processes, the solid Earth tide has a vertical amplitude that can be as high as 30 cm [89] with a semi-diurnal period, whose amplitude can be monitored by an atomic clock that is compared with a distant reference clock. We find that geopotential and gravity measurements are sensitive to two different combinations of tidal Love numbers, and could be used to calibrate existing measurements of the solid Earth tide.

4.1.2 Overview of atomic clocks

According to Einstein's theory of general relativity, time slows down in the vicinity of massive objects. On a neutron star, clocks tick at about half their rates on Earth. An observer outside the horizon of

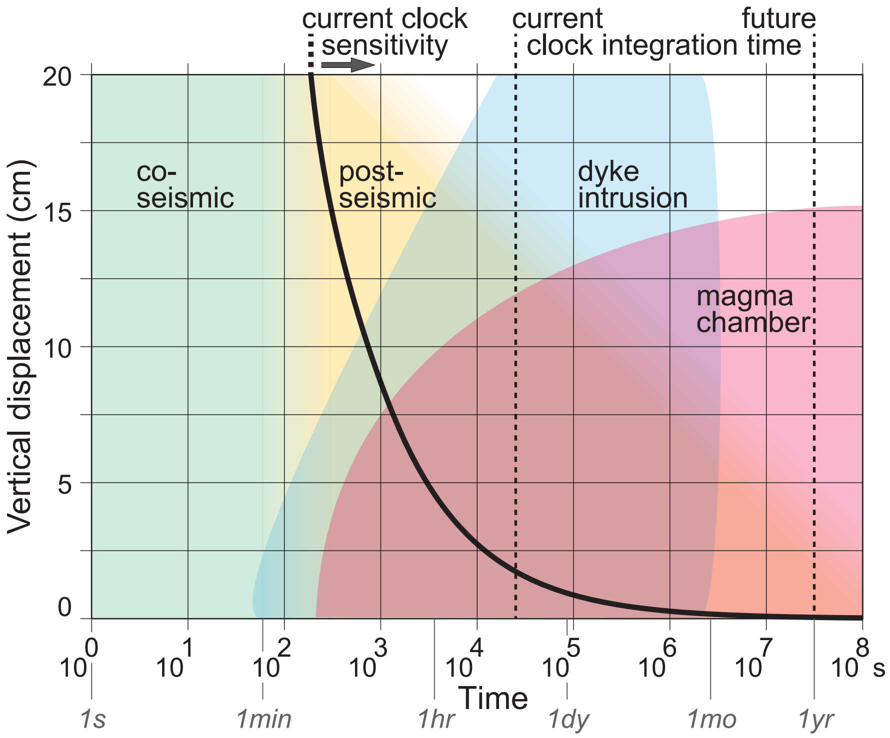

Figure 4.1: Phenomena that could be monitored with optical clock networks. The black line shows the lower sensitivity of today's best optical clocks; see equation (4.1) and Δz_{today} in (4.7). The vertical dashed lines show current and planned clock integration times.

a black hole even sees time stopping all together at the horizon. Similarly, clocks that are closer to Earth tick slightly slower than clocks that are further away.

Atomic clocks employ atomic transitions that are classified, depending on the transition frequency, as either microwave or optical clocks. Since the clock frequency depends only on a known atomic transition and constants of nature, clocks respond identically to changes in the gravitational potential and do not require calibration. This is in contrast to relative gravimeters, which suffer from instrument drift and have to be calibrated via comparisons with other measurements at the same location. The current definition of the second is based on a microwave atomic clock. However, optical clocks have the potential for higher stability because they utilize atomic transitions with resonance line-widths typically 10^5 narrower than microwave transitions. Since the development of the femtosecond laser frequency comb, optical clocks have been improving extremely rapidly [33]. Today's best clocks are optical. They are laboratory devices with frequency uncertainty

$$\Delta f/f \sim 3\times 10^{-16}/\sqrt{\tau/\text{sec}}, \tag{4.1}$$

where τ is the integration period [34, 78, 79], and are likely to continue to improve dramatically within the next decade [33]. A transportable optical clock that monitors and compensates for environmental effects (temperature, pressure, electric and magnetic fields) and fits within two cubic meters has recently been built [90].

In the future, it is expected that clocks will become sensitive to surface displacements at the sub-millimetre level. Possible techniques include nuclear optical transitions [91], optical transitions in Erbium [92], and transitions in highly charged ions [93]. A stability of

$$\Delta f/f \sim \sigma_{\text{tomorrow}} = 10^{-17}/\sqrt{\tau/\text{sec}} \tag{4.2}$$

should be possible [78], which would achieve $\Delta f/f \sim 10^{-20}$ within one month.

In order to take full advantage of the improved stability of optical clocks, distant clocks have to be compared reliably to the 10^{-18} level. This entails a global understanding of vertical displacements, the solid Earth tide, and, overall, of the geoid to the 1-cm level. Any effects that cause perturbations to this level would have to be reliably modelled and understood. Clock comparisons via satellites are currently limited by the precision of the communication link that passes through a potentially turbulent atmosphere. The most precise comparisons of distant clocks currently use underground optical fiber links. Optical frequency transfer with stability better than the clock has been demonstrated over a two-way distance of 1840 km [80], with a fiber-link from Braunschweig, Germany to Paris, France. A fiber-link network capable of disseminating ultra-stable frequency signals is being planned throughout Europe (e.g. NEAT-FT collaboration, REFIMEVE+).

4.1.3 Methods

While clocks are sensitive to changes in the gravitational potential, relative gravimeters see changes in the vertical component of the gravitational acceleration, which is a vector ($\boldsymbol{g} = -\boldsymbol{\nabla} U$) whose amplitude can generally be measured much better than its direction. They both provide local measurements of the change in gravity or potential relative to a reference point where the gravity and potential are known accurately. Within a large fiber links network, the reference clock could be very far away.

For a displacement z, the geopotential and gravity changes are

$$\Delta U \approx -\frac{GM_\oplus}{R_\oplus^2}\, z, \;\; \Delta g \approx \frac{2GM_\oplus}{R_\oplus^3}\, z. \tag{4.3}$$

where G is the gravitational constant, and $M_\oplus$ and $R_\oplus$ the mass and radius of the Earth. The well-known free-air correction Δg for gravity is the gradient of the potential change ΔU.

A vertical displacement of $z = 1$ cm causes changes in the geopotential and in gravity of

$$\Delta U \approx 0.1 \left(\frac{z}{1\ \mathrm{cm}}\right) \frac{\mathrm{m}^2}{\mathrm{sec}^2}, \tag{4.4}$$

$$\Delta g \approx 3 \times 10^{-8} \left(\frac{z}{1\ \mathrm{cm}}\right) \frac{\mathrm{m}}{\mathrm{sec}^2} \sim 3 \left(\frac{z}{1\ \mathrm{cm}}\right) \mu\mathrm{gal}. \tag{4.5}$$

Thus, the frequency of a clock changes by

$$\frac{\Delta f}{f} \approx \frac{\Delta U}{c^2} \sim 10^{-18} \left(\frac{z}{1\ \mathrm{cm}}\right). \tag{4.6}$$

The solid line in Fig. 4.1 is the vertical displacement $\Delta z_{\mathrm{today}}$ as a function of clock integration time τ, which is obtained by equating (4.1) and (4.6), while $\Delta z_{\mathrm{tomorrow}}$ results from (4.2) and (4.6).

$$\Delta z_{\mathrm{today}} \approx 300 \left(\frac{\tau}{\mathrm{sec}}\right)^{-1/2} \mathrm{cm}, \;\; \Delta \mathrm{z}_{\mathrm{tomorrow}} \approx 10 \left(\frac{\tau}{\mathrm{sec}}\right)^{-1/2} \mathrm{cm}. \tag{4.7}$$

4.1.4 Applications

We first discuss the geopotential and gravity changes caused by an inflating magma chamber, using the Mogi model. This is followed by a discussion of the measurability of the solid Earth tides.

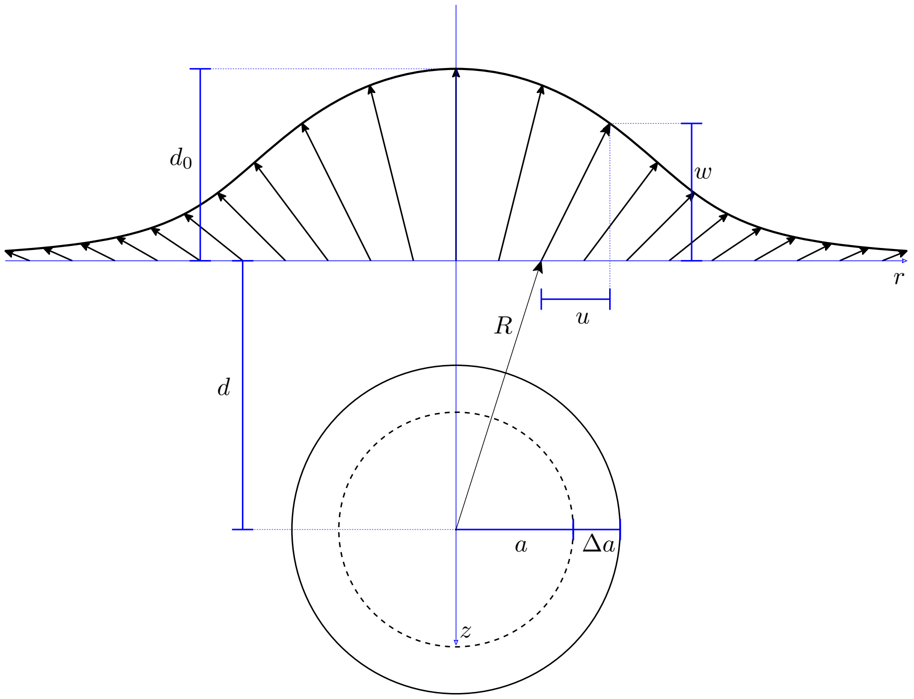

Figure 4.2: Deformation due to inflating cavity.

4.1.4.1 Inflating magma chamber - the Mogi model

An inflating or deflating magma chamber can be described by the so-called "Mogi model" [81]: an isolated point pressure source in an elastic half-space that undergoes a pressure change. The Mogi model is broadly used in the literature (e.g. [94, 95]). Recently, its predictions were compared to sophisticated simulations, which showed that in many situations the discrepancy is quite small [96].

First, we discuss the Modi model in detail. Then, we apply the model to a volcano, in particular the Etna volcano.

A Mogi source is an isolated pressure point source embedded in an elastic half-space. A pressure change ΔP deforms the surrounding half-space and uplifts an observer standing on the surface. This ground displacement, discussed in Sec. 4.1, affects the ticking rate of a clock since its position in the Earth's gravitational field is slightly shifted. Besides that, there are three additional effects affecting both the gravitational potential and acceleration, which are due to the redistribution of matter.

We choose coordinates such that the elastic half-space extends from minus to plus infinity in both the x and y directions, and from 0 to $+\infty$ in the z direction. The source is located at $(0, 0, d)$ and an observer positioned on the surface has coordinates $(x, y, 0)$. By symmetry, we typically use coordinates (r, z), where $r \equiv \sqrt{x^2 + y^2}$ is the distance from the observer to the place on the surface directly above the cavity. A scheme is given in Fig. 4.2.

Even though a point source is considered, the pressure change can be interpreted as the volume change ΔV of a finite size cavity. This approximation is valid as long as the radius of the cavity is much smaller than the depth d. Such a volume change can, for example, be caused by the inflation or deflation of a magma chamber.

The radius of the cavity changes by [97]

$$\Delta a = \frac{a\Delta P}{4\mu}, \tag{4.8}$$

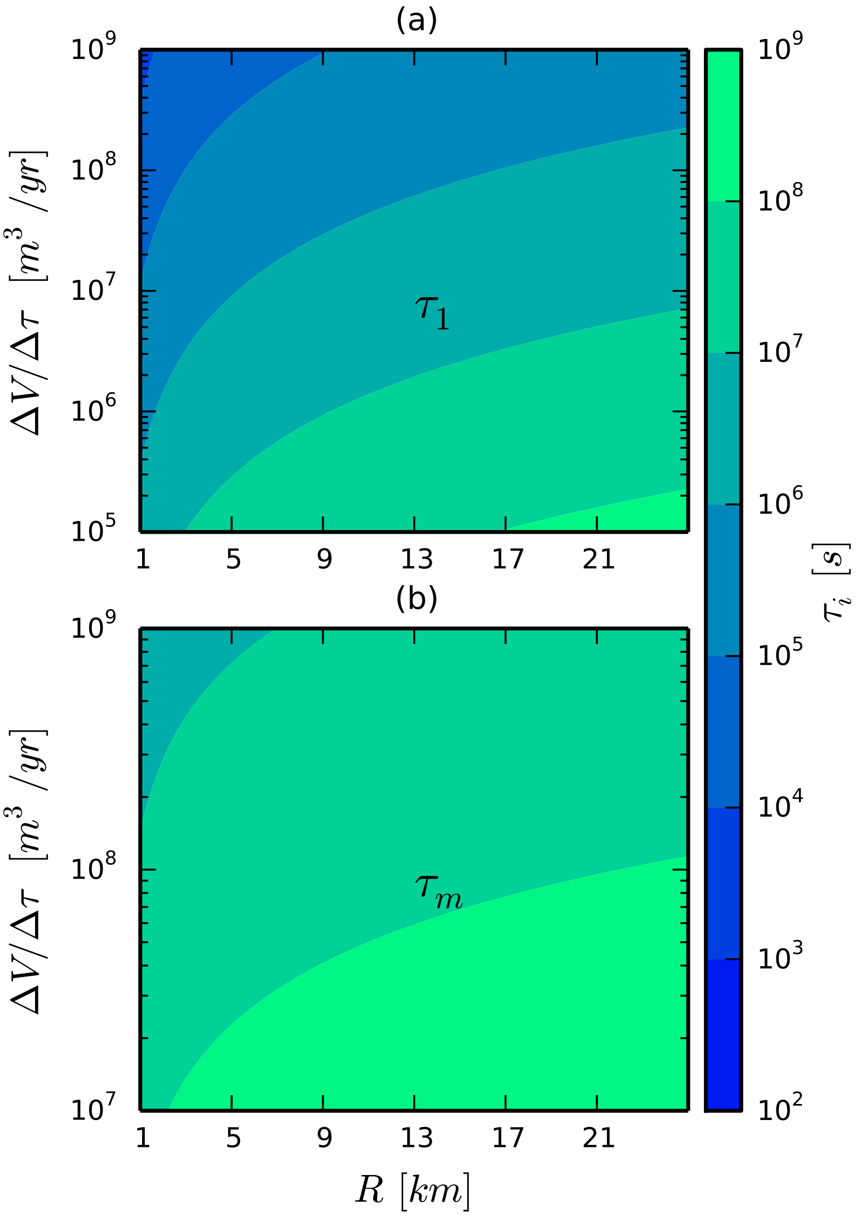

Figure 4.3: Integration times for current clocks. Considering a clock with $\sigma_0 = 3 \times 10^{-16}$, the required integration time to resolve uplift (Eq. (13) is shown in (a) as a function of distance R and (constant) volume change rate $\Delta V/\Delta\tau$. Here, it is assumed that the clock is placed above the magma chamber ($r = 0$). Analogous, the integration time for seeing the redistribution of mass (Eq. (14) is shown in (b). In contrast to the uplift where the result depends on both r and d, the integration time for the mass redistribution term depends on the total distance R only.

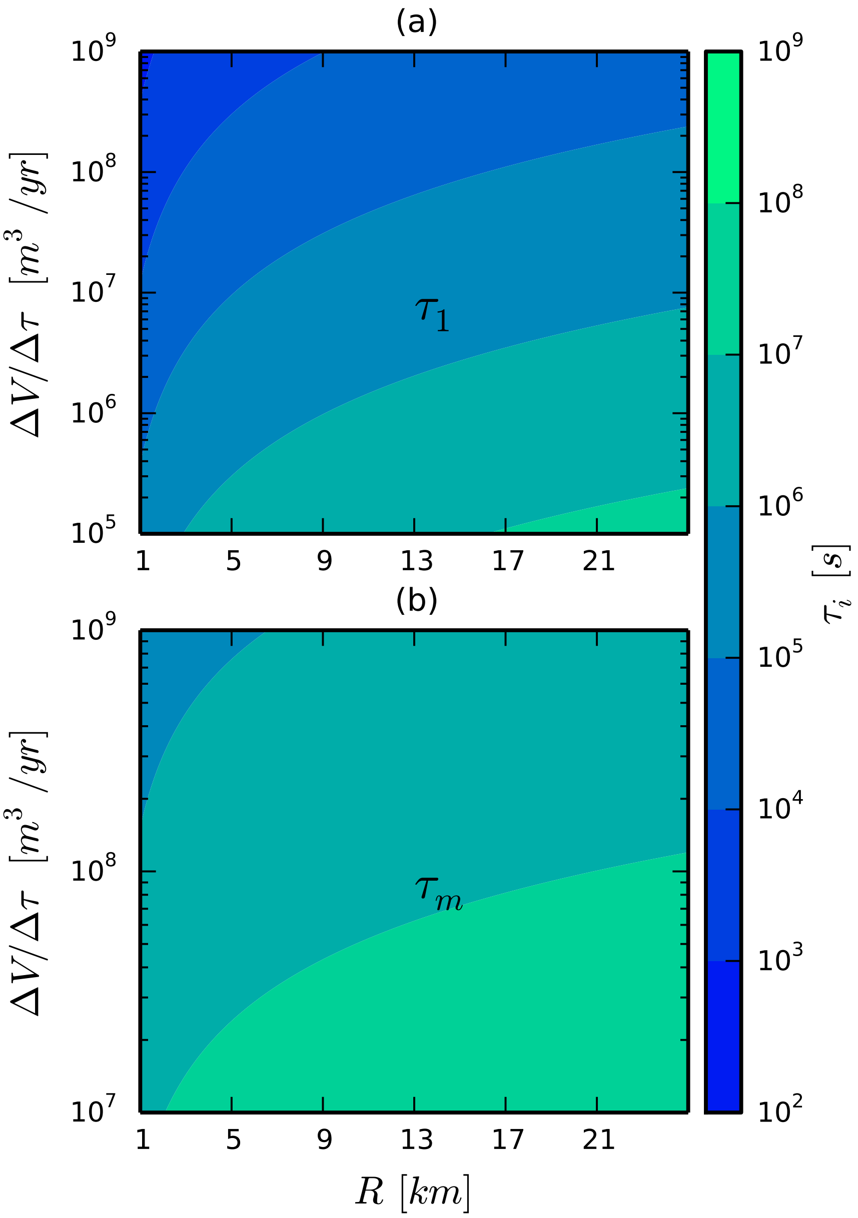

Figure 4.4: Integration times for future clocks. Analogous to Fig. 4.3, the integration times to resolve uplift and mass redistribution are shown for future clocks with $\sigma_0 = 1 \times 10^{-17}$.

where μ is the shear modulus, having the same units as pressure (note that some authors use G for the shear modulus). Typical values for rock are $\mu = 10 \times 10^9$ Pa to 30×10^9 Pa. Thus, the volume changes by

$$\Delta V = \frac{4\pi}{3}(a+\Delta a)^3 - \frac{4\pi}{3}a^3 = 4\pi a^2 \Delta a + \mathcal{O}(\Delta a^2). \tag{4.9}$$

Neglecting terms of order $\mathcal{O}(\Delta a^2)$, it can be written as

$$\Delta V = \frac{\pi a^3 \Delta P}{\mu} = \frac{3V\Delta P}{4\mu}. \tag{4.10}$$

The change in pressure within the cavity induces a volume change that affects the surrounding elastic medium. An observer on the surface at $(r, z=0)$ is displaced by

$$\begin{pmatrix} u \\ w \end{pmatrix} = a^3 \Delta P \frac{1-\nu}{\mu} \begin{pmatrix} r \\ -d \end{pmatrix} / R^3 = (1-\nu)\frac{\Delta V}{\pi} \begin{pmatrix} r \\ -d \end{pmatrix} / R^3, \tag{4.11}$$

with ν being the Poisson ratio and $R \equiv \sqrt{r^2+d^2}$ being the distance between the cavity and the observer. Thus, a point on the surface that was originally at $(r, 0)$ gets shifted to $(r+u, w)$. Therefore, an observer on the Earth surface is vertically uplifted by

$$|w(r)| = (1-\nu)\frac{\Delta V}{\pi}\frac{d}{(r^2+d^2)^{3/2}}. \tag{4.12}$$

In addition, the density of the elastic body changes at each point by [97]

$$\begin{aligned} \Delta\rho(r,z) &= \frac{\rho a^3 \Delta P}{\lambda+\mu}\frac{r^2 - 2(z+d)^2}{[r^2+(z+d)^2]^{5/2}} \\ &= (1-2\nu)\rho\frac{\Delta V}{\pi}\frac{r^2-2(z+d)^2}{[r^2+(z+d)^2]^{5/2}}, \end{aligned} \tag{4.13}$$

where λ is Lamé's constant

$$\lambda \equiv \frac{2\mu\nu}{1-2\nu} \overset{\nu=\frac{1}{4}}{=} \mu. \tag{4.14}$$

Below, we calculate the changes in the clock and gravimeter measurements due to ground displacement and the three effects coming from mass redistribution. Summing the results obtained below we find

$$\Delta U_{\mathrm{m}} \equiv \Delta U_2 + \Delta U_3 + \Delta U_4 = -G\rho_m \Delta V \frac{1}{\sqrt{r^2+d^2}}. \tag{4.15}$$

The required integration timescales to resolve uplift (τ_1) and mass redistribution (τ_m) as a function of the distance to the magma chamber and the volume change rate $\Delta V/\Delta\tau$ is given by Eq. (13) and (14), respectively. For a current clock with $\sigma_0 = 3 \times 10^{-16}$, the respective integration times are shown in Fig. 4.3(a) and (b). Resolving ΔU_{m} requires either long integration timescales of the order of a year or more or better clocks. However, for different geometries (e.g. flatter magma chambers) or more realistic models the mass redistribution term could be more significant. For future clocks with $\sigma_0 = 1 \times 10^{-17}$, the analogous plot is given in Fig. 4.4.

Ground displacement: Treating the Earth as a perfect sphere, its gravitational potential is

$$U(r,z) = -\frac{GM_\oplus}{\sqrt{r^2 + (R_\oplus - z)^2}}, \tag{4.16}$$

where $M_\oplus$ is the mass and $R_\oplus$ is the radius of the Earth.

We expand the potential in a Taylor series around $(r,z) = (0,0)$ and neglect all terms of order $\mathcal{O}(r^3), \mathcal{O}(z^3)$ and higher to obtain

$$U(r,z) \approx -\frac{GM_\oplus}{R_\oplus} - \frac{GM_\oplus}{R_\oplus^2} z + \frac{GM_\oplus}{2R_\oplus^3}(r^2 - 2z^2) \tag{4.17}$$

The gravitational acceleration is given by

$$g(r,z) = \frac{GM_\oplus}{r^2 + (R_\oplus - z)^2}, \tag{4.18}$$

with the expansion

$$g(r,z) \approx \frac{GM_\oplus}{R_\oplus^2} + \frac{2GM_\oplus}{R_\oplus^3} z - \frac{GM_\oplus}{R_\oplus^4}(r^2 - 3z^2)\ . \tag{4.19}$$

The linear term in the expansion is known as the free-air correction; we can neglect the higher orders. We define the gravitational acceleration at the surface as $g \equiv GM_\oplus/R_\oplus^2 \approx 9.81\mathrm{m/sec}^2$. For a Mogi source $z = w$ (see Eq. 4.11). The potential and gravity changes are

$$\Delta U_1 = -g\, z = g(1-\nu)\frac{\Delta V}{\pi}\frac{d}{(r^2 + d^2)^{3/2}}, \tag{4.20}$$

$$\Delta g_1 = 2g\frac{z}{R_\oplus} = -2g(1-\nu)\frac{\Delta V}{\pi\, R_\oplus}\frac{d}{(r^2 + d^2)^{3/2}}\ . \tag{4.21}$$

Direct signal: If there is inflow or outflow of magma, crustal rock of the volume ΔV will be replaced by magma, or vice versa. This change in density gives a direct signal, due to the mass change $\Delta M = \Delta V(\rho_m - \rho)$, where ρ_m and ρ are the densities of magma and crustal rock, respectively. The resulting change in the gravitational potential from the presence of the density anomaly only is

$$\Delta U_2 = -\frac{G\Delta M}{R} = -G(\rho_m - \rho)\Delta V \frac{1}{\sqrt{d^2 + r^2}}, \tag{4.22}$$

and the change in the gravitational acceleration is

$$\Delta g_2 = \frac{\partial \Delta U_2}{\partial d} = G(\rho_m - \rho)\Delta V \frac{d}{(d^2 + r^2)^{3/2}}. \tag{4.23}$$

The potential of the uplifted rock: Before the inflation of the cavity, the surface of the half-space is flat. But after the inflation there will be a hat of material peaking above the location of the cavity; this is where the clock and the gravimeter are located. Obviously, this hat of material affects the outcome of a measurement. As a simplification, most authors replace the hat by an infinite disc of height d_0. While this gives the correct first order result for the gravitational acceleration, the expression for the gravitational potential diverges.

In this section we discuss the gravitational potential and acceleration of this additional hat without making the disc approximation. This allows us to calculate the effect on clock measurements and to compute higher order corrections to the gravitational acceleration.

We denote the uplift directly above the cavity by

$$d_0 \equiv |w(r=0)| = (1-\nu)\frac{\Delta V}{\pi}\frac{1}{d^2}\ . \tag{4.24}$$

We shift the coordinates slightly to put the observer at $z=0$. Thus, $z=d_0$ now corresponds to the surface of the ground before the uplift. The z coordinate of the new surface at a given distance r is

$$\begin{aligned} z(r) &= d_0 - |w(r)| \\ &= d_0\left[1-\left(\frac{r^2}{d^2}+1\right)^{-3/2}\right]. \end{aligned} \tag{4.25}$$

This can be inverted to express r as a function of z:

$$\left(\frac{r_z}{d}\right)^2 = \left(1-\frac{z}{d_0}\right)^{-2/3} - 1. \tag{4.26}$$

The z index is used to emphasize that r_z is the distance at which the surface has altitude z.

In general, the gravitational acceleration and the gravitational potential of an observer located at $(r,z)=(0,0)$ due to the density distribution $\rho(r,z)$ are

$$g_3 = 2\pi G\int_{-\infty}^{\infty}\int_0^{\infty}\frac{\rho(r,z)z}{(r^2+z^2)^{3/2}}r\,dr\,dz, \tag{4.27}$$

$$U_3 = -2\pi G\int_{-\infty}^{\infty}\int_0^{\infty}\frac{\rho(r,z)}{\sqrt{r^2+z^2}}r\,dr\,dz. \tag{4.28}$$

Assuming constant density, the acceleration Δg_3 and the potential ΔU_3 due the uplifted mass are

$$\Delta g_3 = 2\pi G\rho\int_0^{d_0}\int_0^{r_z}\frac{rz}{(r^2+z^2)^{3/2}}dr\,dz, \tag{4.29}$$

$$\Delta U_3 = -2\pi G\rho\int_0^{d_0}\int_0^{r_z}\frac{r}{\sqrt{r^2+z^2}}dr\,dz. \tag{4.30}$$

Performing the integrals over r yields

$$\Delta g_3 = -2\pi G\rho\int_0^{d_0}\left(\frac{z}{\sqrt{r_z^2+z^2}}-1\right)dz, \tag{4.31}$$

$$\Delta U_3 = -2\pi G\rho\int_0^{d_0}\left(\sqrt{r_z^2+z^2}-z\right)dz, \tag{4.32}$$

and defining a new variable $\zeta \equiv z/d_0$, we obtain

$$\begin{aligned} \Delta g_3 &= -2\pi G\rho d_0\int_0^1\left(\frac{\zeta}{\sqrt{\frac{r_z^2}{d_0^2}+\zeta^2}}-1\right)d\zeta \\ &= -2\pi G\rho d_0\int_0^1\left(\frac{d_0}{d}\frac{\zeta}{\sqrt{(1-\zeta)^{-2/3}+\frac{d_0^2}{d^2}\zeta^2-1}}-1\right)d\zeta, \end{aligned} \tag{4.33}$$

$$\begin{aligned} \Delta U_3 &= -2\pi G\rho\int_0^{d_0}\left(\sqrt{r_z^2+z^2}-z\right)dz \\ &= -2\pi G\rho d_0 d\int_0^{d_0}\left(\sqrt{(1-\zeta)^{-2/3}+\frac{d_0^2}{d^2}\zeta^2-1}-\frac{d_0}{d}\zeta\right)d\zeta. \end{aligned} \tag{4.34}$$

Because $d_0/d \ll 1$, we can expand around $d_0/d = 0$ and drop all terms that are of order $\mathcal{O}(d_0^2/d^2)$, then we can integrate and find

$$\begin{aligned} \Delta g_3 &\approx 2\pi G\rho d_0 \left[1 - \left(2 - \frac{15\pi}{32}\right)\frac{d_0}{d}\right], \\ \Delta U_3 &\approx -2\pi G\rho d_0 d \left[1 - \frac{1}{2}\frac{d_0}{d}\right]. \end{aligned} \tag{4.35}$$

To combine this with the other mass redistribution terms, we need the result as a function of r. In the infinite disk model in the literature, the gravitational acceleration at r is taken to be that produced by a disk with a thickness equal to $|w(r)|$, the local value of the uplift,

$$\begin{aligned} \Delta g_3 &= 2\pi G\rho |w(r)| \\ &= 2G\rho(1-\nu)\Delta V \frac{d}{(r^2+d^2)^{3/2}}. \end{aligned} \tag{4.36}$$

Integrating with respect to d we obtain the corresponding potential

$$\Delta U_3 = -2G\rho(1-\nu)\Delta V \frac{1}{\sqrt{r^2+d^2}}. \tag{4.37}$$

Gravitational potential due to density change: In response to the inflating magma chamber, the density throughout the surrounding rock changes by $\Delta\rho(r,z)$, given by (4.13). The resulting change in the gravitational acceleration

$$\Delta g_4(r) = -G(1-2\nu)\rho\Delta V \frac{d}{(r^2+d^2)^{3/2}}. \tag{4.38}$$

was calculated by [97]. Following a similar approach, we determine the change in the gravitational potential due to this density variation. This may be useful for the reader since Hagiwara's paper was written in Japanese.

First, a new function K is defined

$$K(x,y,z) = \left(x^2 + y^2 + (z+d)^2\right)^{-3/2}, \tag{4.39}$$

which allows to rewrite the density change (4.13) as

$$\Delta\rho(x,y,z) = (1-2\nu)\rho\frac{\Delta V}{\pi}\left[K(x,y,z) + (z+d)\frac{\partial K(x,y,z)}{\partial d}\right]. \tag{4.40}$$

The gravitational potential due to this change in density is

$$\begin{aligned} \Delta U_4(x,y,z) &= -\int_{\mathbb{R}^3} \frac{G\Delta\rho(x',y',z')dx'\,dy'\,dz'}{\sqrt{(x-x')^2+(y-y')^2+(z-z')^2}} \\ &= \kappa \int_{\mathbb{R}} \left[1 + (z'+d)\frac{\partial}{\partial d}\right]\Phi_K(x,y,z,z')dz', \end{aligned} \tag{4.41}$$

where we defined

$$\Phi_K(x,y,z,z') \equiv \int_{\mathbb{R}^2} \frac{K(x',y',z')dx'\,dy'}{\sqrt{(x-x')^2+(y-y')^2+(z-z')^2}}, \tag{4.42}$$

$$\kappa \equiv -G(1-2\nu)\rho\frac{\Delta V}{\pi}. \tag{4.43}$$

Further, we assume that before the inflation of the magma chamber the density ρ is constant.

The 2D Fourier transform, assuming $z = 0$, is

$$\begin{aligned}\Phi_K^*(k_x, k_y) &= \frac{1}{2\pi}\int_{\mathbb{R}^2} \Phi_K(x, y, 0, z')e^{-i(k_x x+k_y y)}dx\,dy \\ &= \left[\int_{\mathbb{R}^2} K(x', y', z')e^{-i(k_x x'+k_y y')}dx'\,dy'\right] \\ &\quad\times\left[\frac{1}{2\pi}\int_{\mathbb{R}^2} \frac{e^{-i(k_x u+k_y v)}}{\sqrt{u^2+v^2+z'^2}}du\,dv\right] \\ &= 2\pi\frac{e^{-|z'+d|\sqrt{k_x^2+k_y^2}}}{z'+d}\frac{e^{-|z'|\sqrt{k_x^2+k_y^2}}}{\sqrt{k_x^2+k_y^2}} \\ &= 2\pi\frac{e^{-(2z'+d)\sqrt{k_x^2+k_y^2}}}{(z'+d)\sqrt{k_x^2+k_y^2}}.\end{aligned} \tag{4.44}$$

We substituted $u = x - x'$ and $v = y - y'$ and used $dx\,dy\,dx'\,dy' = du\,dv\,dx'\,dy'$. Further, we used the Fourier integrals

$$\frac{1}{2\pi}\int_{\mathbb{R}^2}\frac{e^{-i(k_x x+k_y y)}}{(x^2+y^2+z^2)^{1/2}}dx\,dy = \frac{e^{-|z|\sqrt{k_x^2+k_y^2}}}{\sqrt{k_x^2+k_y^2}}, \tag{4.45}$$

$$\frac{1}{2\pi}\int_{\mathbb{R}^2}\frac{e^{-i(k_x x+k_y y)}}{(x^2+y^2+z^2)^{3/2}}dx\,dy = \frac{e^{-|z|\sqrt{k_x^2+k_y^2}}}{z}, \tag{4.46}$$

and we used that the density vanishes for $z' < 0$. Taking the Fourier transform of ΔU_4

$$\begin{aligned}\Delta U_4^*(k_x, k_y) &= \frac{1}{2\pi}\int_{\mathbb{R}^2}\Delta U_4(x, y)e^{-i(k_x x+k_y y)}dx\,dy \\ &= \kappa\int_{\mathbb{R}}\left[1+(z'+d)\frac{\partial}{\partial d}\right] \\ &\quad\times\left(\frac{1}{2\pi}\int_{\mathbb{R}^2}\Phi_K(x, y)e^{-i(k_x x+k_y y)}dx\,dy\right)dz' \\ &= \kappa\int_{\mathbb{R}}\left[1+(z'+d)\frac{\partial}{\partial d}\right]\Phi_K^*(k_x, k_y)dz',\end{aligned} \tag{4.47}$$

and using the expression for Φ_K^* above, we obtain

$$\begin{aligned}\Delta U_4^*(k_x, k_y) &= 2\pi\kappa\int_{\mathbb{R}}\left[1+(z'+d)\frac{\partial}{\partial d}\right]\frac{e^{-(2z'+d)\sqrt{k_x^2+k_y^2}}}{(z'+d)\sqrt{k_x^2+k_y^2}}dz' \\ &= -2\pi\kappa\int_0^\infty e^{-(2z'+d)\sqrt{k_x^2+k_y^2}}dz' \\ &= -\pi\kappa\frac{e^{-d\sqrt{k_x^2+k_y^2}}}{\sqrt{k_x^2+k_y^2}},\end{aligned} \tag{4.48}$$

where we used that outside the half-space (i.e., for $z' < 0$) the density (contained in κ) vanishes. The inverse Fourier transform is

$$\begin{aligned}\Delta U_4(x, y) &= \frac{1}{2\pi}\int_{\mathbb{R}^2}\Delta U_4^*(k_x, k_y)e^{i(k_x x+k_y y)}dk_x dk_y \\ &= -\frac{1}{2}\kappa\int_{\mathbb{R}^2}\frac{e^{-d\sqrt{k_x^2+k_y^2}}}{\sqrt{k_x^2+k_y^2}}e^{i(k_x x+ky_y)}dk_x dk_y,\end{aligned} \tag{4.49}$$

and introducing polar coordinates $k_x = k\cos\theta, k_y = k\sin\theta$ (such that $dk_x dk_y = k\,dk\,d\theta$) and orientating the coordinate axes such that $(x, y) = (r, 0)$, the integral can be written as

$$\begin{aligned}\Delta U_4(x,y) &= -\frac{1}{2}\kappa\int_0^\infty\int_0^{2\pi}\frac{e^{-dk}}{k}e^{ikr\cos\theta}k\,d\theta\,dk\\ &= -\frac{1}{2}\kappa\int_0^\infty e^{-dk}\left(\int_0^{2\pi}e^{ikr\cos\theta}\,d\theta\right)dk\\ &= -\kappa\frac{\pi}{\sqrt{r^2+d^2}}.\end{aligned} \tag{4.50}$$

Here, we used the definition of the Bessel functions and the integral 6.751(3) in [98]. Finally, we find

$$\Delta U_4(r) = G(1-2\nu)\rho\Delta V\frac{1}{\sqrt{r^2+d^2}}. \tag{4.51}$$

Optimizing the placement of a second clock: We now consider the question of the optimal location for measuring the depth and volume change of a magma chamber. We will assume that one clock is directly over the magma chamber. What is the optimal location of a second clock? Recall that there must also be a distant reference clock. For this example, we assume that the horizontal location of the magma chamber is known from a previous survey. If this were not known, it could also be measured, but more clock locations would be required.

The shift in the gravitational potential at clock i can be written

$$\Delta U_i(r) = C_0\Delta V\frac{d}{(r_i^2+d^2)^{3/2}}\ , \tag{4.52}$$

$$C_0 \equiv \frac{GM_\oplus}{R_\oplus^2}\frac{1-\nu}{\pi}, \tag{4.53}$$

where d is the depth of the magma chamber, r_i the horizontal distance of clock i from the magma chamber. We assume that ν is known, thus C_0 is a constant.

We measure two quantities, the differences between each of the clocks and the reference clock. These are

$$\Delta U_1 = C_0\Delta V\frac{1}{d^2}, \tag{4.54}$$

$$\Delta U_2 = C_0\Delta V\frac{d}{(r^2+d^2)^{3/2}}\ . \tag{4.55}$$

The measurements of each of these quantities is affected by clock noise. The three clocks will have uncorrelated noise, but the ΔU_i will be correlated because they each depend on the reference clock. We write the variance of the two clocks near the magma chamber as σ_M^2, and the variance of the reference clock as σ_R^2. Then the variances and covariance of ΔU_1 and ΔU_2 are

$$\mathrm{Var}(\Delta U_1) = \sigma_M^2 + \sigma_R^2, \tag{4.56}$$

$$\mathrm{Var}(\Delta U_2) = \sigma_M^2 + \sigma_R^2, \tag{4.57}$$

$$\mathrm{Cov}(\Delta U_1, \Delta U_2) = \sigma_R^2\ . \tag{4.58}$$

The noise variance in the measurement of d is

$$\begin{aligned}\mathrm{Var}(d) = &\left(\frac{\partial d}{\partial\Delta U_1}\right)^2\mathrm{Var}(\Delta U_1) + \left(\frac{\partial d}{\partial\Delta U_2}\right)^2\mathrm{Var}(\Delta U_2)\\ &+2\frac{\partial d}{\partial\Delta U_1}\frac{\partial d}{\partial\Delta U_2}\mathrm{Cov}(\Delta U_1,\Delta U_2)\end{aligned} \tag{4.59}$$

and the same holds replacing d with ΔV. It is easiest to calculate the partial derivatives by calculating first the partial derivatives of the ΔU_i with respect to d and α, and inverting. They are

$$\frac{\partial \Delta V}{\partial \Delta U_1} = \frac{d^2(r^2-2d^2)}{3C_0\, r^2}, \tag{4.60}$$

$$\frac{\partial \Delta V}{\partial \Delta U_2} = \frac{2(r^2+d^2)^{5/2}}{3C_0 d\, r^2}, \tag{4.61}$$

$$\frac{\partial d}{\partial \Delta U_1} = -\frac{d^3(r^2+d^2)}{3C_0 \Delta V\, r^2}, \tag{4.62}$$

$$\frac{\partial d}{\partial \Delta U_2} = \frac{(r^2+d^2)^{5/2}}{3C_0 \Delta V\, r^2}\ . \tag{4.63}$$

We find the optimal location for the second clock by minimizing the variance of either ΔV or d, as a function of r, the horizontal distance to the second clock. Fortunately, we find that d and ΔV are optimized for similar values of r, and the minima are fairly broad. A reasonable compromise, in the case where the reference clock has the same performance as the other clocks, is $r \approx 0.78\, d$. With this clock placement, we have

$$\mathrm{Var}(\Delta V) \approx \left(4.6\, \frac{d^2}{C_0}\right)^2 \sigma_M^2, \tag{4.64}$$

$$\mathrm{Var}(d) \approx \left(2.2\, \frac{d^3}{C_0 \Delta V}\right)^2 \sigma_M^2. \tag{4.65}$$

We can summarize this more succinctly in terms of fractional errors. We define $\delta h \equiv \sigma_M/g$, which is the standard deviation of the measurement of a single clock, in terms of equivalent height. The maximum value of the uplift (at the summit) is $h = C_0\Delta V/(gd^2)$. The standard deviation of one clock is then $\sigma_M = (C_0\Delta V/d^2)\delta h/h$. Given this, the fractional accuracies of our measurements are

$$\frac{\delta \Delta V}{\Delta V} \approx 4.6\, \frac{\delta h}{h}, \tag{4.66}$$

$$\frac{\delta d}{d} \approx 2.2\, \frac{\delta h}{h}. \tag{4.67}$$

A frequency stability of 10^{-18} corresponds to 1 cm, which is achieved with current clocks after an integration of 7 hours. If each clock has this performance and the maximum uplift is 10 cm, this is a fractional accuracy of 10%, giving a fractional accuracy on d of 22% and on ΔV of 46%. If instead, we integrate for a month, the fractional accuracies improve by an order of magnitude leading to fractional accuracies of 2.2% and 4.6%, respectively.

In the case of a reference clock that is much better than the others ($\sigma_R \ll \sigma_M$), the numbers become $r \approx 0.87d$, $\delta\Delta V/\Delta V \approx 3.7\, \delta h/h$, and $\delta d/d \approx 2.0\, \delta h/h$.

4.1.4.2 Apply Mogi model to volcano

Clocks and gravimeters lying above the magma chamber will be affected by (1) a ground displacement, (2) the change of mass density within the chamber, (3) the uplifted rock, and (4) the change in the density of the surrounding material. We refer to effects (2), (3) and (4) as 'mass redistribution' (ΔU_2, ΔU_3 and ΔU_4 in above). The change of the gravitational potential due to ground displacement (1) arises since the observer is shifted to a position farther away from the centre of the Earth. A Mogi source centred at $(0, d)$ that undergoes a volume change ΔV deforms the half-space, lifting an observer sitting at $(r, 0)$ by

$$|w| = (1-\nu)\frac{\Delta V}{\pi}\frac{d}{(r^2+d^2)^{3/2}}, \tag{4.68}$$

where ν is Poisson's ratio. For crustal rock the typical value is $\nu \approx 0.25$. Using Eq. (4.3) with $z = w$, this uplift changes the potential by

$$\Delta U_1 \approx -\frac{GM_\oplus}{R_\oplus^2}w = \frac{GM_\oplus}{R_\oplus^2}(1-\nu)\frac{\Delta V}{\pi}\frac{d}{(r^2+d^2)^{3/2}}, \tag{4.69}$$

where higher order terms have been neglected. When we add the contribution of the mass redistribution terms

$$\Delta U_\mathrm{m} = G\rho_m \Delta V \frac{1}{\sqrt{r^2+d^2}}. \tag{4.70}$$

The total geopotential change is

$$\begin{aligned} \Delta U &= \Delta U_1 + \Delta U_\mathrm{m} \\ &= \frac{GM_\oplus}{R_\oplus^2}(1-\nu)\frac{\Delta V}{\pi}\frac{d}{(r^2+d^2)^{3/2}} + G\rho_m\Delta V\frac{1}{\sqrt{r^2+d^2}}, \end{aligned} \tag{4.71}$$

where ρ_m is the magma density. Typically, the change due to mass redistribuiton ΔU_m is several orders of magnitude smaller than that due to uplift ΔU_1. Measuring the mass redistribution term would require that we subtract the uplift term which may be obtained individually using other techniques like GPS or InSAR.

Similarly, the change in the gravitational acceleration is given by

$$\begin{aligned} \Delta g &= \Delta g_1 + \Delta g_m \\ &= \left[-\frac{2GM_\oplus}{R_\oplus^3}\frac{1-\nu}{\pi} + G\rho_m\right]\Delta V\frac{d}{(r^2+d^2)^{3/2}}. \end{aligned} \tag{4.72}$$

Notice that for both the acceleration and the potential the different terms of (2), (3) and (4) mostly cancel each other and only a term $\sim \rho_m$ survives (see Sec. 4.1.4.1). However, this cancellation is a consequence of the elastic half-space assumption of the Mogi model and will be less exact in more realistic scenarios. On the one hand, for the acceleration all terms have the same spatial dependence. On the other hand, for the potential they scale differently: while the uplift term scales as d/R^3 like all acceleration terms, the mass redistribution term scales as $1/R$, where $R = \sqrt{r^2+d^2}$ is the distance to the source.

Assuming a clock with stability $\Delta f/f = \sigma_0/\sqrt{\tau/\mathrm{sec}}$ and a source with a constant volume change rate $\Delta V/\Delta\tau$, the minimum required integration time to measure the uplift at a location (r, d)

$$\tau_1 = \left[\frac{\sigma_0\pi c^2}{g(1-\nu)}\frac{R^3}{d}\left(\frac{\Delta V}{\Delta\tau}\right)^{-1}\mathrm{sec}^{-1}\right]^{2/3}\mathrm{sec}, \tag{4.73}$$

with $g = GM_\oplus/R_\oplus^2$, whereas for the mass redistribution

$$\tau_m = \left[\frac{\sigma_0 R c^2}{G\rho_m}\left(\frac{\Delta V}{\Delta\tau}\right)^{-1}\mathrm{sec}^{-1}\right]^{2/3}\mathrm{sec}. \tag{4.74}$$

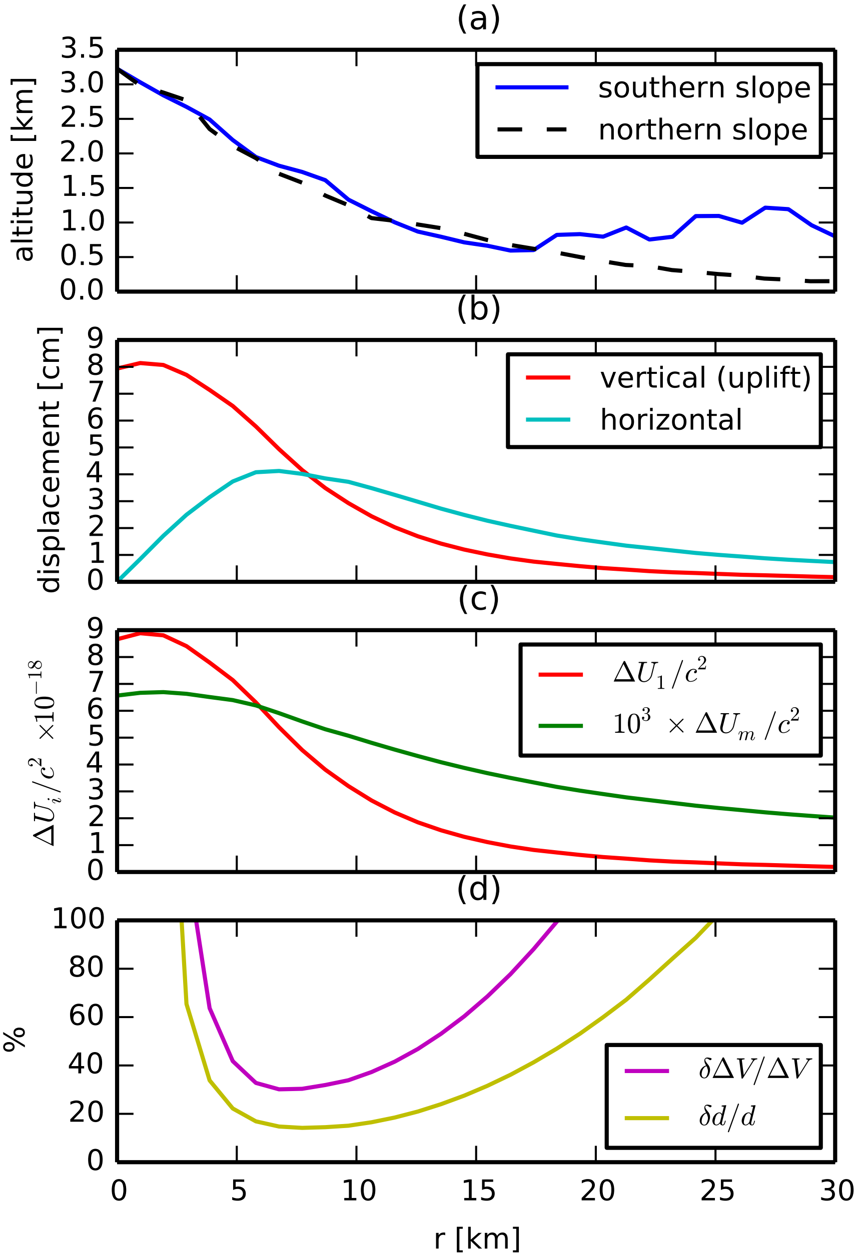

Figure 4.5: Estimate of vertical ground deformation on the Etna volcano over the course of one year with the Mogi model. In (a), the altitude profile of Etna is shown. The solid curve shows the southern slope of the mountain, the dashed line shows the mirror image of the northern slope. For the following plots only the former is considered since the latter gives very similar results. Assuming a Mogi source located 9.5 km below the summit with a volume change rate of $30 \times 10^6 \mathrm{m}^3/\mathrm{yr}$, the vertical and horizontal motion over one year is plotted in (b). The change in the gravitational potential due to this uplift together with the change due to mass redistribution is shown in (c). Notice that the latter is about 3 orders of magnitude smaller. If one clock is positioned at the summit, (d) shows the fractional errors on the measurements of the source depth $\delta d/d$ and the volume change $\delta \Delta V/V$ as a function of the horizontal distance to a second clock.

We focus on the specific example of the Etna volcano. Houlié *et al.* [94] used GPS data to investigate its underground magma system and found that a Mogi source located about 9.5 km below the summit with a volume change rate of 30×10^6 m^3/yr would yield the observed uplift. In Fig. 4.5, we plot the ground motion and the resulting potential change as well as the potential change due to mass redistribution. We find that $\Delta U_m \sim 10^{-3} \Delta U_1$, which roughly corresponds to $\Delta f/f \sim \Delta U/c^2 \sim 10^{-20}$. If we assume constant volume change rate, an optical clock on the summit would see the uplift if integrated for about ten days (Eq. (4.73)), while the mass redistribution signal is out of reach. With a clock stability σ_{tomorrow}, such an uplift would be observable within a day, and the mass redistribution in five months.

We also give an example of how to best choose the clock locations. We assume that the horizontal position of the magma chamber is already known from previous surveys, and that the two measurements we wish to make are the depth of the magma chamber d and the volume change ΔV (assuming also that ν is known). With one clock directly above the magma chamber, we find the location of a second clock which minimizes the measurement errors on d and ΔV; of course there must also be a distant reference clock. For a flat half-space we find the optimal location to be at a horizontal distance $r \approx 0.78d$ (note that the minima is broad; see Sec. 4.1.4.1). Assuming Etna to be a half-space with chamber depth 9.5 km, the fractional errors there are $\delta d/d \approx 18\%$ and $\delta\Delta V/\Delta V \approx 38\%$. Including the height profile of the mountain, Fig. 4.5(d) shows $\delta d/d$ and $\delta\Delta V/\Delta V$ as a function of the distance to the summit, assuming a clock sensitive to $\Delta U/c^2 = 10^{-18}$. We find that the optimal location of a second clock is $r \approx 0.78\,d$, independent of the clock's performance. For the performance considered here, this corresponds to $\delta d/d \approx 14\%$ and $\delta\Delta V/\Delta V \approx 30\%$.

4.1.4.3 Solid Earth tides

Solid Earth tides are the deformation of the Earth by the gravitational fields of external bodies, chiefly the Moon and the Sun. In general relativity the Earth is freely falling, so at the centre of the Earth the external gravitational force is canceled by the Earth's acceleration toward the external body. Because the external field is not uniform, other points experience a position-dependent tidal force [89].

The tide has three effects of concern on the gravitational potential. First is the external potential itself, which can be calculated directly from the known mass and position of the external bodies. Second is the change in the Earth's gravitational potential produced by the deformation of the Earth. Third is the vertical displacement of the surface, which produces a free-air correction to our measurements. The last two effects are proportional to the first, parametrized by the Love numbers k_n and h_n, respectively [89].

Throughout this section we follow [89] and we use standard spherical coordinates. The gravitational potential of an external body can be written as a multipole expansion

$$\begin{aligned} U_{\text{ext}} &= -\frac{GM_{\text{ext}}}{\rho} \\ &= -\frac{GM_{\text{ext}}}{R} \sum_{n=0}^{\infty} \left(\frac{r}{R}\right)^n P_n(\cos\alpha). \end{aligned} \tag{4.75}$$

Here, ρ is the distance between the external body and the location of the clock, R is the distance between the body and the Earth's centre of mass, r is the distance between the Earth's centre and the clock and α is the angle between the two vectors pointing from the centre of the Earth to the external mass and the clock. The P_n denote the Legendre polynomials. In the sum, the $n = 0$ term can be neglected since it is constant and therefore does not contribute to the force since it will drop out when taking the gradient. The $n = 1$ term ($U_{\text{ext,n=1}} = -GM_{\text{ext}}/R^2 r\cos\alpha$) causes the orbital acceleration and therefore, by the definition of tides, the tidal potential is

$$U_{\text{tid}}(r,\alpha) = -\frac{GM_{\text{ext}}}{R}\sum_{n=2}^{\infty}\left(\frac{r}{R}\right)^n P_n(\cos\alpha). \tag{4.76}$$

By U^n_{tid} we will denote the n-th order component of the expansion.

The tidal deformation is mainly caused by the Moon and the Sun; the other planets cause very minor effects. Since typically r/R is small (for the Moon: $r/R \approx 1/60$, Sun: $r/R \approx 1/23000$), it is sufficient to just consider the first few orders of the expansion.

If the Earth was a completely rigid spherical body with no external mass acting tidally, the gravitational acceleration at the surface would be a constant $g \equiv GM_\oplus/R^2_\oplus$. Changing the radial distance by a small amount Δr would change g by $\Delta g = -2GM_\oplus/R^3_\oplus\Delta r$. Thus, going farther away ($\Delta r > 0$) weakens the gravitational acceleration.

First, we consider just the effect of an external body, letting the Earth be perfectly rigid. This corresponds to the Love numbers (introduced below) being zero. The value of the tidal potential on the surface is $U_{\text{tid}}(R_\oplus,\alpha)$. This induces a change in the gravitational acceleration at the surface of

$$\begin{aligned}\Delta g(\alpha) &= -\left.\frac{\partial U_{\text{tid}}(r,\alpha)}{\partial r}\right|_{r=R_\oplus} \\ &= -\sum_{n=2}^{\infty} n\frac{U^{(n)}_{\text{tid}}(R_\oplus,\alpha)}{R_\oplus}.\end{aligned} \tag{4.77}$$

Just taking the first ($n=2$) term, this is

$$\begin{aligned}\Delta g(\alpha) &= -2\frac{U^{(2)}_{\text{tid}}(R_\oplus,\alpha)}{R_\oplus} \\ &= \frac{GM_{\text{ext}}}{R^3}R_\oplus(3\cos^2\alpha - 1).\end{aligned} \tag{4.78}$$

Thus, there is an outward pull, $\Delta g > 0$, at the sides of the Earth facing ($\alpha = 0$) and opposing ($\alpha = \pi$) the external body. Halfway between, there is an inward pull ($\alpha = \pi/2, 3\pi/2$). Since the Earth is not a rigid body, it is deformed by tidal forces. Its tidal response is quantified by the Love numbers k_n and h_n; there is also a Love number l_n which we do not use here. The larger the Love numbers, the stronger the deformation.

The gravitational acceleration arising from the tidal interaction has three components. First, there is the direct effect from the external body (4.77). Second, the deformation of the Earth gives rise of an additional gravitational potential $k_n U^{(n)}_{\text{tid}}$, resulting in an additional acceleration. Third, due to the deformation, the altitude of the observer changes by $-h_n U^{(n)}_{\text{tid}}/g$ compared to a non-deformed Earth. Thus, the effective tidal potential measured by a clock on the surface, for a given n, is

$$U^{(n)}_{\text{tid,eff}} = (1 + k_n - h_n)U^{(n)}_{\text{tid}}\ . \tag{4.79}$$

The potential of the deformed Earth is $k_n U_{(n)}$. It can be written as an expansion around its value $U_{\text{tid}}(R_\oplus,\alpha)$ at the undistorted surface. Since the gravitational field satisfies Poisson's equation, it is a harmonic function outside the Earth and therefore, we can write it as an expansion of the form

$$U_{\text{Earth def}}(r,\alpha) = \sum_{n=0}^{\infty}\left(\frac{R_\oplus}{r}\right)^{n+1} F_n(\alpha), \tag{4.80}$$

where the functions $F_n(\alpha)$ have to be chosen such that they match $U_{\text{tid}}(R_\oplus, \alpha)$ at the Earth's surface, giving

$$U_{\text{Earth def}}(r,\alpha) = -\frac{GM_{\text{ext}}}{R}\sum_{n=2}^{\infty}\left(\frac{R_\oplus}{R}\right)^n\left(\frac{R_\oplus}{r}\right)^{n+1}P_n(\cos\alpha). \tag{4.81}$$

The tidal acceleration is now given by

$$\begin{aligned} &-\left.\frac{\partial(U_{\text{tid}}+k_nU_{\text{Earth def}})}{\partial r}\right|_{r=R_\oplus} \\ &= \frac{GM_{\text{ext}}}{R}\sum_{n=2}^{\infty}\frac{1}{R_\oplus}\left(n-k_n(n+1)\right)\left(\frac{R_\oplus}{R}\right)^n \\ &\quad\times P_n(\cos\alpha), \end{aligned} \tag{4.82}$$

which can be written as

$$-\sum_{n=2}^{\infty}n\left(1-\frac{n+1}{n}k_n\right)\frac{U^n_{\text{tid}}(R_\oplus,\alpha)}{R_\oplus}. \tag{4.83}$$

The change in the gravitational acceleration due to a small radial displacement Δr close to the surface of the Earth is

$$-\frac{2GM_\oplus}{R_\oplus^3}\Delta r = -2\frac{GM_\oplus}{R_\oplus^2}\frac{\Delta r}{R_\oplus} = -2g\frac{\Delta r}{R_\oplus}. \tag{4.84}$$

The final effective tidal acceleration on the surface is

$$\Delta g^{(n)}_{\text{tid,eff}} = \left(n-(n+1)k_n+2h_n\right)\frac{U^n_{\text{tid}}(R_\oplus,\alpha)}{R_\oplus}\ . \tag{4.85}$$

From (4.79) and (4.85), we see a key feature of clocks relative to gravimeters. Gravimeters are relatively more sensitive to effects at higher n, i.e., shorter wavelengths, than are clocks. This is because they measure a spatial derivative of the potential rather than the potential itself. In contrast, the response to uplift only depends on motion in the entire gravitational field of the Earth, and so the coefficients of h_n do not depend on n.

Note that clocks are best at constraining the lower order multipoles. Instruments that measure higher order derivatives of the geopotential (e.g. gradiometers) are more sensitive to the higher order multipoles. Clocks will only be useful for measuring the $n = 2$ and possibly $n = 3$ tides. However, a detailed analysis of the multipole structure based on clock data is beyond the subject of this paper.

As shown above, clocks (sensitive to geopotential changes) and gravimeters (sensitive to the downward component of g) each measure a different linear combination of the Love numbers. This is because the three effects scale differently with the distance from the centre of the Earth. It is therefore desirable to combine gravimeter and clock measurements to infer the Love numbers with great accuracy. Recall that clock measurements must be made between a pair of clocks. Since tidal effects are global, both clocks are sensitive to the tidal deformation; one clock cannot simply be treated as a reference. To measure the tidal amplitude, it is necessary to compare instruments over distances of the order of half the tidal wavelength on timescales shorter than the period of the tide. The tidal wavelength is half the circumference of the Earth for the dominant tidal mode. Both differential GPS and InSAR have short baseline, so tidal effects are small and are mostly subtracted by modelling. A network of clocks where each clock pair is separated by hundreds of kilometers could more holistically monitor solid Earth tides. Current clocks provide measurements of the vertical uplift to within a percent of the maximal tidal amplitude on an hourly basis. Such measurements could be used to monitor stress changes within the crust, and to investigate whether these correlate with triggered seismicity.

Such a network of clocks on the continent scale could accurately measure the tidal Love numbers. The external tidal potential can be decomposed into a sum of Legendre polynomials

$$U^n_{\text{tid}}(R,\alpha) = -\frac{GM_{\text{ext}}}{R}\left(\frac{R_\oplus}{R}\right)^n P_n(\cos\alpha), \tag{4.86}$$

where R is the distance between the external body of mass M_{ext} and the Earth's centre of mass, and α is the angle from the observation point to the line between the centre of the Earth and the external body. Since $R_\oplus/R \approx 1/60$ for the Moon, and $R_\oplus/R \approx 1/23000$ for the Sun, it is typically sufficient to just consider the first few terms of the expansion. By linearity, we treat each n separately.

The potential change measured by a clock, including all three effects above, is

$$\Delta U_n = (1 + k_n - h_n)U^n_{\text{tid}}(R,\alpha)\ . \tag{4.87}$$

The change in the vertical gravitational acceleration measured by a gravimeter is

$$\Delta g_n = -n\left(1 - \frac{n+1}{n}k_n + \frac{2}{n}h_n\right)\frac{U^n_{\text{tid}}(R,\alpha)}{R_\oplus}\ . \tag{4.88}$$

Combining the two measurements with the known $U^n_{\text{tid}}(R_\oplus,\alpha)$ we can determine the Love numbers

$$k_n = \frac{n+2}{n-1} + \frac{R_\oplus \Delta g_n - 2\Delta U_n}{(n-1)U^n_{\text{tid}}(R_\oplus,\alpha)}, \tag{4.89}$$

$$h_n = \frac{2n+1}{n-1} + \frac{R_\oplus \Delta g_n - (n+1)\Delta U_n}{(n-1)U^n_{\text{tid}}(R_\oplus,\alpha)}. \tag{4.90}$$

Both Love numbers are believed to be modelled to within a fraction of a percent [99]. These models will be throughly tested once a global optical clock network becomes available.

4.1.5 Conclusions

We have demonstrated the promise of very precise atomic clocks for geophysical measurements with two illustrative examples. In the inflation or deflation of a spherical magma chamber (the Mogi model) clocks are primarily sensitive to the local vertical displacement resulting at the Earth's surface. Such monitoring of local deformations can be done using a reference clock anywhere outside the zone where the displacement is significant, typically tens of kilometres. However, when monitoring solid Earth tides, the best accuracy will be obtained with a clock network spanning the globe.

Beyond the examples given, it should be possible to use clocks in conjunction with gravimeters to monitor dyke intrusion, post-seismic deformation, aquifer variations, and other effects causing vertical displacement or subsurface mass change. In contrast to GPS and InSAR measurements, ground clock measurements are insensitive to the turbulence in the atmosphere.

In the future, optical clocks are expected to become part of the global ground-clock network that is used for telecommunications increasing the precision with which we can monitor time. Ground clocks can thus be combined with existing instrumentations (GPS, InSAR, gravimeters) to track underground mass redistribution through its effects on the geopotential. Portable optical clocks have already been developed [90], and could monitor changes in the geopotential of the Earth across fault lines, in areas with active volcanoes, and for surveying.

Chapter 5

Conclusions

It is safe to say that it is a good time now to start doing research on general relativity. Over the course of my PhD, many very exciting events in the field of gravitational physics occurred. *LIGO* made the first direct detection of gravitational waves and the *LISA Pathfinder* satellite has not only been launched successfully but is also performing remarkably well. Together, they lay the cornerstone for gravitational wave astronomy in space. The *Microscope* satellite launched and is currently testing the weak equivalence principle at an unprecedented level. Furthermore, the two atomic clocks of the *Atomic Clock Ensemble in Space (ACES)* mission will launch soon.

As the title of this thesis indicates, I worked on different projects studying alternative theories of gravity, tests of theories of gravitation and applications of relativity in geophysics. In some of the projects, we tried to make connections between the different fields. Below, all the chapters are briefly summarized. Besides stating the main results, some remarks are added.

In chapter 2 we discuss **scalar-tensor and multi scalar-tensor theories**. First, we consider the case of a single scalar field where the action is given in the Einstein frame. We discuss and demonstrate the advantage of working in this frame compared to the Jordan frame. We focus on the weak field limit that can be described in the PPN framework in which we calculate the parameters γ and β. We introduce a general formalism to discuss constraints on scalar-tensor theories. Applying the Cassini constraint on γ, it can be used to constrain the $(\alpha_{\text{Sun}}, m_{\text{J}})$-parameter space, which is shown in figure 2.1. Here, we take the signal's closest distance to the Sun as the interaction distance. This constraint is specific to the Sun, since the parameter α_{Sun} will, in realistic scenarios, not only depend on parameters of the theory but also on the properties of the Sun. As an example, we calculate α for a homogeneous sphere, assuming a massive Brans-Dicke theory. It shows that in fact α depends on the size of the sphere. Figure 2.2 shows the Cassini constraint applied to this situation. This yields a more stringent constraint compared to the one obtained when considering a point source. Since α depends on properties of the central mass, experiments around different masses, say the Sun and the Earth, are complementary. Furthermore, we estimate the impact of the PPN parameters on a redshift measurement as measured by a satellite which carries a clock that is compared to ground clocks. Assuming a realistic eccentric orbit and constant PPN parameters, limits on γ and β should be achievable that are comparable to the limits obtained from the Cassini experiment or from planetary ephemerides.

Chapter 3 discusses the possibility of measuring **relativistic effects** in the Solar System by comparing a satellite clock to laboratory clocks on the Earth's surface. We developed a code to calculate those effects for terrestrial satellites and planetary missions. We find that it is desirable to have orbits with high eccentricities. This boosts relativistic effects at pericenter due to the high velocity and the relatively low altitude there. Often, physicists think of relativistic effects as continuous effects that build up slowly. For example, it is well-known that perihelion of an orbit precesses per orbit, as given by equation (3.66), which is due to Schwarzschild space curvature. However, this is the total precession averaged over one orbit. For an eccentric orbit, almost all precession is done during the pericenter passage, as can be seen in figure 3.1. This is analogous for all relativistic effects on the orbit. Studying these relativistic effects when averaged over many orbits can bring significant problems. Small relativistic effects might get masked by much larger Newtonian effects, e.g., due to multipole moments that are not well-known. Therefore, we propose to look at the redshift signal over just one pericenter passage. Each relativistic effect leaves a characteristic imprint that can, in principle, be filtered out. We discuss the different relativistic effects on the basis of proposed terrestrial missions and the currently flying planetary missions *Juno* and *Cassini*, orbiting Jupiter and Saturn, respectively. With current technology it is realistic to probe Schwarzschild curvature and first order spin, which is a frame-dragging effect. Also, the leading order relativistic effect on the signal, the Shapiro time delay, is measurable. However, with slightly improved technology also spin-square, the effects of next higher order seem to lie within reach.

We proposed a satellite project called *Einstein Gravitational Redshift Probe (E-GRIP)* in the context of a call for ideas of a mission by the Swiss Space Office. The idea of *E-GRIP* is to have a hydrogen maser atomic clock built in Switzerland on an eccentric orbit around Earth. This would allow testing aspects of the Einstein equivalence principle and relativistic effects. In addition, it would provide measurements for time and frequency metrology and geodesy. Although the mission did not get selected, we are very confident that *E-GRIP* or a similar mission will fly eventually. For me, it was a great experience to take part in the process of proposing such a mission. It was not only interesting from a scientific point of view but also to see how the organization behind such a project works.

In the **geophysics project** presented in chapter 4, we calculate the impact of an inflating or deflating magma chamber on an atomic clock that is located at the volcano above. We use the Mogi model for describing the magma chamber. Its impact on an instrument can be divided into two parts: A part solely due to uplift and another due to the redistribution of matter. We estimate the former to be larger by usually about three orders of magnitude. We find that clocks can indeed be a very interesting tool to monitor volcanoes. However, current clocks are of limited use and further improvement is necessary. Assuming a similar improvement to the one in the past years, clocks in the near future will be significantly more stable over longer periods of time as well as more portable. Such clocks could be a valuable alternative or extension to current observation techniques such as gravimeters, GPS and InSAR. For example, while clocks measure differences in the gravitational potential, gravimeters measure changes in the gravitational acceleration, which is the gradient of the potential. On the one hand, the change in potential due to uplift scales as $1/R^2$ and change due to redistribution as $1/R$. On the other hand, both contributions scale as $1/R^2$ for the gravitational accelerations. As a consequence, using both instruments together would help getting a better understanding of underground processes. Furthermore, we motivate the establishment of a global network of atomic clocks that can be used to measure the solid Earth tides.

This project was done by a collaboration of theoretical physicists and geophysicists. It was an interesting experience to work with scientists from a different field. I think that such interdisciplinary collaborations are invaluable and input from other fields can give ideas that one would not come up with when just being surrounded by people with a similar background.

5.1 Outlook

There are many interesting projects that could extend my research.

The discussion of single and multi scalar-tensor theories can be extended to more general theories. One can consider more types of coupling and also add further types of fields such as vector fields. In section 2.1 we discuss the possibility of constraining PPN parameters with satellite experiments. However, we consider the parameters to be constant. This is only a valid assumption for massless scalar fields, but if they are massive, the parameters depend on the distance from the central mass. Therefore, one could implement distance dependent PPN parameters into the code presented in section 3.

In our discussion of relativistic effects we solve the forward problem. I.e., we choose an orbit and calculate the size of the different effects on the signal. An interesting follow-up project would be to tackle the inverse problem. There, the goal would be to extract the relativistic contributions for a given redshift curve.

Appendix A

Theory of multi-scalar tensor gravity

In this appendix, some calculations that are needed in Sec. 2.2 are done in detail.

A.1 Field equations

We start with the action of a multi-scalar tensor gravitation theory, formulated in an arbitrary frame (2.75)

$$S = \frac{1}{2\kappa^2}\int d^4x\sqrt{-g}\,\Big(\mathcal{A}(\Phi)R - \mathcal{B}_{AB}(\Phi)g^{\mu\nu}\partial_\mu\Phi^A\partial_\nu\Phi^B - 2\kappa^2\mathcal{U}(\Phi)\Big) + S_m[e^{2\alpha(\Phi)}g_{\mu\nu},\chi]\,. \tag{A.1}$$

It will be useful to remember the D'Alembert operator

$$\Box\phi \equiv \nabla^2\phi \equiv \nabla^\mu\nabla_\mu\phi = \frac{1}{\sqrt{-g}}\partial_\mu\left(\sqrt{-g}\partial^\mu\phi\right). \tag{A.2}$$

A.1.1 Metric field equations

The metric field equations, which are a generalization of Einstein's equations, are derived from varying the action (A.1) w.r.t. the metric tensor. Next, we take the variation of all the terms in the metric individually. The variation of the curvature part is

$$\delta\left(\int d^4x\sqrt{-g}\mathcal{A}R\right) = \int d^4x\sqrt{-g}\,\Big[\mathcal{A}\,G_{\mu\nu} + g_{\mu\nu}\nabla^2\mathcal{A} - \nabla_\mu\nabla_\nu\mathcal{A}\Big]\,\delta g^{\mu\nu}\,, \tag{A.3}$$

and the variation of kinetic part is

$$\begin{aligned}
&\delta\left(\int d^4x\,\sqrt{-g}\mathcal{B}_{AB}g^{\mu\nu}\partial_\mu\Phi^A\partial_\nu\Phi^B\right)\\
&= \int d^4x\,\delta(\sqrt{-g}g^{\mu\nu})\mathcal{B}_{AB}\partial_\mu\Phi^A\partial_\nu\Phi^B\\
&= \int d^4x\left(-\frac{1}{2}\sqrt{-g}g_{\alpha\beta}\delta g^{\alpha\beta}g^{\mu\nu} + \sqrt{-g}\delta g^{\mu\nu}\right)\mathcal{B}_{AB}\partial_\mu\Phi^A\partial_\nu\Phi^B\\
&= \int d^4x\,\sqrt{-g}\,\mathcal{B}_{AB}\left(-\frac{1}{2}g_{\mu\nu}g^{\alpha\beta}\partial_\alpha\Phi^A\partial_\beta\Phi^B + \partial_\mu\Phi^A\partial_\nu\Phi^B\right)\delta g^{\mu\nu}\,,
\end{aligned} \tag{A.4}$$

where we used

$$\delta(\sqrt{-g}) = -\frac{1}{2}\sqrt{-g}g_{\alpha\beta}\delta g^{\alpha\beta}\,. \tag{A.5}$$

We take the variation of the potential part

$$\delta\left(\int d^4x\sqrt{-g}2\kappa^2\mathcal{U}\right) = -\int d^4x\frac{1}{2}\sqrt{-g}g_{\mu\nu}2\kappa^2\mathcal{U}\delta g^{\mu\nu}\,, \tag{A.6}$$

and, finally, the variation of the matter part

$$\begin{aligned}\delta S_m &= \delta\left(\int d^4x\sqrt{-g}\mathcal{L}\right)\\ &= \int d^4x\frac{\partial\left(\sqrt{-g}\mathcal{L}\right)}{\partial g^{\mu\nu}}\delta g^{\mu\nu}\\ &= \frac{-1}{2}\int d^4x\sqrt{-g}\left(\frac{-2}{\sqrt{-g}}\frac{\partial\left(\sqrt{-g}\mathcal{L}\right)}{\partial g^{\mu\nu}}\right)\delta g^{\mu\nu}\\ &= \int d^4x\sqrt{-g}\frac{-T_{\mu\nu}}{2}\delta g^{\mu\nu}\,.\end{aligned} \tag{A.7}$$

We defined the stress-energy tensor

$$T_{\mu\nu} \equiv \frac{-2}{\sqrt{-g}}\frac{\partial\left(\sqrt{-g}\mathcal{L}\right)}{\partial g^{\mu\nu}}\,. \tag{A.8}$$

Then, from the action principle $\delta S = 0$ the tensor field equations follow:

$$\begin{aligned}&\frac{1}{2\kappa^2}\left[\mathcal{A}\,G_{\mu\nu} + g_{\mu\nu}\nabla^2\mathcal{A} - \nabla_\mu\nabla_\nu\mathcal{A} + \frac{1}{2}g_{\mu\nu}\mathcal{B}_{AB}g^{\alpha\beta}\partial_\alpha\Phi^A\partial_\beta\Phi^B - \mathcal{B}_{AB}\partial_\mu\Phi^A\partial_\nu\Phi^B + g_{\mu\nu}\kappa^2\mathcal{U}\right]\\ &-\frac{T_{\mu\nu}}{2} = 0\end{aligned} \tag{A.9}$$

or, equivalently,

$$\mathcal{A}\,G_{\mu\nu} + g_{\mu\nu}\nabla^2\mathcal{A} - \nabla_\mu\nabla_\nu\mathcal{A} + \frac{1}{2}g_{\mu\nu}\mathcal{B}_{AB}g^{\alpha\beta}\partial_\alpha\Phi^A\partial_\beta\Phi^B - \mathcal{B}_{AB}\partial_\mu\Phi^A\partial_\nu\Phi^B + g_{\mu\nu}\kappa^2\mathcal{U} = \kappa^2T_{\mu\nu}\,. \tag{A.10}$$

We introduced the Einstein tensor $G_{\mu\nu} = R_{\mu\nu} - \frac{1}{2}g_{\mu\nu}R$. It is useful to take the trace of both sides of the equation (i.e., applying $g^{\mu\nu}$ to both sides)

$$-\mathcal{A}\,R + 3\nabla^2\mathcal{A} + \mathcal{B}_{AB}\partial_\mu\Phi^A\partial^\mu\Phi^B + 4\kappa^2\mathcal{U} = \kappa^2T\,, \tag{A.11}$$

where we made use of $G = g^{\mu\nu}G_{\mu\nu} = -R$. Using the trace of the metric field equations (A.11) together with

$$\nabla^2\mathcal{A} = \nabla^\mu\nabla_\mu\mathcal{A} = \nabla^\mu\left(\frac{\partial\mathcal{A}}{\partial\Phi^C}\nabla_\mu\Phi^C\right) = \frac{\partial\mathcal{A}}{\partial\Phi^C}\nabla^2\Phi^C + \frac{\partial^2\mathcal{A}}{\partial\Phi^D\partial\Phi^C}\partial^\mu\Phi^D\partial_\mu\Phi^C \tag{A.12}$$

allows us to express the Ricci scalar as

$$R = \frac{3}{\mathcal{A}}\frac{\partial\mathcal{A}}{\partial\Phi^A}\nabla^2\Phi^A + \frac{1}{\mathcal{A}}\left(\mathcal{B}_{AB} + 3\frac{\partial^2\mathcal{A}}{\partial\Phi^A\partial\Phi^B}\right)\partial_\mu\Phi^A\partial^\mu\Phi^B + \frac{4}{\mathcal{A}}\kappa^2\mathcal{U} - \frac{1}{\mathcal{A}}\kappa^2T\,. \tag{A.13}$$

Plugging this into Eq. (A.10) and rearranging Eq. (A.12)

$$\frac{\partial\mathcal{A}}{\partial\Phi^C}\nabla^2\Phi^C = \nabla^2\mathcal{A} - \frac{\partial^2\mathcal{A}}{\partial\Phi^D\partial\Phi^C}\partial^\mu\Phi^D\partial_\mu\Phi^C \tag{A.14}$$

gives

$$R_{\mu\nu} = \frac{1}{\mathcal{A}}\left[\kappa^2\left(T_{\mu\nu} - \frac{1}{2}g_{\mu\nu}T\right) + g_{\mu\nu}\kappa^2\mathcal{U} + \frac{1}{2}g_{\mu\nu}\nabla^2\mathcal{A} + \nabla_\mu\nabla_\nu\mathcal{A} + \mathcal{B}_{AB}\partial_\mu\Phi^A\partial_\nu\Phi^B\right]. \tag{A.15}$$

Using (A.12) and

$$\nabla_\mu\nabla_\nu\mathcal{A} = \nabla_\mu\left(\frac{\partial\mathcal{A}}{\partial\Phi^A}\nabla_\nu\Phi^A\right) = \frac{\partial^2\mathcal{A}}{\partial\Phi^A\partial\Phi^B}\nabla_\mu\Phi^A\nabla_\nu\Phi^B + \frac{\partial\mathcal{A}}{\partial\Phi^A}\nabla_\mu\nabla_\nu\Phi^A, \tag{A.16}$$

we can write the field equation (A.10) as

$$\begin{aligned}&\mathcal{A}\,G_{\mu\nu} + \frac{\partial\mathcal{A}}{\partial\Phi^A}\left(g_{\mu\nu}\nabla^2\Phi^A - \nabla_\mu\nabla_\nu\Phi^A\right) - \left(\frac{\partial^2\mathcal{A}}{\partial\Phi^A\partial\Phi^B} + \mathcal{B}_{AB}\right)\partial_\mu\Phi^A\partial_\nu\Phi^B\\ &+ g_{\mu\nu}\left(\frac{\partial^2\mathcal{A}}{\partial\Phi^A\partial\Phi^B} + \frac{1}{2}\mathcal{B}_{AB}\right)\partial^\rho\Phi^A\partial_\rho\Phi^B + g_{\mu\nu}\kappa^2\mathcal{U} = \kappa^2T_{\mu\nu}\end{aligned} \tag{A.17}$$

and the trace-reversed tensor field equation (A.15) as

$$\begin{aligned}R_{\mu\nu} = \frac{1}{\mathcal{A}}\Bigg[&\kappa^2\left(T_{\mu\nu} - \frac{1}{2}g_{\mu\nu}T\right) + \frac{\partial\mathcal{A}}{\partial\Phi^A}\left(\nabla_\mu\nabla_\nu\Phi^A + \frac{1}{2}g_{\mu\nu}\nabla^2\Phi^A\right)\\ &+ \left(\frac{\partial^2\mathcal{A}}{\partial\Phi^A\partial\Phi^B} + \mathcal{B}_{AB}\right)\partial_\mu\Phi^A\partial_\nu\Phi^B + \frac{1}{2}g_{\mu\nu}\frac{\partial^2\mathcal{A}}{\partial\Phi^A\partial\Phi^B}\partial^\rho\Phi^A\partial_\rho\Phi^B + g_{\mu\nu}\kappa^2\mathcal{U}\Bigg].\end{aligned} \tag{A.18}$$

A.1.2 Scalar field equations

The scalar field equations are obtained by taking the variation of the action A.1 w.r.t. the scalar fields. The variation of the curvature part is

$$\delta\left(\int d^4x\sqrt{-g}\mathcal{A}R\right) = \int d^4x\sqrt{-g}\delta(\mathcal{A})R = \int d^4x\sqrt{-g}\frac{\partial\mathcal{A}}{\partial\Phi^C}R\,\delta\Phi^C \tag{A.19}$$

and taking the variation of the kinetic part gives

$$\begin{aligned}&\delta\left(\int d^4x\,\sqrt{-g}\mathcal{B}_{AB}g^{\mu\nu}\partial_\mu\Phi^A\partial_\nu\Phi^B\right)\\ &= \int d^4x\,\sqrt{-g}\left(\frac{\partial\mathcal{B}_{AB}}{\partial\Phi^C}\delta\Phi^C\partial_\mu\Phi^A\partial^\mu\Phi^B + 2\mathcal{B}_{AB}\partial_\mu(\delta\Phi^A)\partial^\mu\Phi^B\right)\\ &= \int d^4x\left(\sqrt{-g}\frac{\partial\mathcal{B}_{AB}}{\partial\Phi^C}\partial_\mu\Phi^A\partial^\mu\Phi^B\delta\Phi^C - 2\partial_\mu\left(\sqrt{-g}\mathcal{B}_{AB}\partial^\mu\Phi^B\right)\delta\Phi^A\right)\\ &= \int d^4x\left(\sqrt{-g}\frac{\partial\mathcal{B}_{AB}}{\partial\Phi^C}\partial_\mu\Phi^A\partial^\mu\Phi^B\delta\Phi^C - 2\sqrt{-g}\nabla^2\Phi^B\mathcal{B}_{AB}\delta\Phi^A - 2\frac{\partial\mathcal{B}_{AB}}{\partial\Phi^C}\partial_\mu\Phi^C\sqrt{-g}\partial^\mu\Phi^B\delta\Phi^A\right)\\ &= \int d^4x\sqrt{-g}\left(\left[\frac{\partial\mathcal{B}_{AB}}{\partial\Phi^C} - 2\frac{\partial\mathcal{B}_{BC}}{\partial\Phi^A}\right]\partial_\mu\Phi^A\partial^\mu\Phi^B - 2\mathcal{B}_{AC}\nabla^2\Phi^A\right)\delta\Phi^C.\end{aligned} \tag{A.20}$$

We utilized that $\mathcal{B}_{AB}$ is symmetric, Eq. (A.2) and dropped the boundary terms when integrating by parts. The variation of the potential part is

$$\delta\left(\int d^4x\sqrt{-g}2\kappa^2\mathcal{U}\right) = \int d^4x\sqrt{-g}2\kappa^2\delta(\mathcal{U}) = \int d^4x\sqrt{-g}2\kappa^2\frac{\partial\mathcal{U}}{\partial\Phi^C}\delta\Phi^C \tag{A.21}$$

and the variation of the matter part is

$$\begin{aligned}\delta S_m &= \int d^4x\, \delta\left(\sqrt{-g}\mathcal{L}\right) \\ &= -2\int d^4x\, \frac{\partial(\sqrt{-g}\mathcal{L})}{\partial g^{\mu\nu}} g^{\mu\nu}\frac{\partial\alpha}{\partial\Phi^C}\delta\Phi^C \\ &= \int d^4x\sqrt{-g}T_{\mu\nu}g^{\mu\nu}\frac{\partial\alpha}{\partial\Phi^C}\delta\Phi^C \\ &= \int d^4x\sqrt{-g}T\frac{\partial\alpha}{\partial\Phi^C}\delta\Phi^C\,,\end{aligned} \tag{A.22}$$

where we used the trace of the stress-energy tensor

$$T = T_{\mu\nu}g^{\mu\nu}\,. \tag{A.23}$$

Then, the action principle gives the scalar field equations

$$\begin{aligned}&\frac{1}{2\kappa^2}\left[\frac{\partial\mathcal{A}}{\partial\Phi^C}R - \left(\frac{\partial\mathcal{B}_{AB}}{\partial\Phi^C} - \left(\frac{\partial\mathcal{B}_{AC}}{\partial\Phi^B} + \frac{\partial\mathcal{B}_{BC}}{\partial\Phi^A}\right)\right)\partial_\mu\Phi^A\partial^\mu\Phi^B + 2\mathcal{B}_{AC}\nabla^2\Phi^A - 2\kappa^2\frac{\partial\mathcal{U}}{\partial\Phi^C}\right] \\ &+T\frac{\partial\alpha}{\partial\Phi^C} = 0\,.\end{aligned} \tag{A.24}$$

Using Eq. (A.13), we can eliminate the Ricci scalar. By multiplying both sides with $\mathcal{A}$ and taking the D'Alembertian to the left hand side, the scalar field equations are now

$$\begin{aligned}&\left(2\mathcal{A}\mathcal{B}_{AC} + 3\frac{\partial\mathcal{A}}{\partial\Phi^C}\frac{\partial\mathcal{A}}{\partial\Phi^A}\right)\nabla^2\Phi^A \\ &= \left[\mathcal{A}\left(\frac{\partial\mathcal{B}_{AB}}{\partial\Phi^C} - \left(\frac{\partial\mathcal{B}_{AC}}{\partial\Phi^B} + \frac{\partial\mathcal{B}_{BC}}{\partial\Phi^A}\right)\right) - \frac{\partial\mathcal{A}}{\partial\Phi^C}\left(\mathcal{B}_{AB} + 3\frac{\partial^2\mathcal{A}}{\partial\Phi^A\partial\Phi^B}\right)\right]\partial_\mu\Phi^A\partial^\mu\Phi^B \\ &\quad - 4\frac{\partial\mathcal{A}}{\partial\Phi^C}\kappa^2\mathcal{U} + 2\mathcal{A}\,\kappa^2\frac{\partial\mathcal{U}}{\partial\Phi^C} - \left(2\mathcal{A}\frac{\partial\alpha}{\partial\Phi^C} - \frac{\partial\mathcal{A}}{\partial\Phi^C}\right)\kappa^2 T\,.\end{aligned} \tag{A.25}$$

Remember that $\mathcal{B}_{AB}$ is symmetric and therefore

$$2\frac{\partial\mathcal{B}_{BC}}{\partial\Phi^A}\partial_\mu\Phi^A\partial^\mu\Phi^B = \left(\frac{\partial\mathcal{B}_{BC}}{\partial\Phi^A} + \frac{\partial\mathcal{B}_{AC}}{\partial\Phi^B}\right)\partial_\mu\Phi^A\partial^\mu\Phi^B\,. \tag{A.26}$$

A.2 Frame transformations

We consider a Wely transformation of the metric tensor $g_{\mu\nu} \to \bar{g}_{\mu\nu}$ and a reparametrization of the scalar fields $\Phi \to \bar{\Phi}$ defined by

$$g_{\mu\nu} = e^{2\bar{\gamma}(\bar{\Phi})}\bar{g}_{\mu\nu}\,, \tag{A.27a}$$

$$\Phi^A = \bar{f}^A(\bar{\Phi})\,. \tag{A.27b}$$

For derivatives w.r.t. a scalar field it follows that

$$\frac{\partial}{\partial\bar{\Phi}^A} = \frac{\partial\Phi^B}{\partial\bar{\Phi}^A}\frac{\partial}{\partial\Phi^B} = \bar{f}^B_{,A}\frac{\partial}{\partial\Phi^B}\,, \tag{A.28a}$$

$$\frac{\partial}{\partial\Phi^A} = \frac{\partial\bar{\Phi}^B}{\partial\Phi^A}\frac{\partial}{\partial\bar{\Phi}^B} = (\bar{f}^B_{,A})^{-1}\frac{\partial}{\partial\bar{\Phi}^B}\,. \tag{A.28b}$$

It is useful to know the following relations

$$\begin{aligned} g_{\mu\nu} &= e^{2\bar{\gamma}(\bar{\Phi})}\bar{g}_{\mu\nu}\,, && \text{(A.29a)}\\ g^{\mu\nu} &= e^{-2\bar{\gamma}(\bar{\Phi})}\bar{g}^{\mu\nu}\,, && \text{(A.29b)}\\ \sqrt{-g} &= e^{4\bar{\gamma}(\bar{\Phi})}\sqrt{-\bar{g}}\,, && \text{(A.29c)}\\ R &= e^{-2\bar{\gamma}(\bar{\Phi})}\left[\bar{R} - 6\bar{\nabla}^2\bar{\gamma}(\bar{\Phi}) - 6\bar{g}^{\mu\nu}(\partial_\mu\bar{\gamma}(\bar{\Phi}))(\partial_\nu\bar{\gamma}(\bar{\Phi}))\right]. && \text{(A.29d)} \end{aligned}$$

Now, we investigate how the individual terms in the action change under these transformations. The **curvature term** becomes

$$\sqrt{-g}\mathcal{A}(\Phi)R = \sqrt{-\bar{g}}e^{2\bar{\gamma}(\bar{\Phi})}\mathcal{A}(\Phi(\bar{\Phi}))\left[\bar{R} - 6\bar{\nabla}^2\bar{\gamma}(\bar{\Phi}) - 6\bar{g}^{\mu\nu}(\partial_\mu\bar{\Phi}^A)(\partial_\nu\bar{\Phi}^B)\bar{\gamma}_{,A}\bar{\gamma}_{,B}\right], \tag{A.30}$$

where we used $\partial_\mu\bar{\gamma}(\bar{\Phi}) = \frac{\partial\bar{\Phi}^A}{\partial x^\mu}\frac{\partial\bar{\gamma}}{\partial\bar{\Phi}^A} = (\partial_\mu\bar{\Phi}^A)\,\bar{\gamma}_{,A}$ with the notation $\bar{\gamma}_{,A} \equiv \frac{\partial\bar{\gamma}(\bar{\Phi})}{\partial\bar{\Phi}^A}$. When integrating, the middle term will yield (using integrating by parts)

$$\begin{aligned} &-\frac{1}{2\kappa^2}\int d^4x\sqrt{-\bar{g}}e^{2\bar{\gamma}(\bar{\Phi})}\mathcal{A}(\Phi(\bar{\Phi}))6\bar{\nabla}^2\bar{\gamma}(\bar{\Phi})\\ &= -\frac{1}{2\kappa^2}\int d^4x\,6\,e^{2\bar{\gamma}(\bar{\Phi})}\mathcal{A}(\Phi(\bar{\Phi}))\partial_\mu\left(\sqrt{-\bar{g}}\bar{g}^{\mu\nu}\partial_\nu\bar{\gamma}(\bar{\Phi})\right)\\ &= \frac{1}{2\kappa^2}\int d^4x\sqrt{-\bar{g}}\,6\,e^{2\bar{\gamma}(\bar{\Phi})}\left(2(\partial_\mu\bar{\Phi}^A)\,\bar{\gamma}_{,A}\mathcal{A}(\Phi(\bar{\Phi})) + \partial_\mu(\mathcal{A}(\Phi(\bar{\Phi})))\right)\bar{g}^{\mu\nu}(\partial_\nu\bar{\Phi}^B)\,\bar{\gamma}_{,B} + \text{B.T.} \end{aligned} \tag{A.31}$$

The boundary term (B.T.) can be ignored and therefore we can consider the following curvature term:

$$\begin{aligned} \sqrt{-\bar{g}}\Bigg[&e^{2\bar{\gamma}(\bar{\Phi})}\mathcal{A}(\Phi(\bar{\Phi}))\bar{R}\\ &+ 6\,e^{2\bar{\gamma}(\bar{\Phi})}\bar{g}^{\mu\nu}(\partial_\mu\bar{\Phi}^A)(\partial_\nu\bar{\Phi}^B)\left(\mathcal{A}(\Phi(\bar{\Phi}))\bar{\gamma}_{,A}\bar{\gamma}_{,B} + \frac{1}{2}\left(\frac{\partial\mathcal{A}}{\partial\bar{\Phi}^A}\bar{\gamma}_{,B} + \frac{\partial\mathcal{A}}{\partial\bar{\Phi}^B}\bar{\gamma}_{,A}\right)\right)\Bigg]. \end{aligned} \tag{A.32}$$

The **kinetic part** of the scalar field now takes the form

$$\sqrt{-g}\mathcal{B}_{AB}(\Phi)g^{\mu\nu}\partial_\mu\Phi^A\partial_\nu\Phi^B = e^{2\bar{\gamma}(\bar{\Phi})}\sqrt{-\bar{g}}\mathcal{B}_{AB}(\Phi(\bar{\Phi}))\bar{g}^{\mu\nu}(\partial_\mu\bar{\Phi}^C)(\partial_\nu\bar{\Phi}^D)\bar{f}^A_{,C}\bar{f}^B_{,D}\,, \tag{A.33}$$

with $\partial_\mu(\bar{f}^A(\bar{\Phi})) = \frac{\partial\bar{f}^A}{\partial\bar{\Phi}^C}\frac{\partial\bar{\Phi}^C}{\partial x^\mu} = \bar{f}^A_{,C}\,\partial_\mu\bar{\Phi}^C$, and the **scalar potential term** becomes

$$\sqrt{-g}2\kappa^2\mathcal{U}(\Phi) = \sqrt{-\bar{g}}2\kappa^2e^{4\bar{\gamma}(\bar{\Phi})}\mathcal{U}(\Phi)\,. \tag{A.34}$$

Taken all together, the action can now be written as

$$\begin{aligned} S =&\frac{1}{2\kappa^2}\int d^4x\sqrt{-\bar{g}}\Bigg(e^{2\bar{\gamma}(\bar{\Phi})}\mathcal{A}(\Phi(\bar{\Phi}))\bar{R}\\ &- \bar{g}^{\mu\nu}(\partial_\mu\bar{\Phi}^C)(\partial_\nu\bar{\Phi}^D)e^{2\bar{\gamma}(\bar{\Phi})}\\ &\quad\times\left[-6\,\bar{\gamma}_{,C}\bar{\gamma}_{,D}\mathcal{A}(\Phi(\bar{\Phi})) - 6\frac{1}{2}\left(\frac{\partial\mathcal{A}}{\partial\bar{\Phi}^C}\bar{\gamma}_{,D} + \frac{\partial\mathcal{A}}{\partial\bar{\Phi}^D}\bar{\gamma}_{,C}\right) + \bar{f}^A_{,C}\bar{f}^B_{,D}\mathcal{B}_{AB}(\Phi(\bar{\Phi}))\right]\\ &- 2\kappa^2e^{4\bar{\gamma}(\bar{\Phi})}\mathcal{U}(\Phi(\bar{\Phi}))\Bigg) + S_m[e^{2\alpha(\Phi(\bar{\Phi}))}e^{2\bar{\gamma}(\bar{\Phi})}\bar{g}_{\mu\nu},\chi]\,. \end{aligned} \tag{A.35}$$

Thus, in order for the action to be invariant under the transformations (A.27), i.e., such that it looks as

$$S =\frac{1}{2\kappa^2}\int d^4x\sqrt{-\bar{g}}\left(\bar{\mathcal{A}}(\bar{\Phi})\bar{R} - \bar{\mathcal{B}}_{AB}(\bar{\Phi})\bar{g}^{\mu\nu}(\partial_\mu\bar{\Phi}^A)(\partial_\nu\bar{\Phi}^B) - 2\kappa^2\bar{\mathcal{U}}(\bar{\Phi})\right) + S_m[e^{2\bar{\alpha}(\bar{\Phi})}\bar{g}_{\mu\nu},\chi]\,, \tag{A.36}$$

the following transformation laws must be satisfied:

$$\bar{\mathcal{A}}(\bar\Phi) = e^{2\bar\gamma(\bar\Phi)}\mathcal{A}(\Phi(\bar\Phi))\,, \tag{A.37a}$$

$$\bar{\mathcal{U}}(\bar\Phi) = e^{4\bar\gamma(\bar\Phi)}\mathcal{U}(\Phi(\bar\Phi))\,, \tag{A.37b}$$

$$\bar\alpha(\bar\Phi) = \alpha(\Phi(\bar\Phi)) + \bar\gamma(\bar\Phi)\,, \tag{A.37c}$$

$$\bar{\mathcal{B}}_{AB}(\bar\Phi) = e^{2\bar\gamma(\bar\Phi)}\left[-6\bar\gamma_{,A}\bar\gamma_{,B}\mathcal{A}(\Phi(\bar\Phi)) - 6\frac{1}{2}\left(\frac{\partial\mathcal{A}}{\partial\bar\Phi^A}\bar\gamma_{,B} + \frac{\partial\mathcal{A}}{\partial\bar\Phi^B}\bar\gamma_{,A}\right) + \bar f^C_{,A}\bar f^D_{,B}\mathcal{B}_{CD}(\Phi(\bar\Phi))\right]\,. \tag{A.37d}$$

Inverting those conditions gives

$$\mathcal{A}(\Phi(\bar\Phi)) = e^{-2\bar\gamma(\bar\Phi)}\bar{\mathcal{A}}(\bar\Phi)\,, \tag{A.38a}$$

$$\mathcal{U}(\Phi(\bar\Phi)) = e^{-4\bar\gamma(\bar\Phi)}\bar{\mathcal{U}}(\bar\Phi)\,, \tag{A.38b}$$

$$\alpha(\Phi(\bar\Phi)) = \bar\alpha(\bar\Phi) - \bar\gamma(\bar\Phi)\,, \tag{A.38c}$$

$$\begin{aligned}\mathcal{B}_{AB}(\Phi(\bar\Phi)) &= (\bar f^C_{,A})^{-1}(\bar f^D_{,B})^{-1}\left(e^{-2\bar\gamma(\bar\Phi)}\bar{\mathcal{B}}_{CD}(\bar\Phi) + 6\bar\gamma_{,C}\bar\gamma_{,D}\mathcal{A}(\Phi(\bar\Phi)) + 6\frac{1}{2}\left(\frac{\partial\mathcal{A}}{\partial\bar\Phi^C}\bar\gamma_{,D} + \frac{\partial\mathcal{A}}{\partial\bar\Phi^D}\bar\gamma_{,C}\right)\right)\\ &= e^{-2\bar\gamma(\bar\Phi)}(\bar f^C_{,A})^{-1}(\bar f^D_{,B})^{-1}\Big(\bar{\mathcal{B}}_{CD}(\bar\Phi) - 6\bar\gamma_{,C}\bar\gamma_{,D}\bar{\mathcal{A}}(\bar\Phi) + 3\left(\bar\gamma_{,C}\bar{\mathcal{A}}_{,D} + \bar\gamma_{,D}\bar{\mathcal{A}}_{,C}\right)\Big)\,.\end{aligned} \tag{A.38d}$$

Here, we used

$$\begin{aligned}\frac{\partial\mathcal{A}}{\partial\bar\Phi^A}(\Phi(\bar\Phi)) = \frac{\partial}{\partial\bar\Phi^A}\left(e^{-2\bar\gamma(\bar\Phi)}\bar{\mathcal{A}}(\bar\Phi)\right) &= -2\bar\gamma_{,A}\,e^{-2\bar\gamma(\bar\Phi)}\bar{\mathcal{A}}(\bar\Phi) + e^{-2\bar\gamma(\bar\Phi)}\frac{\partial\bar{\mathcal{A}}}{\partial\bar\Phi^A}(\bar\Phi)\\ &= -2\bar\gamma_{,A}\,e^{-2\bar\gamma(\bar\Phi)}\bar{\mathcal{A}}(\bar\Phi) + e^{-2\bar\gamma(\bar\Phi)}\bar{\mathcal{A}}_{,A}(\bar\Phi)\,.\end{aligned} \tag{A.39}$$

We define the quantity (see Eq. 2.76)

$$\mathcal{F}_{AB} \equiv \frac{2\mathcal{A}\mathcal{B}_{AB} + 3\mathcal{A}_{,A}\mathcal{A}_{,B}}{4\mathcal{A}^2}\,, \tag{A.40}$$

which we can interpret as a metric on the space of scalar fields since it is invariant under Weyl transformation and transforms as a tensor under scalar field redefinition. Here, we want to show this property. This can be seen by plugging

$$\mathcal{A}_{,A} = \frac{\partial\mathcal{A}}{\partial\Phi^A} = \frac{\partial\mathcal{A}}{\partial\bar\Phi^C}\frac{\partial\bar\Phi^C}{\partial\Phi^A} = e^{-2\bar\gamma}\left(-2\bar\gamma_{,C}\bar{\mathcal{A}} + \bar{\mathcal{A}}_{,C}\right)(\bar f^C_{,A})^{-1} \tag{A.41}$$

into the definition

$$\begin{aligned}\mathcal{F}_{AB} &= \frac{2\mathcal{A}\mathcal{B}_{AB}}{4\mathcal{A}^2} + \frac{3\mathcal{A}_{,A}\mathcal{A}_{,B}}{4\mathcal{A}^2}\\ &= (\bar f^C_{,A})^{-1}(\bar f^D_{,B})^{-1}\Bigg(\frac{2\bar{\mathcal{A}}\bar{\mathcal{B}}_{CD} - 12\bar\gamma_{,C}\bar\gamma_{,D}\bar{\mathcal{A}}^2 + 6\bar{\mathcal{A}}\left(\bar\gamma_{,C}\bar{\mathcal{A}}_{,D} + \bar\gamma_{,D}\bar{\mathcal{A}}_{,C}\right)}{4\bar{\mathcal{A}}^2}\\ &\quad + \frac{12\bar\gamma_{,C}\bar\gamma_{,D}\bar{\mathcal{A}}^2 - 6\bar{\mathcal{A}}(\bar\gamma_{,C}\bar{\mathcal{A}}_{,D} + \bar\gamma_{,D}\bar{\mathcal{A}}_{,C}) + 3\bar{\mathcal{A}}_{,C}\bar{\mathcal{A}}_{,D}}{4\bar{\mathcal{A}}^2}\Bigg)\\ &= (\bar f^C_{,A})^{-1}(\bar f^D_{,B})^{-1}\frac{2\bar{\mathcal{A}}\bar{\mathcal{B}}_{CD} + 3\bar{\mathcal{A}}_{,C}\bar{\mathcal{A}}_{,D}}{4\bar{\mathcal{A}}^2} = (\bar f^C_{,A})^{-1}(\bar f^D_{,B})^{-1}\bar{\mathcal{F}}_{CD}\,.\end{aligned} \tag{A.42}$$

Bibliography

[1] A. Schärer, R. Angélil, R. Bondarescu, P. Jetzer, and A. Lundgren, Phys. Rev. D **90**, 123005 (2014).

[2] M. Hohmann and A. Schärer, not yet submitted (2017).

[3] R. Angélil, P. Saha, R. Bondarescu, P. Jetzer, A. Schärer, and A. Lundgren, Phys. Rev. D **89**, 064067 (2014).

[4] A. Schärer, R. Bondarescu, P. Saha, R. Angélil, R. Helled, and P. Jetzer, submitted to Frontiers in Astronomy and Space Sciences (2017).

[5] R. Bondarescu, A. Schärer, A. Lundgren, G. Hetényi, N. Houlié, P. Jetzer, and M. Bondarescu, Geophys. J. Int. **202**, 1770 (2015).

[6] Y. M. Cho and P. G. O. Freund, Phys. Rev. D **12**, 1711 (1975).

[7] T. Damour and A. M. Polyakov, Nucl. Phys. B **423**, 532 (1994).

[8] G. Aad *et al.* (ATLAS Collaboration), Phys. Lett. B **726**, 120 (2013).

[9] A. H. Guth, Phys. Rev. D **23**, 347 (1981).

[10] S. M. Carroll, Phys. Rev. Lett. **81**, 3067 (1998).

[11] C. M. Will, Living Rev. Relativity **17** (2014).

[12] L. Perivolaropoulos, Phys. Rev. D **81**, 047501 (2010).

[13] A. Hees and A. Füzfa, Phys. Rev. D **85**, 103005 (2012).

[14] X.-M. Deng, Y. Xie, and T.-Y. Huang, Phys. Rev. D **79**, 044014 (2009).

[15] M. Hohmann, L. Järv, P. Kuusk, and E. Randla, Phys. Rev. D **88**, 084054 (2013).

[16] M. Hohmann, L. Järv, P. Kuusk, and E. Randla, Phys. Rev. D **89**, 069901 (E) (2014).

[17] J. Khoury and A. Weltman, Phys. Rev. Lett. **93**, 171104 (2004).

[18] J. Khoury and A. Weltman, Phys. Rev. D **69**, 044026 (2004).

[19] K. Hinterbichler and J. Khoury, Phys. Rev. Lett. **104**, 231301 (2010).

[20] K. Hinterbichler, J. Khoury, A. Levy, and A. Matas, Phys. Rev. D **84**, 103521 (2011).

[21] B. Bertotti, L. Iess, and P. Tortora, Nature **425**, 374 (2003).

[22] L. Cacciapuoti and C. Salomon, Eur. Phys. J. Spec. Top. **172**, 57 (2009).

[23] B. Altschul *et al.*, J. Adv. Space Res. **55**, 501 (2015).

[24] C. M. Will, *Theory and Experiment in Gravitational Physics* (Cambridge University Press, Cambridge, 1993).

[25] Y. Fujii and K.-I. Maeda, *The Scalar-Tensor Theory of Gravitation* (Cambridge University Press, Cambridge, 2003).

[26] A. K. Verma, A. Fienga, J. Laskar, H. Manche, and M. Gastineau, Astron. Astrophys. **561**, A115 (2014).

[27] E. V. Pitjeva and N. P. Pitjev, Mon. Not. R. Astron. Soc. **432**, 3431 (2013).

[28] P. Brax, A.-C. Davis, and J. Sakstein, Classical and Quantum Gravity **31**, 225001 (2014).

[29] D. Hobbs *et al.*, Proc. Int. Astron. Union **5**, 315 (2009).

[30] C. Brans and R. H. Dicke, Phys. Rev. **124**, 925 (1961).

[31] S. Weinberg, *Gravitation and Cosmology: Principles and Applications of the General Theory of Relativity* (John Wiley & Sons, Inc., New York, 1972).

[32] T. Damour and J. F. Donoghue, Phys. Rev. D **82**, 084033 (2010).

[33] N. Poli *et al.*, arXiv:1401.2378 (2014).

[34] B.J. Bloom *et al.*, Nature **506**, 71 (2014).

[35] R. Angélil and P. Saha, Astrophys. J. **711**, 157 (2010).

[36] J. Páramos and G. Hechenblaikner, Planet. Space Sci. **79–80**, 76 (2013).

[37] M. Hohmann, L. Järv, P. Kuusk, and E. Randla, Phys. Rev. D **88**, 084054 (2013).

[38] M. Hohmann, L. Järv, P. Kuusk, and E. Randla, Phys. Rev. D **89**, 069901 (2014).

[39] M. Hohmann *et al.*, Phys. Rev. D **94**, 124015 (2016).

[40] L. Järv, P. Kuusk, M. Saal, and O. Vilson, Phys. Rev. D **91**, 024041 (2015).

[41] P. Kuusk, L. Järv, and O. Vilson, Int. J. Mod. Phys. A **31**, 1641003 (2016).

[42] R. Kannan and P. Saha, The Astrophysical Journal **690**, 1553 (2009).

[43] J. H. Taylor, Rev. Mod. Phys. **66**, 711 (1994).

[44] M. Kramer *et al.*, Science **314**, 97 (2006).

[45] I. Ciufolini and E. Pavlis, Nature **431**, 958 (2004).

[46] I. Ciufolini *et al.*, European Physical Journal C **76**, 120 (2016), `1603.09674`.

[47] C. W. F. Everitt *et al.*, Physical Review Letters **106**, 221101 (2011).

[48] G. Renzetti, Open Physics **11**, 531 (2013).

[49] L. Iorio, H. I. Lichtenegger, M. L. Ruggiero, and C. Corda, Astrophysics and Space Science **331**, 351 (2011).

[50] N. Ashby, Living Reviews in Relativity **6**, 1 (2003).

[51] L. Cacciapuoti and C. Salomon, in *Journal of Physics: Conference Series* (IOP Publishing, 2011), vol. 327, p. 012049.

[52] Altschul, B. *et al.*, Advances in Space Research **55**, 501 (2015).

[53] R. Bondarescu *et al.*, Geophysical Journal International **191**, 78 (2012).

[54] J. Lense and H. Thirring, Physikalische Zeitschrift **19** (1918).

[55] R. Helled, J. D. Anderson, G. Schubert, and D. J. Stevenson, Icarus **216**, 440 (2011).

[56] L. Iorio, Classical and Quantum Gravity **30**, 195011 (2013).

[57] L. Iorio, New Astronomy **15**, 554 (2010).

[58] M. Preto and P. Saha, APJ **703**, 1743 (2009), `0906.2226`.

[59] R. Angélil, P. Saha, and D. Merritt, The Astrophysical Journal **720**, 1303 (2010).

[60] R. Angélil and P. Saha, APJL **734**, L19 (2011), `1105.0918`.

[61] R. Angélil and P. Saha, MNRAS **444**, 3780 (2014).

[62] F. Zhang and L. Iorio, ApJ **834**, 198 (2017), `1610.09781`.

[63] B. Mashhoon, F. W. Hehl, and D. S. Theiss, General Relativity and Gravitation **16**, 711 (1984).

[64] R. Helled, The Astrophysical Journal Letters **735**, L16 (2011).

[65] N. Nettelmann, J. Fortney, K. Moore, and C. Mankovich, Monthly Notices of the Royal Astronomical Society **447**, 3422 (2015).

[66] V. N. Zharkov and V. P. Trubitsyn, Moscow, Izdatel'stvo Nauka, 1980. 448 p. In Russian. **1** (1980).

[67] T. Guillot and D. Gautier, *Treatise on geophysics, planets and moons, vol. 10* (2007), `arXiv:0912.2019`.

[68] R. Helled, J. D. Anderson, and G. Schubert, Icarus **210**, 446 (2010).

[69] R. Helled, G. Schubert, and J. D. Anderson, Planetary and Space Science **57**, 1467 (2009).

[70] R. Helled, E. Galanti, and Y. Kaspi, Nature **520**, 202 (2015).

[71] D. Gurnett, A. Persoon, W. Kurth, J. Groene, T. Averkamp, M. Dougherty, and D. Southwood, Science **316**, 442 (2007).

[72] A. P. Ingersoll and D. Pollard, Icarus **52**, 62 (1982).

[73] M. G. Sterenborg and J. Bloxham, Geophysical Research Letters **37** (2010).

[74] J. D. Anderson and G. Schubert, Science **317**, 1384 (2007).

[75] P. Read, T. Dowling, and G. Schubert, Nature **460**, 608 (2009).

[76] S. Matousek, Acta Astronautica **61**, 932 (2007).

[77] S. G. Edgington and L. J. Spilker, Nature Geoscience **9**, 472 (2016).

[78] N. Hinkley, *et al.*, Science **341**, 1215 (2013).

[79] T.L. Nicholson *et al.*, Nat. Commun. **6**, 6896 (2015).

[80] S. Droste *et al.*, Phys. Rev. Lett. **111**, 110801 (2013).

[81] K. Mogi, Bull. Earthq. Res. Inst. **36**, 99 (1958).

[82] G. Blewitt and D. Lavallée, J. Geophys. Res. **107**, (B7), 2145. (2002).

[83] N. Houlié and T. Stern, EPSL **345–348**, 117–125 (2012).

[84] R. Jolivet, R. Bürgmann, and N. Houlié, Earth Planet. Sci. Lett. **288**, 26 (2009).

[85] N. Houlié and B. Romanowicz, Phys. Earth Planet. In. **184**, 143 (2011).

[86] N. Houlié and J. Montagner, EPSL **261**, 1 (2007).

[87] D. Boore, Bull. Seismol. Soc. Am. **93**, 2017 (2003).

[88] H. Rymer and G. Williams-Jones, Geophys. Res. Lett. **27**, 2389 (2000).

[89] D. Agnew, *Treatise on Geophysics, 3.06 - Earth Tides* (Elsevier, Amsterdam, 2007), pp. 163–195.

[90] N. Poli *et al.*, Appl. Phys. B **117**, 1107 (2014).

[91] C.J. Campbell *et al.*, Phys. Rev. Lett. **108**, 120802 (2012).

[92] A. Kozlov, V. Dzuba, and V. Flambaum, Phys. Rev. A **88**, 032509 (2013).

[93] A. Derevianko, V. Dzuba, and V. Flambaum, Phys. Rev. Lett. **109**, 180801 (2012).

[94] N. Houlié, P. Briole, A. Bonforte, and G. Puglisi, Geophys. Res. Lett. **33**, L02309 (2006).

[95] J. Biggs, I. Bastow, D. Keir, and E. Lewi, Geochem. Geophys. Geosyst. **12**, Q0AB10 (2011).

[96] K. Pascal, J. Neuberg, and E. Rivalta, Geophys. J. Int. **196**, 253–278 (2014).

[97] Y. Hagiwara, Bull. Earthq. Res. Inst. **52**, 301 (1977).

[98] I. Gradshteyn and I. Ryzhik, *Table of Integrals, Series, and Products* (Elsevier, Burlington, San Diego, London., 2007), 7th ed.

[99] L. Yuan and B. Chao, EPSL **355**, 255 (2012).

SCHÄRER Andreas — Curriculum Vitae

Personal information

Date of birth	3 September 1987
Nationality	Swiss
Place of origin	Stein am Rhein, SH
Marital status	engaged

Education

2013–2017 **Doctorate**
Physik-Institut, Universität Zürich
Supervisors: Prof. Dr. Ph. Jetzer, Prof. Dr. P. Saha
Thesis title: "General Relativity: Alternatives, Tests and Applications"

2011–2013 **Master** in Theoretical Physics
Universität Zürich
Supervisors: Prof. Dr. Ph. Jetzer, Dr. R. Bondarescu
Thesis title: "Constraints on Scalar Field Models from Tests of General Relativity"

2007–2012 **Bachelor** in Mathematics and Physics
Universität Zürich
Bachelor thesis in Physics:
Supervisors: Prof. Dr. Ph. Jetzer, Dr. R. Bondarescu
Thesis title: "Einstein Equivalence Principle Tests of General Relativity"

2003–2007 **Matura**
Pädagogische Maturitätsschule Kreuzlingen

Publications

2014 "Spacecraft clocks and relativity: Prospects for future satellite missions"
R. Angélil, R. Saha, B. Bondarescu, P. Jetzer, A. Schärer and A. Lundgren.
Phys. Rev. D, **89**, *064067.*

2014 "Testing scalar-tensor theories and parametrized post-Newtonian parameters in Earth orbit"
A. Schärer, R. Angélil, R. Bondarescu, P. Jetzer and A. Lundgren.
Phys. Rev. D, **90**, *123005.*

2015 "Ground-based optical atomic clocks as a tool to monitor vertical surface motion"
R. Bondarescu, A. Schärer, A. Lundgren, G. Hetényi, N. Houlié, P. Jetzer and M. Bondarescu.
Geophys. J. Int., **202**, *1770.*

2015 "Testing general relativity and alternative theories of gravity with space-based atomic clocks and atom interferometers"
R. Bondarescu, A. Schärer, P. Jetzer, R. Angélil, P. Saha, and A. Lundgren.
Proceedings of the 3rd International Conference on New Frontiers in Physics, Kolymbari, Crete, Greece.

Conferences, Schools and Talks

May 22-23 2013	STE-QUEST Workshop Poster: “Testing Chameleon Scalar Fields With STE-QUEST” *ESTEC, Noordwijk - The Netherlands*
Feb. 6-7 2014	Swiss Cosmology Days *ETH Zurich - Switzerland*
June 23-26 2014	28th European Frequency and Time Forum *University of Neuchâtel - Switzerland*
Sep. 14-19 2014	DPG Physics School on General Relativity 99 *Physikzentrum Bad Honnef - Germany*
Jan. 19-22 2014	School on Scientific Programming with Python *University of Zurich - Switzerland*
July 12-18 2015	Fourteenth Marcel Grossmann Meeting - MG14 Talk: “Prospects for Testing GR and Alternative Theories with Clocks in Earth Orbit” *University of Rome ‘La Sapienza’, Rome - Italy*
Sep. 5-9 2016	11th International LISA Symposium *University of Zurich - Switzerland*
Mar. 21 2017	Seminar: “PPN Parameters in Scalar-Tensor Theories” *Physics Institute, University of Tartu - Estonia*